On-board Correction Estimation

for LEO-PNT Satellites

MSc Thesis

Jillian S. Oduber

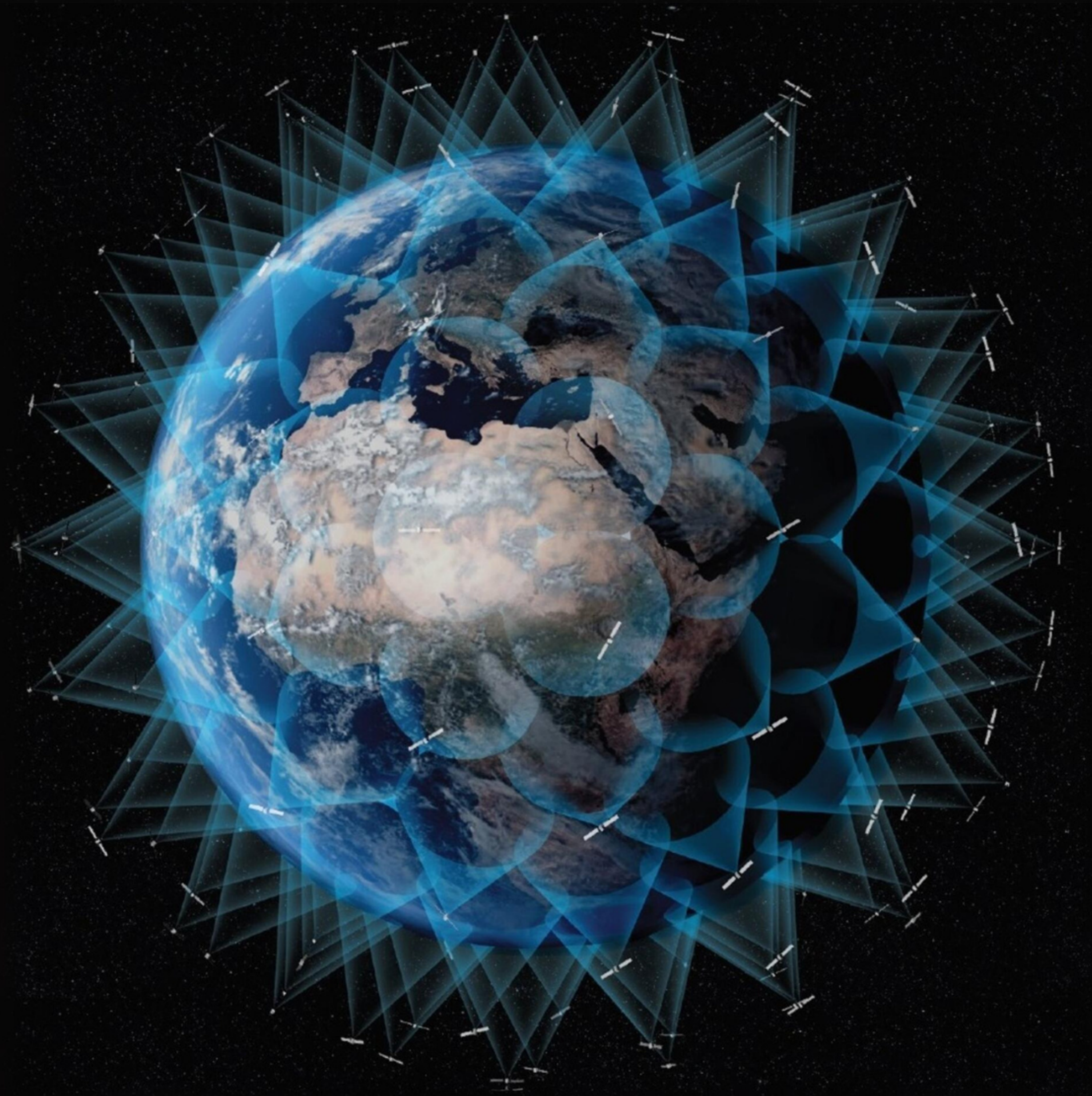

Faculty of Aerospace Engineering

TU Delft

On-board Correction Estimation

for LEO-PNT Satellites

by

Jillian S. Oduber

To obtain the degree of

Master of Science
in Aerospace Engineering

at the Delft University of Technology,

to be defended publicly on Wednesday March 5th, 2025 at 14:00.

Student number:	4534581	
Project duration:	March 2024 – March 2025	
Supervisors:	Dr.ir. J.A.A. van den IJssel	TU Delft
	Dr.ir. L. Massarweh	TU Delft
Thesis committee:	Prof.dr.ir. P.N.A.M. Visser	TU Delft
	Dr.ir. A.A. Verhagen	TU Delft

Cover: Property of the European Space Agency (ESA)

TU Delft

Preface

This report presents the work done for my MSc thesis on *On-board Correction Estimation for LEO-PNT Satellites*. I have been so fortunate to have been able to work on this topic for my thesis. Through this work I have been able to gain such a deeper understanding, fascination, and appreciation for the rich fields of POD, PPP, GNSS, and more. For this thesis, I was lucky enough to have not just one, but two incredibly supportive and knowledgeable supervisors. Jose and Lotfi, I cannot thank you enough for all your support, patience, and everything you have taught me during this journey.

Next, I would like to give my thanks and appreciation to a few more people who have made this work possible. I would like to thank Dr. Oliver Montenbruck for allowing access to the GHOST tool and providing the Sentinel-6A setup. I would also like to thank Florin Grec and the ESA LEO-PNT program team for the various exchanges we had under the ESA_Lab@TU Delft collaboration framework and the continued interest in our work. Thank you also to Filipe De Oliveira Salgueiro specifically for providing the HAS data that I used in this thesis. Lastly, I would like to thank Lotfi again for allowing me to use the LEOPARD tool, it has been really great being able to see all the results come together, which would not have been possible without it!

Thank you to all of my friends and family, for being so supportive and patient with me. Most of all, thank you to my parents for always supporting me unconditionally in whatever I set out to do. None of this would have been possible without you. Masha, masha danki!

Jillian S. Oduber
Delft, February 18th, 2025

Contents

List of Abbreviations and Symbols

Abbreviations

Abbreviation	Definition
BDS	BeiDou Navigation Satellite System
BRD	Broadcast Ephemerides
CDDIS	Crustal Dynamics Data Information System
CDMA	Code Division Multiple Access
CSAC	Chip-Scale Atomic Clocks
CSDE	Copernicus Space Data Ecosystem
DCB	Differential Code Bias
DLR	German Aerospace Center
DOD	Dynamic Orbit Determination
DOP	Dilution of Precision
DORIS	Doppler Orbitography and Radio-positioning Integrated by Satellite
EC	European Commission
ECEF	Earth-Centered Earth-Fixed
ECI	Earth-Centered Inertial
ESA	European Space Agency
EU	European Union
FDMA	Frequency Division Multiple Access
FOC	Full Operational Capability
GDOP	Geometric Dilution of Precision
GEO	Geostationary Orbit
GHOST	GPS High Precision Orbit Determination Software
GLONASS	Globalnaya Navigatsionnaya Sputnikovaya Sistema
GNSS	Global Navigation Satellite System
GPS	Global Positioning System
HAS	High Accuracy Service
IF	Ionosphere Free
IGS	International GNSS Service
IGSO	Inclined Geosynchronous Orbit
IOC	Initial Operational Capability
IOV	In-Orbit Validation
ISB	Inter-System Bias
JAXA	Japan Aerospace Exploration Agency
KF	Kalman Filter
KOD	Kinematic Orbit Determination
LEO	Low Earth Orbit
LEO-PNT	Low Earth Orbit Positioning, Navigation, and Timing
LOS	Line of Sight
LS	Least-Squares
MEO	Medium Earth Orbit
NASA	National Aeronautics and Space Administration
NRT	Near Real-Time
OD	Orbit Determination

Abbreviation	Definition
ODTS	Orbit Determination and Time Synchronization
OS	Open Service
PCO	Phase-Center Offset
PCV	Phase-Center Variations
PDOP	Position Dilution of Precision
PNT	Positioning, Navigation, and Timing
POD	Precise Orbit Determination
PPP	Precise Point Positioning
PPP-AR	Precise Point Positioning Ambiguity Resolution
PPP-RTK	Precise Point Positioning Real-Time Kinematic
PPS	Precision Positioning Service
PRN	Pseudo-Random Noise
RDOD	Reduced-Dynamic Orbit Determination
RHCP	Right-Hand Circular Polarized
RINEX	Receiver Independent Exchange
RT	Real-Time
S-6A	Sentinel-6A
SA	Selective Availability
SBAS	Satellite-Based Augmentation Systems
SF	Single Frequency
SISRE	Signal-in-Space Range Error
SLR	Satellite Laser Ranging
SOOP	Signals of Opportunity
SP3	Standard Product #3 (orbital format)
SPP	Single Point Positioning
SPS	Standard Positioning Service
SSR	State Space Representation
SSV	Space Service Volume
STEC	Slant Total Electron Content
STL	Satellite Time and Location
SWaP	Size, Weight, and Power
TEC	Total Electron Content
TGD	Timing Group Delay
TSV	Terrestrial Service Volume
TT&C	Telemetry, Tracking, and Control
UEE	User Equipment Error
UERE	User Equivalent Range Error
US	United States
VTEC	Vertical Total Electron Content
ZTD	Zenith Tropospheric Delay

Symbols

Symbol	Definition
$T^s_{\mathrm{r},0}$	a-priori tropospheric correction
C	carrier signal
$\varphi^s_{r,j}$	carrier-phase
$\zeta^s_{r,j}$	carrier-phase antenna phase-center offsets
C/N_0	carrier-to-noise-power-density ratio
$\xi^s_{r,j}$	code antenna phase-center offsets
$e^s_{r,j}$	code receiver noise and multipath error
pos	code scaling coefficient for combined observables
$o^s_{r,c}$	combined observable
S	constellation index
J_2	Earth oblation gravitational perturbation
$\omega_\oplus$	Earth's rotation rate
f^S_j	frequency
ρ^s_r	geometric range
d	hardware delay
$\mathbf{C}_n$	identity matrix with p-th column removed, resulting in $n \times (n-1)$ matrix
Δ	incremental operator
$\Delta d^s_{r,j}$	interchannel bias
μ^{S}_j	ionospheric coefficient
$I^s_{r,j}$	ionospheric delay
$\boldsymbol{e}^s_r$	Line-of-Sight (LOS) unit vector
$\mathbf{G}^{\mathrm{S}}_r$	matrix of LOS unit vectors
$\mathbf{I}_n$	$n \times n$ identity matrix
N_0	noise power
m_{S}	number of observed satellites
$N^s_{r,j}$	phase integer ambiguity
$\varepsilon^s_{r,j}$	phase receiver noise and multipath error
α_j	phase scaling coefficient for combined observables
ω^s_r	phase wind-up correction
p	pivot satellite index
$p^s_{r,j}$	pseudorange
$\dot{\rho}^s_r$	range rate
dt_r	receiver clock offset
$d_{r,j}$	receiver code hardware delay
r	receiver index
$\delta_{r,j}$	receiver phase hardware delay
$\boldsymbol{r}_r$	receiver position
$\delta t^{\mathrm{rel}}_{\mathrm{clk}}$	relativistic clock correction
δt^{rel}	relativistic delay
$\mathbf{R}(T)$	rotation matrix
dt^s	satellite clock offset
dt^s	satellite code hardware delay
s	satellite index

Symbol	Definition
δ_j^s	satellite phase hardware delay
$\boldsymbol{r}^S$	satellite position
j	signal/frequency index
$\delta t_{\mathrm{stc}}^{\mathrm{rel}}$	space-time curvature relativistic delay
c	speed of light
$\boldsymbol{x}_r$	state vector of receiver position and zenith tropospheric delay
t^{AB}	system time offset
t	time
t_A	time of arrival
t_E	time of emission
τ	travel time or propagation time
T_r^s	tropospheric delay
$\boldsymbol{g}_r^s$	vector in $\mathbf{G}_r^{\mathrm{S}}$ matrix
$\boldsymbol{u}_n$	vector of n ones
$\boldsymbol{I}_r^{\mathrm{S}}$	vector of ionospheric delay parameters
λ_j	wavelength
T_r^{Z}	zenith tropospheric delay
m_r^s	zenith tropospheric delay mapping function

Abstract

Global Navigation Satellite Systems (GNSS) have become crucial for providing Positioning, Navigation, and Timing (PNT) services worldwide. Existing GNSS constellations such as GPS, GLONASS, BeiDou, and Galileo operate in Medium Earth Orbit (MEO) at around 20,000 km altitude. Low Earth Orbit Positioning, Navigation, and Timing (LEO-PNT) is an emerging satellite navigation concept to augment current GNSS by placing satellites closer to Earth, at around 600-1200 km altitude. This lower altitude results in a faster change in satellite geometry, which is primarily expected to reduce the convergence time of Precise Point Positioning (PPP). To fully realize this opportunity, accurate knowledge of the LEO-PNT satellite orbital positions and clock offsets at a low latency is required. For existing GNSS constellations, global networks of ground stations are generally used to determine the GNSS satellite positions and clock offsets. This information is then uplinked to the GNSS satellites for dissemination to users. Due to the closer proximity to Earth, LEO-PNT systems would require an extensive ground network to replicate the ground estimation approach of GNSS. However, being situated below MEO, there is an opportunity to leverage GNSS to perform real-time Precise Orbit Determination (POD) on board the LEO-PNT satellites.

This thesis aims to quantify the impact on ground user positioning that the LEO-PNT satellites could have when using on-board POD. This numerical assessment was performed in two main parts. In the first part, the achievable accuracies for real-time on-board POD were investigated using real-world GPS and Galileo observations from the Sentinel-6A mission for the period of DOY 118-124 in 2024. A reduced-dynamic Extended Kalman Filtering (EKF) approach with degraded dynamical models was used to replicate the on board processing conditions. Various types of GNSS products were considered to assess their impact on the POD accuracy achievable on board. As compared to the Sentinel-6A reference orbits, 3D RMS orbit errors of 2.8 cm, 4.8 cm, 9.9 cm, and 14.5 cm were obtained for the real-time POD computations when respectively using CODE MGEX final products (COD), the CNES Real-Time products (CRT), the Galileo High Accuracy Service corrections (HAS), and the broadcast ephemerides (BRD). Furthermore, a reduced-dynamic Batch Least-Squares POD approach was used to obtain a reference Sentinel-6A clock solution. This resulted in clock error standard deviations of 9.9 cm, 10.7 cm, 15.9 cm, and 21.6 cm for the on-board POD using COD, CRT, HAS, and BRD products respectively.

In the second part, the real-time Sentinel-6A POD results were used to quantify the impact of the LEO satellite orbit and clock errors on kinematic float-PPP simulated for a ground user located at Redu, Belgium on DOY 121 in 2024. A LEO space segment of 28 satellites was simulated to augment the cases of GPS-only, Galileo-only, and GPS+Galileo, while considering different product error levels for both the LEO and MEO satellites. The results showed that including this LEO constellation with orbit and clock errors from on-board POD using CRT products consistently improved the PPP convergence time and positioning accuracy as compared to using stand-alone MEO GNSS. When using GPS+Galileo with CRT products, adding the LEO constellation with CRT-level orbit and clock errors improved the 3D convergence time to 20 cm from 6.0 to 3.7 minutes and reduced the 3D RMS error from 4.7 cm to 3.8 cm. For HAS products, it enabled 3D convergence in 11 minutes (previously >60 min) and improved the 3D RMS error from 13.2 cm to 9.2 cm. The PPP performance when adding the LEO constellation using on-board POD with HAS and BRD products was only improved for the HAS ground user, and was degraded for the CRT ground user. These results indicate that improvements from LEO-PNT augmentation are only possible when sufficiently accurate orbits and clocks are available, though this also depends on the type of GNSS products employed by the ground user. The impact of the LEO-PNT correction dissemination latency still must be further investigated.

1 Introduction

1.1. Background & Relevance

Global Navigation Satellite Systems (GNSS) have become instrumental in providing Positioning, Navigation, and Timing (PNT) services on and around the Earth. The current operational GNSS constellations, namely GPS (USA), GLONASS (Russia), BeiDou (China), and Galileo (EU), predominantly operate in Medium Earth Orbit (MEO) at around 20,000 km in altitude. Thanks to factors such as an increased variety in launch vehicle providers and advancements in satellite technology (Reid et al., 2020b), there is an ongoing trend towards the deployment of constellations in Low Earth Orbit (LEO), which is defined in a range between 200 to 2000 km in altitude (Teunissen and Montenbruck, 2017, Chapter 32). Such LEO mega-constellations, ranging from tens to thousands of satellites in size, have been conceptualized for a variety of applications. This includes the provision of PNT services in support of or as an alternative to the existing GNSS (Reid et al., 2020b). Iridium's Satellite Time & Location service (STL, originally created with Satelles from 2016) already commercially offers PNT services using signals from its Iridium NEXT satellites in LEO. Commercial initiatives such as CentiSpace (Beijing Future Navigation Technology Company), Pulsar (Xona Space Systems), and TrustPoint, as well as institutional ones such as the European Space Agency's (ESA) LEO-PNT In-Orbit Demonstration are among the new LEO-PNT constellations proposed so far (UNOOSA, 2023).

While positioning performance would naturally be expected to benefit from the availability of more PNT satellites, the main difference of PNT from LEO as compared to MEO is the closer proximity to Earth. This results in a reduced free-space path loss, potentially enhancing performance against interference and in more challenging environments. The lower orbit also offers a higher orbital velocity, leading to quicker changes in satellite geometry with respect to ground users. This rapidly changing geometry is expected to help with whitening multipath effects (Reid et al., 2020b), and especially with reducing the convergence time of Precise Point Positioning (PPP) as compared to using MEO GNSS alone (Zheng et al., 2024). This improved PPP convergence time has been one of the main topics of LEO-PNT research in literature until now. Studies such as Li et al. (2019c) and Ge et al. (2020b) have shown that PPP convergence times in the order of 1-3 minutes can be achieved at all latitudes when augmenting both single and multi-GNSS with around 150 or more LEO satellites.

Besides the potential benefits of a LEO-PNT constellation, the closer proximity to Earth also raises several challenges. Being closer to Earth leads to a smaller footprint per satellite, requiring a large number of LEO satellites to achieve global coverage. LEO satellites also experience larger dynamical perturbations and have shorter overpass times as compared to MEO. Accurate knowledge of the orbital positions and clock offsets of the satellites are fundamental for any satellite navigation system, as they are needed by ground users who are estimating their location using the corresponding ranging measurements. In existing GNSS, these satellite orbits and clocks are determined by global networks of ground stations in a process referred to as Orbit Determination and Time Synchronization (ODTS). This approach is not foreseen to be a practical solution for future LEO-PNT constellations, as an extensive ground network would be needed due to the aforementioned closer proximity to Earth. Instead, being situated below MEO, there is the opportunity to perform real-time Precise Orbit Determination (POD) on board the LEO satellites themselves by leveraging the use of GNSS receivers.

This on-board real-time GNSS-based POD has been shown to be a viable option, such as in the study conducted by Hauschild and Montenbruck (2021). Here, 3D RMS position accuracies of around 8.5 cm were achieved using the GNSS broadcast ephemerides in combination with the reduced-dynamic orbit determination method (Wu et al., 1990). Using the Galileo High Accuracy Service (HAS), which provides real-time corrections for GPS and Galileo through the E6 signal (European Union, 2022), could potentially further improve on-board POD performance. Using preliminary HAS test data, Hauschild et al. (2022) showed that the HAS corrections improved the 3D position accuracy by approximately 10% in the case of dual-constellation real-time POD of the Sentinel-6A satellite as compared to using broadcast ephemerides alone.

1.2. Literature Review, Research Gap, Research Objectives, & Research Questions

As mentioned, LEO-PNT has been identified as a potential contributor to reducing PPP convergence times from tens of minutes to a few minutes. A literature study was performed in preparation for this thesis to explore the state-of-the-art in LEO-PNT research, and to identify specific research gaps regarding on-board real-time estimated LEO satellite orbit and clock corrections, and their potential impact on ground user positioning performance. The following key findings from the literature study can be summarized and categorized as follows:

1. **LEO-PNT PPP studies using simulated LEO satellite orbits:** As mentioned, many studies so far have looked into the potential PPP improvements when including a LEO-PNT constellation. Several of these studies have begun with simulating observations from the LEO satellites using nominal LEO satellite orbits without considering the any additional orbit errors (Ge et al., 2018), (Su et al., 2019), (Ge et al., 2020b), (Hong et al., 2023), (Li et al., 2023), (Li et al., 2019b).

   In practice, similar to GNSS satellites, the satellite orbits and clocks determined in the LEO-PNT's ODTS will have some level of error. Wang et al. (2024) investigated the addition of synthetic LEO satellite orbit errors to their LEO observation simulation by using sine functions to simulate the LEO satellite orbital errors. Furthermore, Li et al. (2019c) considered synthetic LEO satellite orbit errors by emulating on-board kinematic POD with simulated GNSS measurements.

   Overall, these studies have found that that inclusion of LEO satellites could speed up PPP convergence, though none of these studies explicitly dealt with on-board LEO satellite orbit and clock estimation **using real-world data, leaving a gap in understanding how those errors could impact the PPP performance.**

2. **Studies using real-world measurements:**

   - **LEO-PNT PPP studies:** PPP performance using LEO satellites has been studied with real measurements from the experimental CentiSpace satellites (Li et al., 2024), (Xu et al., 2024). Here, the LEO satellite orbits were determined from on-board GNSS measurements using the reduced dynamic technique, **though the LEO satellite clock offsets were determined with measurements gathered from the ground.**

   - **On-board POD studies:** The study of (Kunzi et al., 2023) does outline the strategy of using reduced-dynamic on-board orbit and clock determination in real-time for LEO satellite navigation. **However, they did not use their estimated on-board LEO satellite orbit and clock in PPP computations directly.**

3. **On-ground POD studies:** Studies such as Li et al. (2019a) have still investigated the potential of ground-based POD processing schemes for LEO-PNT. Other examples of these types of studies are Wang et al. (2023a) and Wang et al. (2024) that investigated the strategy of using batch processing for near real-time POD combined with short-term prediction, and Ge et al. (2020a) which considered the use of on-board gathered accelerometer data to improve the LEO satellite orbit prediction that is computed on the ground.

As mentioned, there lies a significant opportunity to reduce the need for an extensive ground tracking network if on-board real-time POD can provide sufficiently adequate LEO-PNT orbit and clock corrections. Based on this opportunity and on the individual gaps listed for each of the above categories, the main identified research gap is that none of the reviewed studies have addressed the combination of using real-world GNSS data to assess the on-board real-time estimation of both LEO-PNT satellite orbit and clock errors, and subsequently used these errors in a PPP analysis.

Based on this research gap, the following research objective for this thesis was defined. The research objective is to:

Quantify the impact on user positioning that LEO-PNT satellite orbit and clock errors determined with on-board real-time precise orbit determination will have.

The following research questions were formulated to address this objective:

1. What **orbit and clock accuracies** can be expected from on-board real-time POD for LEO-PNT satellites?
   (a) What **accuracies** can be expected from using only **broadcast ephemerides**?
   (b) What **accuracies** can be expected from using **high-accuracy GNSS corrections** made available to LEO-PNT satellites?
2. What **user positioning performances** can be expected when using LEO-PNT in addition to MEO GNSS?
   (a) What is the effect of the **accuracy** of the LEO-PNT **orbit** products on precise user positioning?
   (b) What is the effect of the **accuracy** of the LEO-PNT **clock** products on precise user positioning?

As can be seen from the division of the the research questions, two main bodies of work were identified for this thesis. These can briefly be referred to as the POD part and PPP part. A visual summary of these two parts and how they relate is shown in Figure 1.1.

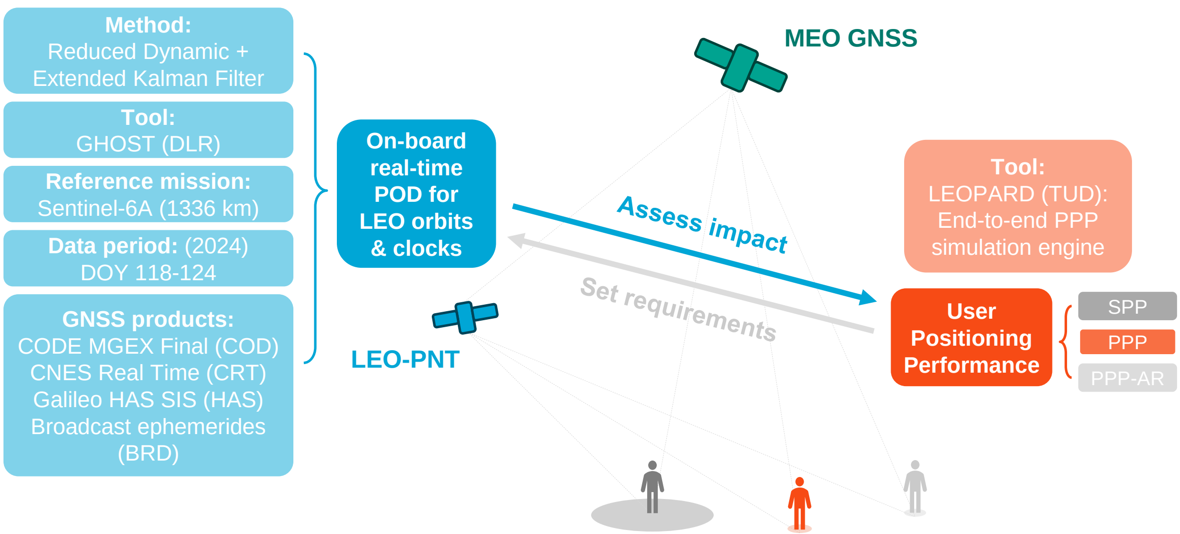

Figure 1.1: A visual representation of the two main parts of this research and their relation to each other. This study has focused on numerically assessing the impact of the on-board real-time estimation of LEO-PNT satellite orbit and clock errors on PPP ground users specifically. The findings of this study could potentially support the requirement definition for future LEO-PNT systems regarding the on-board POD performance, though this aspect has not been addressed in this work specifically.

1.3. Thesis Outline

This thesis report is organized as follows. First, Chapter 2 provides the relevant background information on existing GNSS systems and their principles, along with emerging LEO-PNT concepts and their key benefits and challenges. Next, Chapter 3 introduces the methods for POD and PPP. For the POD, the relevant considerations and key aspects for LEO-PNT are addressed, and the achievable performances of the state-of-the-art in real-time POD are briefly introduced. In the PPP part, the user positioning methods are recapped and the main expected impact of LEO-PNT on each of them is highlighted. Then, the mission and data to be used in this study are detailed in Chapter 4, namely the selected Sentinel-6A mission, as well as the various MEO GNSS products that are considered. Next, the POD setup and results are presented in Chapter 5 and Chapter 6 respectively. Similarly, the PPP setup and results are respectively shown in Chapter 7 and Chapter 8. Finally, the conclusion is given in Chapter 9, along with some recommendations for future work that build up on the results of this thesis.

2
Background

This chapter provides background information on GNSS systems in general given in Section 2.1, as well as more specific aspects related to LEO-PNT systems given in Section 2.2. The content of this chapter has been summarized from the literature study preceding this thesis report.

2.1. Global Navigation Satellite Systems (GNSS)

Global Navigation Satellite Systems (GNSS) provide positioning and timing solutions anywhere in the world. These systems consist of three segments. The first is the space segment, which is a constellation of satellites that transmit the designated signals. The second is the control segment, which monitors and maintains the constellation. The last is the user segment, consisting of receivers that are able to receive the signals from the navigation satellites (Teunissen and Montenbruck, 2017, Chapter 1). The services provided by GNSS can be categorized into two main service volumes (UNOOSA, 2021). The Terrestrial Service Volume (TSV) is the shell within which the GNSS performance and visibility specifications are valid and covers users from the Earth's surface up to an altitude of 3000 km. Though no specific commitments were originally made for the Space Service Volume (SSV), which extends from 3000 km to 36000 km, users can still make use of limited coverage and performance available in this region, which is covered by the side lobes of the transmitted signals (Montenbruck et al., 2023).

As mentioned, GNSS satellites transmit signals to users. These signals are a carrier wave in the L-band (1.2-1.6 GHz) modulated with a Pseudo-Random Noise (PRN) code and a low-rate data stream. The PRN code facilitates the ranging measurements, while the data stream contains further navigation data needed by the user. The basic concept of GNSS positioning and timing is to use range measurements from several satellites along with the data provided in the navigation message to solve for the receiver's position and clock offset. The basic measurements essentially measure the signal's propagation time τ from satellite to receiver. This measurement is enabled by the PRN code, where a locally generated PRN is aligned to the received PRN in a tracking loop. The code phase yielding this alignment corresponds to the transmission time of the signal. Along with knowledge of the reception time, the propagation time can then be computed, which produces a distance when multiplying with the speed of light (Teunissen and Montenbruck, 2017, Chapter 1).

2.1.1. Existing Systems

The key characteristics for each GNSS are presented in Table 2.1. This thesis has only considered the use of GPS and Galileo, which are briefly described below.

GPS

The Global Positioning System (GPS) is the GNSS of the United States of America (USA). Originally named Navstar GPS, the project was started in the 1970s, and its first satellite was launched in 1978. GPS was originally intended for military use, but was also made available for civilian use from early on (Teunissen and Montenbruck, 2017, Chapter 1). As of July 2023, there are 31 operational satellites in orbit, not including spare and/or decommissioned satellites. GPS's Initial Operational Capability (IOC) was achieved in 1993 once a full nominal constellation was in orbit and its Standard Positioning

Table 2.1: The key characteristics of existing GNSS constellations. The following acronyms can be clarified: Medium Earth Orbit (MEO), Inclined Geosynchronous Orbit (IGSO), Geostationary Orbit (GEO), Initial Operational Capability (IOC), Full Operational Capability (FOC), Code Division Multiple Access (CDMA), and Frequency Division Multiple Access (FDMA).

System	GPS	GLONASS	BeiDou	Galileo
Country	USA	Russia	China	EU
Orbit	MEO (near) circular	MEO (near) circular	MEO (+IGSO+GEO) (near) circular	MEO (near) circular
Nominal constellation				
Number of satellites	24	24	27 (+3+5)	30
Number of planes	6	3	3	3
Inclination [°]	55	64.8	55	56
Altitude [km]	20180	19100	21530 (35786)	23222
IOC	1993	1993	2012	2016
FOC	1995	1995 / 2011[1]	2020	-
Signal characteristics				
Frequencies [MHz]	L1: 1575.42 L2: 1227.60 L5: 1176.45	L1: 1602.00 L2: 1246.00 L3: 1202.025	B1: 1561.098 B2: 1207.14 B3: 1268.52	E1: 1575.42 E5a: 1176.45 E5b: 1207.14 E6: 1278.75
Signal type	CDMA	FDMA (later +CDMA)	CDMA	CDMA

Service (SPS) became available. Full Operational Capability (FOC) was then achieved once the Precision Positioning Service (PPS) was online in 1995.

The legacy GPS signals are L1 and L2. The legacy SPS uses a coarse-acquisition (C/A) code on L1, while the PPS uses a more precise and encrypted (P/Y) code on both L1 and L2 (Teunissen and Montenbruck, 2017, Chapter 1). GPS has undergone several modernizations over its different generations referred to as "blocks" (Teunissen and Montenbruck, 2017, Chapter 7). For civilians, the upgrades include the L2C signal added to Block IIR-M in 2005, a third L5 signal added to Block IIF in 2010, and the L1C signal added to GPS III in 2018. All three of these are not yet fully operational at the moment of writing. Block IIR-M also introduced the new military (M) code, which is meant to be more robust against jamming. The M code was accepted as operational for early use in 2020. Block III satellites are still being launched, while their "follow-on" Block IIIF is currently under development.

Galileo

Galileo is a joint venture between the European Commission (EC) and the European Space Agency (ESA) (Teunissen and Montenbruck, 2017, Chapter 9). The development of Galileo began in 2003 and started with the In-Orbit Validation (IOV) phase. First, experimental satellites GIOVE-A and GIOVE-B were launched in 2005 and 2008, respectively, followed by four IOV satellites launched in pairs in 2011 and 2012. Since then, Full Operational Capability (FOC) satellites have been launched, starting in 2014 and most recently in 2021. Initial Operational Capability (IOC) was achieved in December 2016. In April 2024 there were 23 operational Galileo satellites in orbit. Since then, four of the remaining FOC satellites were launched in pairs in April 2024 and September 2024, while the development of the next generation of Galileo has recently begun.

[1]The GLONASS constellation was declared fully operational for the first time in 1995. Shortly after, the system deteriorated, resulting in only seven active satellites by 2001. After being prioritized again, the constellation regained full-operational status with 24 satellites in 2011 (Teunissen and Montenbruck, 2017, Chapter 8).

Galileo offers several services, both currently available and planned for the future. The most relevant ones for this work include the Open Service (OS) and the High Accuracy Service (HAS). The OS is the publicly accessible positioning service consisting of data-pilot signal pairs on the E1 and E5 frequencies (Teunissen and Montenbruck, 2017, Chapter 9). The HAS provides real-time PPP corrections for free through the E6 signal as well as over the Internet (European Union, 2022), with its initial services beginning in January 2023 (European Commission and Space, 2023). The full service aims to provide 95% horizontal and vertical accuracies of 20 cm and 40 cm globally within 5 minutes. The corrections currently provided include orbit, clock, and code bias corrections for GPS and Galileo satellites.

2.1.2. Observables

This section describes the various fundamental GNSS observables, namely pseudoranges and carrier-phase measurements, as defined in Teunissen and Montenbruck (2017). It can be noted that Doppler measurements are also GNSS observables, though these were not utilized in this thesis and are therefore not discussed.

Pseudorange Measurements

Pseudoranges are a measurement of the apparent signal travel time from the satellite to the receiver[2]. As previously described, transmitted GNSS signals are modulated with specific codes. A code consists of a certain number and pattern of “chips” at a set chip length, with the transmitted code being repeated at a set interval longer than the code duration itself. Receivers generate local replicas of these codes, which are then aligned with the received signals. The shift needed to align the local and received signals is a measure of the signal travel time, and can be determined at sub-chip resolution. Multiplying this measured travel time with the speed of light gives a pseudorange. It is an apparent range and not the true range due to offsets in the receiver and satellite clocks from the system time of a given GNSS, as well as other errors and delays (Teunissen and Montenbruck, 2017, Chapter 19). Depending on the application, errors can either be estimated or corrected for, where the correction can be done either from external data or through modelling.

Accordingly, a pseudorange measurement can be expressed by its observation equation, as shown in Equation 2.1 following the formulation given in Teunissen and Montenbruck (2017, Chapter 19). The terms of this equation are briefly mentioned below.

$$p_{r,j}^{s}(t) = \rho_r^s(t) + \xi_{r,j}^{s}(t) + \left(d_{r,j} - d_j^s\right) + \left(dt_r(t) - dt^s(t) + \delta t^{\mathrm{rel}}(t)\right) + I_{r,j}^{s}(t) + T_r^s(t) + e_{r,j}^{s}(t) \tag{2.1}$$

- The times t in seconds are specific epochs, where it can be noted that indices such as t_E and t_A for the time of emission and the time of arrival, respectively, have been omitted for simplicity.
- The indices s, r, and j refer to a specific **(transmitting) satellite**, **receiver**, and **signal** respectively.
- Each of the terms are considered in units of meters.
- $\rho_r^s(t)$ is the **geometric range**, with the Euclidean norm of a vector defined as $\|\cdot\| = \sqrt{(\cdot)^\top(\cdot)}$ where $(\cdot)^\top$ is the transpose of a vector, between the satellite's center of mass at the signal emission time t_{E} and the receiver's antenna reference point at the signal arrival time t_{A}, defined here in the Earth-Centered Inertial (ECI) frame:

$$\rho_r^s(t_E, t_A) = \left\| \boldsymbol{r}^s\left(t_{\mathrm{E}}\right) - \boldsymbol{r}_r\left(t_{\mathrm{A}}\right) \right\| \tag{2.2}$$

  - $\boldsymbol{r}^s = [x^s, y^s, z^s]^\top$ is the satellite position vector.
  - $\boldsymbol{r}_r = [x_r, y_r, z_r]^\top$ is the receiver position vector.

[2]In literature, it is common to use the terminology “satellite” for the transmitter and “receiver” for the user since most GNSS applications consider ground users. In this case, there are also LEO satellites under consideration, which are both receivers of MEO GNSS signals as well as transmitters to ground users. Therefore, this ambiguity between a LEO satellite as a transmitter or receiver should be noted, as well as the ambiguity between a MEO or a LEO satellite. In general, when discussing observations, the term “satellite” will refer to the transmitting satellite, and “receiver” can refer to either a ground or space receiver. It is chosen to maintain this terminology to be consistent with existing literature.

- $\xi^s_{r,j}(t)$ is a term to correct for the **phase-center offsets** for the transmitting and receiving antennas for code observations.
- $d_{r,j}$ and d^s_j represent receiver and satellite **code hardware delays** respectively[3]. It can be noted that this formulation follows that of Teunissen and Montenbruck (2017, Chapter 19), in which these delays are assumed to be time-invariant over short periods of time (hours or days). In reality, these delays can be varying due to temperature changes in the electrical components.
- $dt_r(t)$ and $dt^s(t)$ are the respective receiver and satellite **clock offsets** from the system time of the given GNSS.
- $\delta t^{\mathrm{rel}}(t)$ includes both **relativistic effects**, namely the relativistic delay due to space-time curvature and the relativistic clock correction:

$$\delta t^{\mathrm{rel}}(t_E, t_A) = \delta t^{\mathrm{rel}}_{\mathrm{stc}}(t_E, t_A) - \delta t^{\mathrm{rel}}_{\mathrm{clk}}(t_E) \tag{2.3}$$

- $I^s_{r,j}(t)$ and $T^s_r(t)$ account for the atmospheric effects, namely the (slant) **ionospheric delay** and **tropospheric delay** respectively.
- The term $e^s_{r,j}(t)$ considers the **receiver noise**, which can be considered random with a zero-mean normal distribution, and the **multipath** effect for **code** observations[4].

As mentioned, the pseudorange is obtained from an apparent time of flight measurement. The geometric range, in turn, calls for the satellite position at the (true) emission time, as shown in Equation 2.2. The emission time can be approximated with the travel time τ as $t_{\mathrm{E}} \approx t_{\mathrm{A}} - \tau$. However, the travel time is also unknown, as it is a function of the geometric range itself: $\tau(t_A) \approx \rho^s_r(t_E, t_A)/c$. Using $\tau \approx 0$ and thus $t_E \approx t_A$, along with an initial guess for receiver position, the travel time can first be approximated as $\tau \approx \rho^s_r(t_A, t_A)/c$. This can then be iterated upon to further refine the geometric range estimate (Teunissen and Montenbruck, 2017, Chapter 19 & 21).

As mentioned, the positions given in Equation 2.2 are defined in the ECI frame. The Earth's rotation during the signal travel time must be taken into account when using the Earth-Centered Earth-Fixed (ECEF) frame. Following Teunissen and Montenbruck (2017, Chapter 19 & 21), this can be done as shown in Equation 2.4, assuming $t_{\mathrm{E}} \approx t_{\mathrm{A}} - \tau$ and using the rotation matrix $\mathbf{R}(t)$ as defined in Equation 2.5 with Earth's rotation rate $\omega_\oplus$ in rad/s. In the second line of Equation 2.4, the property $\mathbf{R}(t_{\mathrm{A}} - \tau) = \mathbf{R}(t_{\mathrm{A}})\,\mathbf{R}(-\tau)$ is used considering that a common rotation can be taken out of the norm. Alternatively, the Sagnac correction shown in Equation 2.6 can be applied to the geometric range directly, where $\cdot$ is the inner product and $\times$ is the outer product.

$$\begin{aligned} \rho^s_r(t_{\mathrm{A}} - \tau, t_A) &= \left\| \mathbf{R}(t_{\mathrm{A}} - \tau)\, \boldsymbol{r}^s_{\mathrm{ECEF}}(t_{\mathrm{A}} - \tau) - \mathbf{R}(t_A)\boldsymbol{r}_{r,\mathrm{ECEF}}(t_A) \right\| \\ &\cong \left\| \mathbf{R}(-\tau)\, \boldsymbol{r}^s_{\mathrm{ECEF}}(t_{\mathrm{A}} - \tau) - \boldsymbol{r}_{r,\mathrm{ECEF}}(t_A) \right\| \end{aligned} \tag{2.4}$$

$$\mathbf{R}(t) = \begin{bmatrix} +\cos(\omega_\oplus t) & +\sin(\omega_\oplus t) & 0 \\ -\sin(\omega_\oplus t) & +\cos(\omega_\oplus t) & 0 \\ 0 & 0 & 1 \end{bmatrix} \tag{2.5}$$

$$\Delta\rho^s_r = \frac{1}{c}\left(\boldsymbol{r}_r(t_{\mathrm{A}}) - \boldsymbol{r}^s(t_{\mathrm{E}})\right) \cdot \left(\omega_\oplus \times \boldsymbol{r}_r(t_{\mathrm{A}})\right) \tag{2.6}$$

Carrier-Phase Measurements

Similar to the pseudorange (code) measurements, the receiver also generates a replica of the carrier signal, which can be aligned to the received carrier signal. This provides a carrier-phase measurement, namely the fractional phase shift between the local and received carrier phases. As this is continuously measured, the receiver can also count the number of complete cycles that have elapsed during the tracking. With a wavelength of approximately 19-25 cm, carrier-phase measurements offer a higher precision than pseudoranges. However, these measurements are ambiguous, as the number of integer

[3] Sometimes the term **instrumental** is used instead of hardware, and **biases** instead of delays.

[4] This formulation is consistent with that presented in Teunissen and Montenbruck (2017, Chapter 19), though in other literature the effects of multipath and receiver (thermal) noise are sometimes listed separately in the observation equations.

cycles at the start of the tracking is unknown. The corresponding observation equation is presented in Equation 2.7 (Teunissen and Montenbruck, 2017, Chapter 19), along with its terms further described afterwards.

$$\begin{aligned}\varphi^s_{r,j}(t) = \rho^s_r(t) + \zeta^s_{r,j}(t) + \left(\delta_{r,j} - \delta^s_j\right) + \left(dt_r(t) - dt^s(t) + \delta t^{\text{rel}}(t)\right) - I^s_{r,j}(t) + T^s_r(t) \\ + \lambda_j\left(\omega^s_r(t) + N^s_{r,j}\right) + \varepsilon^s_{r,j}(t)\end{aligned} \tag{2.7}$$

- The indices s, r, and j refer to a specific **(transmitting) satellite**, **receiver**, and **signal** respectively.
- Each of the terms are considered in units of meters, except for the ambiguities $N^s_{r,j}$ which are considered in units of cycles.
- Terms equivalent to those presented for the pseudorange observation in Equation 2.1 are:
  - The **geometric range** $\rho^s_r(t)$.
  - The respective **receiver** and **satellite clock offsets** $dt_r(t)$ and $dt^s(t)$.
  - The **tropospheric delay** $T^s_r(t)$.
- Similar yet differing terms as compared to those for pseudoranges are:
  - The **phase-center offset** correction $\zeta^s_{r,j}(t)$ for the transmitting and receiving antennas for phase observations.
  - The **phase hardware delays** $\delta_{r,j}$ and δ^s_j for the **receiver** and **satellite** respectively, where the same assumption regarding the time-invariability as for the code hardware delays is also made here.
  - The term $\epsilon^s_{r,j}(t)$ gathers the **receiver noise** and **multipath** errors for phase observations, as done in Teunissen and Montenbruck (2017, Chapter 19).
- In the first order approximation, the **ionospheric delay** $I^s_{r,j}(t)$ has the same magnitude, but opposite sign as compared to pseudoranges.
- New terms as compared to the pseudoranges are:
  - The **phase wind-up correction** $\omega^s_r(t)$ accounting for the change in measured phase due to relative rotations of the antennas.
  - The **unknown integer ambiguity** $N^s_{r,j}$ counted in number of cycles, and then multiplied by the corresponding **wavelength** λ_j to obtain units of length.

Error Sources

More detailed descriptions of the various error sources that appear in the presented GNSS observables can be found in the literature study report, which are also based on Teunissen and Montenbruck (2017). An overview of the approximate magnitudes of each of these error sources can be seen in Table 2.2.

Table 2.2: Approximate magnitudes of GNSS observable error sources for a ground receiver, obtained from Teunissen and Montenbruck (2017, Chapter 1, 15, & 25). PCO and PCV stand for Phase-Center Offset and Variations respectively. It can be noted that the typical values for the code multipath error are mentioned, though in severe cases these can reach to 100 m.

Error source	Approximate magnitude	Error source	Approximate magnitude
Broadcast satellite orbit	0.2 – 1.0 m	Satellite PCV	5 – 15 mm
Broadcast satellite clock	0.3 – 1.9 m	Receiver PCO	5 – 15 cm
Relativistic effects: Eccentricity	10 – 20 m	Receiver PCV	up to 3 cm
Relativistic effects: J_2	2 cm	Differential code biases	up to 5 m
Ionospheric delay (1st order)	up to 30 m	Fractional phase biases	up to 0.5 cycles
Ionospheric delay (higher order)	0 – 2 cm	Code receiver noise	0.1 – 1.0 m
Tropospheric delay (dry)	2.3 m	Phase receiver noise	0.1 – 1.0 cm
Tropospheric delay (wet)	up to 0.3 m	Code multipath	0.2 – 1.0 m
Carrier-phase wind-up	10 cm	Phase multipath	0.1 – 1.0 cm
Satellite PCO	0.5 – 3 m		

2.2. Low Earth Orbit Positioning, Navigation, & Timing (LEO-PNT)

This section introduces the case for performing PNT from LEO, first starting with the motivation for such systems. Second, the currently proposed LEO-PNT concepts are briefly presented. Then, the relevant design considerations for the topic of this thesis are mentioned. Finally, the main LEO-PNT challenges are summarized.

2.2.1. LEO-PNT Motivation & Use Cases

As discussed in Section 2.1, most GNSS in operation today reside in MEO at an altitude of around 20,000 km and, in the case of BeiDou, with additional satellites in GEO and IGSO at 35,786 km. Currently, GNSS is the only global free positioning system, playing a critical role for many applications. However, GNSS signals arrive on Earth at very low power, making them vulnerable to (intentional) interference. In the last years, alternatives to GNSS have been sought after to cope with this vulnerability. One potential approach is to complement and augment the MEO GNSS by Low Earth Orbit (LEO) systems.

The first satellite navigation systems began in Low Earth Orbit (LEO); a brief description of their early history is given by Reid et al. (2020b). Broadly defined, LEO can range from about 200 to 2000 km in altitude (Teunissen and Montenbruck, 2017, Chapter 32). One of the main reasons for traditional GNSS opting for MEO is attributed to the larger footprint of MEO satellites on Earth, requiring less satellites to achieve global coverage. At present, thanks to a more diverse launch vehicle landscape and advancements in satellite technology, large constellations of LEO satellites have now become more realistically achievable (Reid et al., 2020b).

Accordingly, a rise in LEO satellite systems has been observed in recent years, mainly driven by the emergence of large LEO constellations for communication and broadband connectivity. Following this trend, LEO constellations for Positioning, Navigation, and Timing services (LEO-PNT) are also an emerging concept. Three types of implementations to perform PNT from LEO are defined below (Prol et al., 2022). It can be noted that this study will only focus on the last type, namely entire LEO constellations specifically designed for navigation purposes.

- **Signals of Opportunity (SOOP):** These are signals transmitted from LEO that are not specifically intended for PNT purposes, but can still be leveraged to obtain positioning information.
- **Modified payload:** In this case, an existing LEO transmitter, usually for satellite communication purposes, is modified to provide a specific positioning signal. This type is sometimes referred to as **fused PNT**.
- **Dedicated LEO-PNT systems:** These systems are specifically designed and optimized for the delivery of PNT services. This could be an entire satellite platform and/or constellation designed for PNT, in addition to a specific navigation payload. Alternatively, a **hosted payload** for PNT could be installed on satellites with other (additional) purposes, such as communication satellites.

PNT from LEO can benefit from several advantages over MEO. First, there is less free-space path loss due to its closer proximity to Earth. This leads to a higher signal-to-noise ratio offered by a LEO satellite when considering similar transmitters and receivers, as shown by Reid et al. (2020b). This can potentially improve resilience against interference, as well as improve navigation indoors and in urban environments. Second, satellites in LEO have a shorter orbital period and, thus, a larger angular rate. This means that LEO satellites traverse the local sky quicker, providing more rapidly changing geometries with respect to a ground user. Reid et al. (2020b) mention that this can potentially help to reduce the effect of multipath, as well as accelerate integer ambiguity resolution. This faster geometric change is especially expected to reduce the convergence time of Precise Point Positioning (PPP) (Ge et al., 2018), (Zheng et al., 2024). Another benefit highlighted by Reid et al. (2020b) is that LEO satellites are in a fairly lower radiation environment than the MEO satellites situated within the Van Allen belt, potentially allowing for leaner satellites to be employed (Ries et al., 2023).

Furthermore, with MEO being situated above LEO, signals from MEO GNSS can also be leveraged for LEO-PNT operations, such as for the Orbit Determination and Time Synchronization (ODTS) of the LEO satellites. Accordingly, a LEO-PNT layer could offer additional observations, both from LEO to ground as well as from MEO to LEO, in addition to the existing MEO to ground measurements. These additional observations could be employed not only to determine the LEO orbits and clocks (Kunzi et al., 2023), but also to improve this process for the MEO satellites (Li et al., 2019a). It can also be noted that Inter-Satellite Links (ISLs) could also be used to obtain additional observations between satellites. Finally, existing literature has also identified the case for a standalone LEO-PNT constellation to be used independently from MEO GNSS.

Considering all of these potential benefits and opportunities for LEO-PNT, it can be highlighted that this study will focus on the case of using LEO-PNT in addition to the existing MEO GNSSs to improve PPP performance. This means that a standalone LEO-PNT scenario is considered beyond the scope of this study. Lastly, the use of ISLs is also deemed beyond the scope of this study.
Considering the potential benefits and opportunities that LEO-PNT presents, this study will focus on LEO-PNT as an augmentation to existing MEO GNSS constellations to improve PPP performance for ground users. Given that applications on ground will continue to use GNSS, which is a well-established and widely deployed system, a standalone LEO-PNT scenario is not considered to be of interest for the case of improving PPP performance. Furthermore, the ODTS of MEO GNSS will not be investigated here, since the identified research gap is related to the on-board real-time POD of the LEO-PNT satellites, which is accordingly the focus of this study. Lastly, the use of ISLs is deemed beyond the scope of this thesis.

2.2.2. Proposed LEO-PNT Concepts

At the moment of writing, several concepts for LEO-PNT constellations have been initiated. Table 2.3 gives an overview of the main operational systems and dedicated concepts. It should be noted that these are snapshots in time of their proposed configurations, as most are in their early stages. Other concepts with less (public) information available, as well as single LEO-PNT experimental missions and multi-purpose LEO constellations including PNT services, are not included here for brevity.

Table 2.3: Overview of current operational and planned LEO-PNT concepts (FrontierSI, 2024). The "satellites launched" are considered as of the moment of writing.

Entity Type	Entity Name	Name / Description	Status	LEO-PNT Type	Satellites planned	Satellites launched
Commercial	Iridium Communications Inc.	STL	Operational	Modified payload	66	66
	Beijing Future Navigation Technology Company	CentiSpace	Planned	Dedicated	190	5 experimental
	Xona Space Systems	Pulsar	Planned	Dedicated	258	1 experimental
	TrustPoint	TrustPoint	Planned	Dedicated	300	2 experimental
Institutional	ESA (Europe)	LEO-PNT In-Orbit Demonstration	Planned	Demonstration	10	0
	JAXA (Japan)	LEO-PNT Constellation	Planned	Dedicated	up to 480	0

- **STL (Iridium Communications Inc.):** Besides Signals of Opportunity from existing communication constellations, there is also the Satellite Time and Location (STL) service implemented on board of Iridium NEXT satellites, which was originally developed by Satelles in partnership with Iridium Communications Inc. The STL service has been shown to provide positioning to 20 m accuracy and timing to within 1 μs in 'deep' indoor conditions (Reid et al., 2020b).
- **CentiSpace (Beijing Future Navigation Technology Company):** The CentiSpace constellation is planned by a Chinese company named Beijing Future Navigation Technology Co., Ltd. Current public plans describe three layers: 120 satellites at an altitude of 975 km and inclination of 55°, 30 satellites at an altitude of 1100 km and inclination of 87.4°, and 40 satellites at an altitude of

1100 km and inclination of 30° (Mu, 2023). Services aim to provide dm-level positioning globally in 5 seconds and cm-level positioning in 1 minute. Furthermore, five experimental satellites have been launched so far. The last four experimental satellites were placed at an altitude of 700 km and inclination of 54°and included payloads transmitting navigation signals on the L1 (1575.42 MHz) and L5 (1176.45 MHz) frequencies.

- **LEO-PNT In-Orbit Demonstration (ESA):** The European Space Agency (ESA) has conducted several studies and R&D activities related to PNT from LEO (Ries et al., 2023). ESA has announced plans for an in-orbit demonstration for LEO-PNT, with the aim of developing the necessary key technologies, performing tests in orbit, and consolidating the types of signals to be transmitted. At the moment of writing, the contracts for the demonstration mission of 10 satellites in total (Cordero et al., 2025) have recently been awarded by ESA and few technical details are publicly known.
- **Pulsar (Xona Space Systems):** Xona Space Systems, a USA-based startup, plans to construct a commercial LEO-PNT constellation named Pulsar. Their latest plans include a final constellation size of 258 LEO satellites rolled out over three phases in the coming years (Youn, 2023). Pulsar is mainly targeting navigation services suitable for autonomous vehicles, aiming to provide positioning accuracies of 5-10 cm at suitable convergence times (Reid et al., 2020a).
- **TrustPoint:** TrustPoint is another USA-based company aiming to provide a same-named commercial LEO-PNT service. Their constellation will be built up over several phases to a total of 288 satellites. Their planned services include GPS augmentation as well as GNSS-independent timing and positioning. TrustPoint plans to focus on operating in C-band frequencies, and specifically not in the L-band. They aim for <1 m accuracy, maturing to <10 cm over time (Anderson, 2023).
- **LEO-PNT Constellation (JAXA):** The Japan Aerospace Exploration Agency (JAXA) has recently announced the interest to construct a LEO-PNT constellation of up to 480 satellites, specifically mentioning the provision of rapid Precise Point Positioning (PPP) convergence for users (Murata et al., 2024).

2.2.3. Relevant LEO-PNT Design Considerations

As mentioned, this study will consider dedicated LEO-PNT systems. In traditional GNSS, the ground segment is tasked with monitoring and maintaining the space segment, including monitoring the health of the satellites and of their transmitted signals. These signals are also used to estimate the satellite orbit and clock deviations during the ODTS, which are provided to users through the routinely updated navigation message. For LEO-PNT, this process does not necessarily need to be performed with only measurements taken from the ground, as observations from GNSS receivers on board the LEO satellites can be used as well. This would require the design of an appropriate LEO ODTS strategy itself, including which types of measurements and models will be used, and where exactly certain corrections will be estimated (either on board or on ground). This thesis will focus on the orbit and clock corrections that can be estimated with on-board POD specifically.

There are a few more related design considerations that will briefly be mentioned here, though these topics themselves are not the main focus of this study. First is the constellation itself, namely type and number of orbital planes, their orbital parameters, and the number of satellites per plane. These choices will naturally impact the user positioning performances (Ge et al., 2020b), but also the operational requirements for tracking all of these satellites. Accordingly, the number and locations of the ground stations can be optimized based on the constellation configuration, as well as the estimation tasks to be carried out on the ground. Additionally, irrespective of how they are determined, the LEO-PNT corrections would likely be provided to users through the LEO navigation message. The format in which these ephemerides are provided to users, e.g. with Keplerian elements similar to MEO GNSS or not, is also an open topic in LEO-PNT due to the higher dynamics experienced in LEO (Prol et al., 2022).

Furthermore, if measurements gathered on board are to be used for the ODTS, then the choice in GNSS receiver and especially the choice in on-board clock are of importance. There are several challenges related to LEO-PNT clock estimation in general, which will be further addressed in Section 2.2.4. These can potentially be exacerbated if clocks that are lower in cost and size but also stability as compared to MEO GNSS are used, though steering using the GNSS receiver could also be employed (Reid et al., 2020b), (Ries et al., 2023), (Prol et al., 2022). Lastly, there is also the LEO-PNT signal design, and more specifically that the choice in carrier frequency is not necessarily trivial. Maintaining interoperability with GNSS for users by also using the L-band may be desired, though other options such as the S-, C-, Ku-, or Ka-bands have also been suggested (Prol et al., 2022), (Ries et al., 2023).

2.2.4. LEO-PNT Challenges

Besides the highlighted benefits and opportunities of LEO-PNT presented in Section 2.2.1, several challenges in achieving such a system are also present. General challenges naturally include the large number of satellites to be produced, launched, and maintained. Being closer to Earth, the LEO satellites will experience higher dynamics and more significant perturbations, including those from Earth's gravitational field and atmospheric drag. These factors lead to a less trivial scenario for the ODTS of a LEO-PNT system. With a constellation in the order of hundreds of satellites and overpass times of 15-20 minutes, an extensive global network of ground stations would be needed to copy the operations of the current MEO GNSS. With high operational costs, this scenario is not desirable. Due to the more perturbed dynamics, high-accuracy long-term predictions of the LEO orbits are not currently foreseen (Wang et al., 2023a), (Wang et al., 2023b).

This highlights the motivation to enhance the autonomy of LEO-PNT, namely by being able to perform the POD on board the satellites themselves without relying on an extensive ground tracking network. To this end, this study will focus on the on-board POD for LEO-PNT satellites, the details of which will be treated in the next chapters. It can be noted that the satellite orbit and clock data is needed to provide to users as navigation data, though other spacecraft operations such as orbit maintenance, collision avoidance, and scheduling in general can also benefit from the orbit and timing information through this increased on-board autonomy. Another challenge that can also be reiterated is how to provide the satellite ephemerides themselves to users, as the current format for MEO GNSS is also not sufficient for LEO-PNT.

Several additional challenges relating to the LEO clock estimation can also be highlighted. When using on-board POD, the LEO *receiver* clock offset is estimated, which will be biased by the *receiver* hardware biases according to the specific combination of signals used for the measurements. However, a user of LEO-PNT would need a LEO *transmitter* clock offset correction, which would be biased by the *transmitter* hardware biases (Wang and El-Mowafy, 2022), (Liu et al., 2024). Furthermore, a LEO-PNT system could be transmitting at different frequencies than the ones it has used as a receiver, further highlighting the potential difference in LEO receiver and transmitter biases and the need for corresponding corrections. As mentioned by Liu et al. (2024), on-ground calibration before launch could account for these corrections to a certain degree, though high-precision applications would also require in-orbit calibration. In the case of the transmitter biases specifically, these can likely only be estimated by receiving these signals on the ground.

3
Methods

Based on the research gap defined in Section 1.2, two main topics in this thesis can be identified. These are Precise Orbit Determination (POD) and Precise Point Positioning (PPP). This chapter provides the background on both of these methods in Section 3.1 and Section 3.2 respectively, as summarized from the corresponding literature study.

3.1. Precise Orbit Determination (POD)

As highlighted in the previous chapter, an important aspect of a LEO satellite navigation service is the means for performing its ODTS. This section covers the POD methods that can be used to achieve this. First, the desired aspects for LEO-PNT POD considered in this study are listed, followed by detailing the state-of-the-art that is in accordance with these specific aspects. Next, the various POD techniques are detailed, followed by the options for POD processing. Finally, some key aspects related to POD for LEO-PNT are highlighted.

3.1.1. Purpose

Users of space-based navigation services rely on the provision and accuracy of the transmitting satellites' orbital positions and clock offsets. Accordingly, the orbits and clocks of the LEO-PNT satellites transmitting navigation signals will also need to be determined. The following aspects are desired for the LEO-PNT Orbit Determination (OD) in the context of this study:

- **Precise:** As previously mentioned, one of the main potential benefits to be provided by LEO-PNT is to lower the time needed for Precise Point Positioning (PPP) convergence. For PPP, precise orbits and clocks are required (Teunissen, 2020), leading to the need for Precise Orbit Determination (POD) methods.
- **On-board:** Also, as introduced in Section 2.2, an extensive ground network would be needed to fulfill the orbit determination needs of a LEO-PNT constellation with many fast-passing satellites. As this would likely be quite costly, on-board POD is an attractive alternative to reduce the need to carry out the OD on the ground.
- **GNSS-based:** LEO satellites are situated within the GNSS Terrestrial Service Volume, offering quite favourable coverage and accuracy with respect to the cost as compared to other satellite tracking techniques (Teunissen and Montenbruck, 2017, Chapter 32). This has led to a rich implementation of GNSS receivers on LEO spacecraft to provide on-board navigation services, as further highlighted in Section 3.1.2, which can also be leveraged in LEO-PNT systems.
- **Real-time:** The usefulness of the PNT services to be provided by the LEO satellites depends not only on the quality of, but also the latency with which the LEO orbits and clocks are provided to users. Thus, the latency with which these corrections can be determined is also relevant. Therefore, real-time processing will be the focus of this study.

3.1.2. State-of-the-Art

Precise orbit determination entails estimating a satellite's position and velocity as accurately as possible. The need for POD of LEO satellites mainly began with the need for precise orbit knowledge of scientific missions, in which ground-based post-processing was usually sufficient. The maturation of space-based GNSS receivers has allowed this form of LEO POD to become widely implemented, with post-processed results using precise GNSS products reaching cm-level accuracies (Hauschild et al., 2022). As described in the previous section, this study aims to focus on POD that is not only GNSS-based but also performed on-board and in real-time. A brief review of the POD literature taking these considerations into account is described below.

Hauschild and Montenbruck (2021) describe how initial implementations of GPS-based real-time on-board POD were limited to around meter-level 3D errors when using only broadcast ephemerides due to their previously poorer quality. This led to several investigations into using precise GNSS orbit and clock products available to LEO satellites, such as from GEO relays, Satellite-Based Augmentation Systems (SBAS), and the planned Galileo High Accuracy Service (HAS). Hauschild and Montenbruck (2021) highlight that the reception of these precise GNSS products on board LEO satellites remains a complex and challenging task and accordingly revisit using only Broadcast Ephemerides (BCE) for real-time on-board POD. The study employs the reduced-dynamic technique through a Kalman-Filter (KF) based implementation. Using simulated dual-frequency Galileo and BeiDou-3 measurements, solutions around 8.5 cm 3D error were found and attributed to the improved BCE quality of these GNSS.

This performance of around 1 dm was confirmed in the study of Montenbruck et al. (2022) using actual flight data from the “PODRIX” dual-constellation (GPS and Galileo) receiver on board the Sentinel-6A satellite and employing a fairly similar POD method. In Hauschild et al. (2022), the added value of Galileo’s HAS was investigated based on initial test transmissions of the service. This study also used GNSS observations from the Sentinel-6A mission, along with GPS and Galileo corrections from HAS messages received at ground stations during the test period. Both a real-time KF implementation and a near-real-time short-arc Batch-Least-Squares (BLS) approach were considered for the POD processing strategies. The real-time results showed about a 5%, 10%, and 40% improvement in 3D position error when using Galileo-only, Galileo+GPS, and GPS-only, respectively.

3.1.3. Techniques

Traditionally, there are three types of techniques to perform precise orbit determination, namely Dynamic (DOD), Kinematic (KOD), and Reduced-Dynamic (ROD or RDOD). As described by Wu et al. (1990), the latter technique enforces a relative weighting between the former two techniques, allowing RDOD to achieve an optimal combination of KOD and DOD. For this reason, the reduced-dynamic method has been selected for this study. As mentioned in Montenbruck et al. (2008), RDOD has been demonstrated to be feasible for implementation on board of a spacecraft platform. Below, each of the three techniques are briefly introduced.

Dynamic

A spacecraft orbiting the Earth experiences several forces. Its trajectory can be described by equations of motion, which are second-order differential equations in which the accelerations a satellite experiences are related in time to its position, velocity, and the forces acting on it. In the dynamic orbit determination approach, the equations of motion using force models can be integrated at measurement times to constrain the estimated trajectory of the satellite (Wu et al., 1990). A detailed description of these spacecraft dynamics and physical force models can be found in Montenbruck and Gill (2000). In DOD, the accuracy depends on the quality of the employed models, with better models usually leading to increased computational complexity. This method benefits from improved resilience against measurement errors and outages. However, due to the unavoidable use of imperfect models, the orbit error will still tend to grow in time (Wu et al., 1990).

Kinematic

Compared to the dynamic method, kinematic orbit determination is a purely geometric method without any dynamical constraints. It entails instantaneous point positioning using (in this case) GNSS measurements, leading to synergies with PPP, which is covered in the next chapter. As such, the kinematic method is susceptible to more or less favorable satellite geometries, as well as measurement errors, noise, and outages. This leads to a need for proper pre-screening of the data to be used. In turn, KOD does not suffer from the effects of mismodelling or considerable computational complexities as the dynamic method does (Wu et al., 1990) and can, therefore, be more applicable in cases of limited resources and/or limited a priori orbit knowledge.

Reduced-Dynamic

The reduced-dynamic orbit determination method, first described by Wu et al. (1990), combines elements of both the dynamic and kinematic methods, capitalizing on the strengths of each a selective weighting strategy. This is complemented by introducing empirical accelerations to the estimation problem, which can absorb uncertainties from unmodeled forces. The tuning of their stochastic parameters controls their degree of flexibility in absorbing these uncertainties. An increased correlation time and a decreased steady-state standard deviation limits this flexibility, approaching the dynamic method. In turn, decreasing the correlation time and increasing the steady-state standard deviation indicate more uncertainties in the dynamical modeling. This allows to maintain a larger weighting of new observations, thereby approaching a more kinematic method. As such, carefully selecting the process noise values can provide an optimal weighting between the two methods. This provides accuracies at least as good as and usually better than the other two methods individually.

3.1.4. Processing Strategies & POD Tool Implementation

The reduced-dynamic orbit determination method was selected for this study. Accordingly, the `FAST` Extended Kalman Filter (EKF) and `RDOD` Batch Least-Squares (BLS) tools in GHOST (Wermuth et al., 2010) were used, as they are implemented in the reduced-dynamic sense. The implementation of these tools in GHOST (Helleputte, 2004) will be briefly summarized in this section, and are largely consistent with the description given in Montenbruck et al. (2005).

Solving the orbit determination problem in a least-squares sense involves estimating a number of parameters such that the sum of the squares of the differences between the measured and modelled observations in minimized. In other words, the least-squares solution gives an estimate for the parameters that allow a certain observation model to come as close to the actual measurements as possible. The general approach to setting up the system of equations to be solved can be described as follows. Starting from a vector $\boldsymbol{z}$ containing measured observations and a vector $\boldsymbol{h}$ containing modelled observations computed with a state vector $\boldsymbol{x}_0$ of the parameters to be estimated, their relation can be described as:

$$\boldsymbol{z} = \boldsymbol{h}\left(\boldsymbol{x}_0\right) + \epsilon \tag{3.1}$$

Here, ϵ accounts for the unknown measurement errors causing the difference between the observed and computed measurements. For non-linear observation equation, a first-order linearization can be performed about an initial guess $\boldsymbol{x}_0^{\mathrm{ref}}$, so that the least-squares adjustment can be applied:

$$\boldsymbol{z} \approx \boldsymbol{h}\left(\boldsymbol{x}_0^{\mathrm{ref}}\right) + \left.\frac{\partial \boldsymbol{h}}{\partial \boldsymbol{x}_0}\right|_{\boldsymbol{x}_0^{\mathrm{ref}}} \left(\boldsymbol{x}_0 - \boldsymbol{x}_0^{\mathrm{ref}}\right) + \epsilon \tag{3.2}$$

$$\Delta \boldsymbol{z} \approx \mathbf{H} \Delta \boldsymbol{x}_0^{\mathrm{ref}} + \epsilon \tag{3.3}$$

$$\Delta \boldsymbol{z} = \boldsymbol{z} - \boldsymbol{h}\left(\boldsymbol{x}_0\right) \qquad \mathbf{H} = \left.\frac{\partial \boldsymbol{h}\left(\boldsymbol{x}_0\right)}{\partial \boldsymbol{x}_0}\right|_{\boldsymbol{x}_0^{\mathrm{ref}}} \qquad \Delta \boldsymbol{x}_0 = \boldsymbol{x}_0 - \boldsymbol{x}_0^{\mathrm{ref}} \tag{3.4}$$

The least squares solution for $\Delta \boldsymbol{x}_0$ in Equation 3.3 represents the correction that can be applied to the initial guess that would approximately cover the discrepancy $\Delta \boldsymbol{z}$ between the observed and computed measurements.

In this case of dual-frequency GNSS-based POD, the observations consist of Ionosphere-Free (IF) pseudoranges and carrier phases, and are respectively modelled as follows:

$$p_r^s = \left\| r_{\mathrm{APC}}^s - r_{r,\mathrm{APC}} \right\| + c\, dt_r - c\, dt^s \tag{3.5}$$

$$\varphi_r^s = \left\| r_{\mathrm{APC}}^s - r_{r,\mathrm{APC}} \right\| + c\, dt_r - c\, dt^s + \lambda_j^S A_r^s \tag{3.6}$$

Here, $r_{r,\text{APC}}$ and r^s_{APC} are the positions of the receiver (S6A in this case) and the GNSS satellite antennas respectively, both considered from their respective Antenna Phase Centers (APC). Furthermore, dt_r and dt^s are receiver and satellite clock offsets respectively. The phase observations also contain the term A^s_r which represents the phase ambiguities. The terms for multipath, receiver biases, and noise are neglected. Furthermore, the tropospheric delay is not present as LEO satellites are above the troposphere. The receiver parameters and the ambiguities are estimated during the estimation procedure. The GNSS satellite position and clock values are obtained from the provided GNSS products, where a position correction is applied for the antenna offset if needed. The reference frame for the observation equations is tied to that of the GNSS products that are used, which is typically a realization of the Earth-Centered Earth-Fixed (ECEF) frame.

In the (reduced) dynamic method, force models are used to further constrain the orbit solution. An equation of motion for the satellite formulated with these models can be numerically integrated to propagate the satellite's state over a number of epochs. This propagated state can then be used as an input to the observation model. The orbital motion can be described using a second order differential equation, which is considered in the inertial International Celestial Reference Frame (ICRF):

$$\ddot{\boldsymbol{r}} = \boldsymbol{a}(t, \boldsymbol{r}, \boldsymbol{v}, \boldsymbol{p}) = \sum_i \boldsymbol{a}_i \tag{3.7}$$

Here, the acceleration $\boldsymbol{a}$ experienced by the receiver satellite is given as a function of time t, the position vector $\boldsymbol{r}$, the velocity vector $\boldsymbol{v}$, and additional force model parameters $\boldsymbol{p}$. This acceleration is composed of the various types of forces i that can be chosen to be included in the modelling. The forces that are used in GHOST include both gravitational and non-gravitational forces. The formulation of these models in GHOST is consistent with the descriptions given in Montenbruck and Gill (2000). The gravitational terms include Earth's gravity expressed in spherical harmonics, solid Earth and ocean tides, and point masses for the Sun and Moon. The non-gravitational terms include aerodynamic drag, solar radiation pressure, and Earth radiation pressure, as well as empirical accelerations in the RTN directions.

Based on the discussion so far, several types of parameters to be estimated in the orbit determination process can be defined, which are gathered in the state vector $\boldsymbol{x}$, as shown in Equation 3.8. These are the receiver position vector $\boldsymbol{r}$ and receiver velocity vector $\boldsymbol{v}$ (which together are referred to as $\boldsymbol{y}$), as well as a number of force model parameters $\boldsymbol{p}$ and measurement model parameters $\boldsymbol{q}$. The force model parameters consist of coefficients for the drag C_D, solar radiation pressure C_R, and Earth radiation pressure C_E, which are used as adjustable scaling factors to account for uncertainties and limitations in the employed models. Furthermore, the empirical accelerations $\boldsymbol{a}_{\mathbf{emp}}$ are also included here, which are specifically included to account for discrepancies in the other force models. The measurement model parameters in this case are the receiver clock dt_r and the phase ambiguities A^s_r.

$$\boldsymbol{x}(t) = [\boldsymbol{r}(t), \boldsymbol{v}(t), \boldsymbol{p}, \boldsymbol{q}]^\top \qquad \boldsymbol{y}(t) = [\boldsymbol{r}(t), \boldsymbol{v}(t)]^\top \tag{3.8}$$

The batch estimation (`RDOD`) involves setting up a system of equations in the form of Equation 3.3 that is built up using observations from all the epochs in the considered data arc. The parameters to be estimated in this method can be clarified as follows. First, it is the initial position $\boldsymbol{r}_0$ and velocity $\boldsymbol{v}_0$ that are to be estimated. Next, the empirical accelerations are defined as piecewise constant over intervals of a pre-defined length. Accordingly, the state vector includes the number of empirical acceleration parameters to be estimated based on these intervals. Furthermore, there is a receiver clock offset parameter for each measurement epoch. Finally, there is a phase ambiguity estimate for each continuous tracking interval of a given GNSS satellite.

The batch estimation process starts with first propagating the trajectory of the satellite across the entire data arc. This is done by numerically integrating the equation of motion starting from an initial guess for the parameters in the state vector. As shown in Equation 3.3, the partial derivatives of the observation equation with respect to the state vector must also be computed. Since the observation equation does not directly depend on the initial state and the force parameters, the variational equations can be used to link the state at a given epoch to the corresponding parameters, which follow from the chain rule as shown in Equation 3.9. These are known as the state transition matrix $\boldsymbol{\Phi}_y(t,t_0)$ and the sensitivity matrix $\mathbf{S}(t)$ shown in Equation 3.10. These variational equations are also propagated over the epochs to determine all the necessary partial derivatives, where more details on the formulation for this propagation can be found in Montenbruck and Gill (2000). As the observations are in ITRF and the equations of motion are in ICRF, the relevant transformations between these must also be considered in the propagation steps. The remaining partials for $\boldsymbol{q}$ are for the receiver clock offsets and phase ambiguities, which are respectively equal to 1 and -1 for the corresponding epochs where each of the parameters are present.

$$\mathbf{H} = \frac{\partial \boldsymbol{h}}{\partial \boldsymbol{x}_0} = \left[\begin{array}{ccc} \frac{\partial \boldsymbol{h}}{\partial \boldsymbol{y}(t_0)} & \frac{\partial \boldsymbol{h}}{\partial \boldsymbol{p}} & \frac{\partial \boldsymbol{h}}{\partial \boldsymbol{q}} \end{array}\right] = \left[\begin{array}{ccc} \frac{\partial \boldsymbol{h}}{\partial \boldsymbol{y}(t)} \cdot \frac{\partial \boldsymbol{y}(t)}{\partial \boldsymbol{y}(t_0)} & \frac{\partial \boldsymbol{h}}{\partial \boldsymbol{y}(t)} \cdot \frac{\partial \boldsymbol{y}(t)}{\partial \boldsymbol{p}} & \frac{\partial \boldsymbol{h}}{\partial \boldsymbol{q}} \end{array}\right] \tag{3.9}$$

$$\boldsymbol{\Phi}_y(t,t_0) = \frac{\partial \boldsymbol{y}(t)}{\partial \boldsymbol{y}(t_0)} \qquad \mathbf{S}(t) = \frac{\partial \boldsymbol{y}(t)}{\partial \boldsymbol{p}} \tag{3.10}$$

The resulting system of equations in the form of Equation 3.3 then consists of the residuals between the observations and observation equations computed with the propagated state, along with the corresponding computed partial derivatives, for all the epochs in the considered arc. The solution that is then computed can be described as a weighted least-squares solution using a priori information, which is formulated in Equation 3.11. Here, the weight matrix $\mathbf{W}$, which is the inverse of the measurement covariance matrix, is used to account for the accuracy of the different types of measurements. Furthermore, a measure of the levels of uncertainty of the various parameters in the initial guess can be taken into account by using an information matrix which is the inverse of the matrix of covariances of these a priori parameters $\boldsymbol{\Lambda} = \left(\mathbf{P}^{\text{apr}}\right)^{-1}$.

$$\boldsymbol{\Delta}\hat{\boldsymbol{x}}_0 = \left(\boldsymbol{\Lambda} + \mathbf{H}^\top \mathbf{W}\mathbf{H}\right)^{-1}\left(\boldsymbol{\Lambda}\,\boldsymbol{\Delta}\boldsymbol{x}_0 + \mathbf{H}^\top \mathbf{W}\boldsymbol{\Delta}\boldsymbol{z}\right) \tag{3.11}$$

The resulting normal equations consist of sparsely filled matrices, meaning large parts of the matrices are empty. There are special techniques for solving these types of matrices more efficiently, more details on how this is done in GHOST can be found in Montenbruck et al. (2005). As mentioned, the obtained solution represents the correction to be applied to the initial guess for the state vector. The process can be repeated after this correction is applied, and after several iterations the solution can converge.

As mentioned, the sequential estimation tool (FAST) uses a Kalman filter, which recursively estimates the instantaneous state of a linear dynamic system by adjusting modelled state predictions with noisy measurements. This is done in two steps: first the time update step for the state propagation, followed by the measurement update step for the correction. As described above, for the case of GNSS-based POD, the system must first be linearized. Furthermore, the GHOST implementation makes use of an *extended* Kalman filter (EKF), in which the linearization and propagation is performed at each epoch using the current (updated) state estimate, instead of first propagating the trajectory over the entire arc.

The state vector used in the EKF consists of the same types of parameters as those presented in Equation 3.8. In this case, the position and velocity estimates pertain to the current epoch, and all the parameters are estimated at each epoch. Furthermore, the covariance matrix $\mathbf{P}$ contains the variances of the parameters on the diagonal and a measure of the correlations between them in the off-diagonal terms. This matrix is used as a measure for how the uncertainties in the state parameters vary as they are propagated and updated. In the time update step, the state vector and the covariance matrix are first propagated from epoch $i-1$ to epoch i as shown in Equation 3.12 and Equation 3.13 respectively (Montenbruck and Gill, 2000, Chapter 8).

$$\boldsymbol{x}_i^- = \boldsymbol{x}\left(t_i; \boldsymbol{x}(t_{i-1}) = \boldsymbol{x}_{i-1}^+\right) \tag{3.12}$$

$$\mathbf{P}_i^- = \boldsymbol{\Phi}_i \mathbf{P}_i^+ \boldsymbol{\Phi}_i^\top + \mathbf{Q}_i \tag{3.13}$$

$$\boldsymbol{\Phi}_i = \boldsymbol{\Phi}(t_i, t_{i-1}) = \frac{\partial \boldsymbol{x}_i^-}{\partial \boldsymbol{x}_{i-1}^+} \tag{3.14}$$

Here, the superscripts $-$ and $+$ denote predicted and updated states respectively. The filter is initiated with the a priori values $\boldsymbol{x}_0 = \boldsymbol{x}_0^{\mathrm{apr}}$ and $\mathbf{P}_0 = \mathbf{P}_0^{\mathrm{apr}}$. The state is propagated by (numerically) integrating the previously introduced equation of motion using the previous state update. The covariance matrix is propagated through multiplication with the state transition matrix as defined in Equation 3.14. Here, the covariance will increase due to state uncertainties growing during the (imperfect) propagation step. The term $\mathbf{Q}$ is for the addition of process noise and will be explained below.

In the measurement update step, first the Kalman gain matrix $\mathbf{K}$ is calculated, as shown in Equation 3.15. This can be seen as balancing the weight between the propagation and the measurements. Somewhat similar to the BLS approach, the matrix $\mathbf{W}$ contains the measurement weights and $\mathbf{G}$ contains the partial derivatives of the observation equation with respect to the estimated state vector. The Kalman gain matrix is then used to update the predicted state as shown in Equation 3.16, essentially mapping the residuals, taken as the difference between the modelled observations $\boldsymbol{g}(\boldsymbol{x})$ and the actual observations $\boldsymbol{z}$, into a state correction. The covariance matrix is also updated using the Kalman gain, where the addition of the information from the measurements results in a decrease of the uncertainties.

$$\mathbf{K}_i = \mathbf{P}_i^- \mathbf{G}_i^\top \left(\mathbf{W}_i^{-1} + \mathbf{G}_i \mathbf{P}_i^- \mathbf{G}_i^\top\right)^{-1} \tag{3.15}$$

$$\boldsymbol{x}_i^+ = \boldsymbol{x}_i^- + \mathbf{K}_i \left(\boldsymbol{z}_i - \boldsymbol{g}_i\left(\boldsymbol{x}_i^-\right)\right) \tag{3.16}$$

$$\mathbf{P}_i^+ = \left(\mathbf{1} - \mathbf{K}_i \mathbf{G}_i\right) \mathbf{P}_i^- \tag{3.17}$$

This systematic decrease in state uncertainty over time leads to a smaller weight being attributed to the measurements in the Kalman gain matrix. This can increasingly shift the trust to the state propagation and neglect the contribution of new measurements, which can lead to divergence in the estimated state over time. This is solved by adding process noise $\mathbf{Q}$, which artificially re-introduces a level of uncertainty to $\mathbf{P}$ to avoid this divergence from happening. The process noise represents the stochastic model discrepancies (Montenbruck and Gill, 2000, Chapter 8) for the parameters described below. The values selected for the process noise can ultimately steer the filter towards a more dynamical (no process noise) or more kinematic (infinite process noise) solution.

In `FAST`, process noise is added for the empirical accelerations, the receiver clock estimate, and the phase ambiguities. For the empirical accelerations, a first order Gauss-Markov process model is applied, where more details on this can be found in (Montenbruck et al., 2005). This Gauss-Markov process has an exponentially decaying auto-correlation in time, which will reach the selected process noise (steady state variance) level σ^2 after a selected time interval τ. The receiver clock and phase ambiguities in turn are modelled according to a random walk process (Montenbruck and Ramos-Bosch, 2008).

3.1.5. LEO-PNT Key Aspects

One of the main purposes of performing the on-board POD for the LEO-PNT satellites is to generate orbit and clock corrections for users. Several key aspects of LEO POD that are of relevance to ground user performance can be highlighted:

- **Accuracy:** As seen in traditional GNSS positioning, the accuracy of the satellite orbits and clocks directly influences the user positioning performance. This will naturally also be the case when using LEO-PNT satellites. This makes the accuracy of the LEO POD of interest, especially when considering what is achievable with the on-board resources. Accordingly, this aspect has been selected as one of the main focuses of this study.
- **Latency:** As briefly mentioned, there will be a latency between the computation of the orbit solution and its dissemination to users. This latency will also impact user positioning. This study will address the latency of the computation time, as it is related to POD processing strategy and setup. In turn, the latency in providing the LEO corrections to users is not addressed in the current study.

Some additional aspects that are not specifically addressed in this work but would also be important for future LEO-PNT systems are:

- **LEO satellite code & phase biases:** Besides the satellite orbits and clocks, the satellite hardware delays (biases) would also be needed by the user to be able further achieve precise positioning. As mentioned in Section 2.2.4, there is a distinction between the LEO *receiver* clock offset that could be estimated on-board, and the LEO *transmitter* clock offset that ground users need. Additionally, there may be differences in the signal frequencies used for on-board clock estimation and those used for LEO navigation signal transmission, which can further contribute to this distinction. As the transmitter biases can only be estimated by receiving the signals, this would likely need to be done by a ground segment, which then can regularly provide the estimated biases to the LEO satellites to be included in their broadcast message. Since on-board POD is the focus of this study, this aspect is not specifically investigated here.
- **Satellite attitude:** GNSS satellites follow a specific variation in their attitude to be able to maintain their operations, namely mainly to keep their solar panels oriented towards the Sun to be able to generate power while also maintaining the nadir-pointing navigation transmission. In traditional GNSS, this attitude information can also be provided to users to improve their knowledge of the satellite's orientation. At this moment, it is not known whether the LEO-PNT satellites will also be following a complex attitude law and, therefore, also require the provision of such information. Therefore, this aspect is also not considered in the present study.

3.2. User Precise Positioning

This section will cover the user positioning methods themselves. This will build from first the "simpler" Single Point Positioning (SPP) presented in Section 3.2.1, followed by the more Precise Point Positioning (PPP) covered in Section 3.2.2. The concept of Ambiguity Resolution within Precise Point Positioning (PPP-AR) will be briefly introduced in Section 3.2.3, though it can already be noted that the use of PPP-AR has been deemed beyond the scope of this thesis. Finally, how LEO-PNT can potentially impact the user positioning is treated in Section 3.2.4.

3.2.1. Single Point Positioning (SPP)

Single Point Positioning (SPP) can generally achieve positioning accuracies of <10 m (Teunissen and Montenbruck, 2017, Chapter 21). It uses **only code (pseudorange) observations** measured by one receiver. The satellite orbit, clock, bias, and atmospheric corrections can be obtained from the broadcasted navigation message or external sources. The SPP strategies can be based on single, dual, or multi-frequency observations, and one or more GNSS constellation(s) can be used. As these strategies employ linear estimation methods, first the linearized (code) observation equation is presented, based on the formulation given by Teunissen and Montenbruck (2017, Chapter 21). There are a few differences with respect to the previously presented non-linear Equation 2.1; these are listed below, along with the explanations of the additional new terms.

$$\begin{aligned}\Delta p_{r,j}^{s}(t) = &- \left[\boldsymbol{e}_{LOS,r}^{s}(t)\right]^{\top} \Delta\boldsymbol{r}_{r}(t) + \Delta T_{r}^{s}(t) + \Delta dt_{r}(t) + \left[\Delta d_{r,j}^{\mathrm{S}}(t)\right] \\ &- \left[\Delta dt^{s}\left(t-\tau_{r}^{s}\right) - \Delta d_{j}^{s}\left(t-\tau_{r}^{s}\right)\right] + \mu_{j}^{\mathrm{S}} \Delta I_{r}^{s}(t) + e_{r,j}^{s}(t)\end{aligned} \tag{3.18}$$

- The indices s, r, j, and S refer to a specific **satellite**, **receiver**, **signal (frequency)**, and **GNSS constellation** respectively.
- The Δ notation indicates so-called **incremental parameters** that correspond to $\Delta(\cdot) = (\cdot) - (\cdot)|_0$, with the **original** parameter $(\cdot)$ and its **approximate** value $(\cdot)|_0$. This *observed-minus-computed* format of the observation equation results from the linearization process.
- $\boldsymbol{e}_{LOS,r}^{s}(t)$ is the **line-of-sight (LOS) unit vector** in units of meters and is expressed as follows:

$$\boldsymbol{e}_{LOS,r}^{s}(t) = \frac{\left[\boldsymbol{r}^{s}\left(t-\tau_{r}^{s}\right) - \boldsymbol{r}_{r}(t)\right]}{\left\|\boldsymbol{r}^{s}\left(t-\tau_{r}^{s}\right) - \boldsymbol{r}_{r}(t)\right\|} \tag{3.19}$$

  - $\boldsymbol{r}^s = [x^s, y^s, z^s]^\top$ is the satellite position vector in units of meters.
  - $\boldsymbol{r}_r = [x_r, y_r, z_r]^\top$ is the receiver position vector in units of meters.
  - τ_r^s is the signal travel time in seconds.

- Compared to the equation found in Teunissen and Montenbruck (2017, Chapter 21), the code interchannel bias term $\Delta\Delta d^s_{r,j}(t)$ is omitted in this report, as it is only needed when using FDMA-based systems such as GLONASS, which will not be considered in this study since LEO-PNT systems are not foreseen to use FDMA.
- The differences as compared to Equation 2.1 are:
  - The phase center offset correction $\xi^s_{r,j}(t)$ and the relativistic term $\delta t^{\mathrm{rel}}(t)$ are not shown as these are deterministic terms that are corrected for.
  - The satellite code hardware bias $d^s_j\,(t - \tau^s_r)$ is preceded by the opposite sign, chosen in Teunissen and Montenbruck (2017, Chapter 21) to be consistent with the IGS convention.
  - The (first-order, slant) ionospheric delay is expressed using the **ionospheric coefficient** μ^{S}_j, which corresponds to:

$$I^s_{r,j}(t) = \mu^{\mathrm{S}}_j I^s_{r,1}(t) \tag{3.20}$$

$$\mu^{\mathrm{S}}_j = \left(\frac{\lambda^{\mathrm{S}}_j}{\lambda^{\mathrm{S}}_1}\right)^2 = \left(\frac{f^{\mathrm{S}}_1}{f^{\mathrm{S}}_j}\right)^2 \tag{3.21}$$

As mentioned above, both single or dual frequencies and constellations can be employed in SPP. This choice impacts the formulation of the SPP model and which parameters can be estimated. As adapted from Teunissen and Montenbruck (2017, Chapter 21):

- **Single frequency, single constellation:** The estimated parameters are the receiver position and the estimable receiver clock error, which is the actual receiver clock error biased by the receiver code hardware delay. Corrections for the satellite orbits, clocks, code hardware biases, and atmospheric effects are used in this case. In SPP, these are usually obtained from the broadcast ephemeris. The satellite clocks from the broadcast are provided in the Ionosphere-Free (IF) combination, which is based on two frequencies. This IF satellite clock is correspondingly biased by the IF satellite code hardware delay. Since this is based on two frequencies, Single-Frequency (SF) users must correct this. In this case, the Differential Code Bias (DCB) or Timing Group Delay (TGD, a scaled version of the DCB)[5] is needed, where the DCB is the difference between the satellite code hardware delays corresponding to specific frequencies.
- **Dual frequency, single constellation:** When using two frequencies, the ionospheric delay can either be eliminated or estimated. In the case of eliminating, the model is similar to the single-frequency case, though now with IF observations and IF parameters. In the case of estimating the slant ionospheric delay, this becomes an additional parameter in a model similar to the SF case, though this model is rank deficient and cannot directly be used in a least-squares adjustment. This can be overcome by using specific linear combinations of parameters that result in a full rank system. The resulting estimable parameters are then the receiver position parameters, the estimable receiver clock error biased by the IF receiver code hardware bias, and the estimable ionospheric delay biased by the DCB.
- **Single frequency, dual constellation:** When considering two constellations with a single frequency from each, it is common practice to choose one system time to reference the receiver clock error to. The estimable receiver clock is then biased by that system's receiver code hardware delay. For this to match the observations of the second system as well, an additional parameter appears. This is the Inter-System Bias (ISB), which considers the differences between the receiver code hardware biases of the two systems. The estimable ISB parameter is biased by the difference between the two time systems themselves, known as the system time offset. Alternatively, a receiver clock error for each constellation can be estimated, instead of estimating just one receiver clock error and the ISB.

[5] It can be noted that for Galileo, these are often referred to as Broadcast Group Delays (BGD) instead.

- **Dual frequency, dual constellation:** Using two frequencies introduces the possibility of estimating the ionospheric delay while using two constellations introduces the additional ISB parameter. For the case of positioning with two constellations using two frequencies from each one, both of these types of corresponding estimable parameters are present. The receiver clock is once again ionosphere-free and referenced to the time of the first system. Each system then has its own estimable ionospheric delay parameters, biased by the corresponding DCBs. The ISB is then formulated as IF as well, while still biased by the system time offset.

Considering the descriptions provided above, the dual-frequency and dual-constellation SPP model can be formulated as shown below, followed by an explanation of each of the present terms. The remaining models can be found in Teunissen and Montenbruck (2017, Chapter 21), along with the corresponding mathematical formulations of each of their estimable parameters.

$$E\left(\begin{bmatrix} \Delta\tilde{\boldsymbol{p}}^{\mathrm{A}}_{r,1}(t) \\ \Delta\tilde{\boldsymbol{p}}^{\mathrm{A}}_{r,2}(t) \\ \Delta\tilde{\boldsymbol{p}}^{\mathrm{B}}_{r,1}(t) \\ \Delta\tilde{\boldsymbol{p}}^{\mathrm{B}}_{r,2}(t) \end{bmatrix}\right) = \begin{bmatrix} \mathbf{G}^{\mathrm{A}}_r(t) & \boldsymbol{u}_{m_\mathrm{A}} & \mu^{\mathrm{A}}_1\mathbf{I}_{m_\mathrm{A}} & 0 & 0 \\ \mathbf{G}^{\mathrm{A}}_r(t) & \boldsymbol{u}_{m_\mathrm{A}} & \mu^{\mathrm{A}}_2\mathbf{I}_{m_\mathrm{A}} & 0 & 0 \\ \mathbf{G}^{\mathrm{B}}_r(t) & \boldsymbol{u}_{m_\mathrm{B}} & 0 & \mu^{\mathrm{B}}_1\mathbf{I}_{m_\mathrm{B}} & \boldsymbol{u}_{m_\mathrm{B}} \\ \mathbf{G}^{\mathrm{B}}_r(t) & \boldsymbol{u}_{m_\mathrm{B}} & 0 & \mu^{\mathrm{B}}_2\mathbf{I}_{m_\mathrm{B}} & \boldsymbol{u}_{m_\mathrm{B}} \end{bmatrix} \begin{bmatrix} \Delta\boldsymbol{r}_r(t) \\ d\tilde{t}^{\mathrm{A}}_r(t) \\ \tilde{\boldsymbol{I}}^{\mathrm{A}}_r(t) \\ \tilde{\boldsymbol{I}}^{\mathrm{B}}_r(t) \\ \mathrm{ISB}^{\mathrm{AB}}_{r,\mathrm{IF}} \end{bmatrix} \tag{3.22}$$

- $E(\cdot)$ denotes the expectation operator.
- The following indices are present:
  - s and r respectively refer to a specific **satellite** and **receiver** .
  - 1 and 2 respectively refer to the **first** and **second signals (frequencies)** of a constellation.
  - A and B respectively refer to a **constellation A** and a **constellation B**.
- m_A and m_B denote the **number of tracked satellites** for each corresponding constellation.
- $\Delta\tilde{\boldsymbol{p}}^{\mathrm{S}}_{r,j}(t)$ are vectors of size m_S containing the **(observed-minus-computed) code observations** in units of meters for the corresponding signals j and constellations S, where the tilde denotes that these are **corrected** observations.
- The matrices $\mathbf{G}^{\mathrm{S}}_r(t) = \left[-\boldsymbol{e}^1_{LOS,r}(t), \ldots, -\boldsymbol{e}^{m_\mathrm{S}}_{LOS,r}(t)\right]^\top$, containing the **line-of-sight (LOS) unit vectors** $\boldsymbol{e}^s_{LOS,r}(t)$ in units of meters between a corresponding satellite s and the receiver r.
- $\boldsymbol{u}_{m_\mathrm{S}} = [1, \ldots, 1]^\top$ are vectors of **ones** of the size m_S.
- μ^{S}_j are the **ionospheric coefficients** as shown in Equation 3.21 and $\mathbf{I}_{m_\mathrm{S}}$ are **identity matrices** of size m_S.
- The parameters, all given in units of meters, are:
  - The **receiver position vector increment** $\Delta\boldsymbol{r}_r(t)$.
  - The **estimable (ionosphere-free) receiver clock error** $d\tilde{t}^{\mathrm{A}}_r(t)$:

$$d\tilde{t}^{\mathrm{A}}_r(t) = dt^{\mathrm{A}}_r(t) + d^{\mathrm{A}}_{r,\mathrm{IF}} \tag{3.23}$$

  - Vectors of the **estimable ionospheric delays** $\tilde{\boldsymbol{I}}^{\mathrm{S}}_r(t) = \left[\tilde{I}^1_r(t), \ldots, \tilde{I}^{m_\mathrm{S}}_r(t)\right]^\top$, which are biased by the DCBs, which are both given in units of meters:

$$\tilde{I}^s_r(t) = I^s_r(t) - \frac{1}{\mu^{\mathrm{S}}_2 - \mu^{\mathrm{S}}_1}\,\mathrm{DCB}^{\mathrm{S}}_{r,12} \tag{3.24}$$

$$\mathrm{DCB}^{\mathrm{S}}_{r,12} = d^{\mathrm{S}}_{r,1} - d^{\mathrm{S}}_{r,2} \tag{3.25}$$

  - The **estimable ionosphere-free ISB**, biased by the **system time offset** t^{AB}, in units of meters:

$$\mathrm{ISB}^{\mathrm{AB}}_{r,\mathrm{IF}} = \left[d^{\mathrm{B}}_{r,\mathrm{IF}} - d^{\mathrm{A}}_{r,\mathrm{IF}}\right] - t^{\mathrm{AB}} \tag{3.26}$$

- It can be noted that an **ionosphere-free** hardware delay (whether satellite or receiver) in units of meters is made from the following **combination**:

$$d_{\mathrm{IF}}(t)=\frac{\mu_2^{\mathrm{S}}}{\mu_2^{\mathrm{S}}-\mu_1^{\mathrm{S}}}d_1(t)-\frac{\mu_1^{\mathrm{S}}}{\mu_2^{\mathrm{S}}-\mu_1^{\mathrm{S}}}d_2(t)=d_j(t)+\frac{\mu_j^{\mathrm{S}}}{\mu_2^{\mathrm{S}}-\mu_1^{\mathrm{S}}}\underbrace{\left[d_1(t)-d_2(t)\right]}_{\mathrm{DCB}_{12}(t)} \tag{3.27}$$

- It can also be noted that the SPP formulations in Teunissen and Montenbruck (2017, Chapter 21) did not include the tropospheric delay, which they attribute to the fact that this can largely be corrected for by models.

3.2.2. Precise Point Positioning (PPP)

Building on what has been described so far, Precise Point Positioning (PPP) entails using **carrier phase observations** in addition to the previously presented pseudoranges, as well as **precise products for the corrections**, such as those provided by the International GNSS Service (IGS). The corrections are first determined by a reference network and then transmitted to the users to include these products in their PPP process. According to the theory presented in Teunissen and Montenbruck (2017), the linearized phase observation equation is first presented below. For brevity, only new symbols and considerations are clarified afterwards.

$$\begin{aligned}\Delta\varphi_{r,j}^{s}(t)=&-\left[\boldsymbol{e}_{LOS,r}^{s}(t)\right]^{\top}\Delta\boldsymbol{r}_r(t)+\Delta T_r^s(t)+\left[c-\dot{\rho}_r^s(t)\right]\Delta dt_r(t)+c\left[\Delta\delta_{r,j}^{\mathrm{S}}(t)\right]\\&-c\left[\Delta dt^s\left(t-\tau_r^s\right)-\Delta\delta_j^s\left(t-\tau_r^s\right)\right]-\mu_j^{\mathrm{S}}\Delta I_r^s(t)+\lambda_j^S\Delta N_{r,j}^s+\varepsilon_{r,j}^s(t)\end{aligned} \tag{3.28}$$

- Compared to the equation found in Teunissen and Montenbruck (2017, Chapter 21), the phase interchannel bias term $\Delta\Delta\delta_{r,j}^{s}(t)$ is omitted in this report, as it is only needed when using FDMA-based systems such as GLONASS, which will not be considered in this study since LEO-PNT systems are not foreseen to use FDMA.
- The differences as compared to Equation 2.7 are:
  - The phase center offset correction $\zeta_{r,j}^{s}(t)$, the relativistic term $\delta t^{\mathrm{rel}}(t)$, and the phase wind-up correction $\omega_r^s(t)$ are not shown as these are deterministic terms that are corrected for.
  - The satellite phase hardware bias $\delta_j^s\left(t-\tau_r^s\right)$ is preceded by the opposite sign, chosen in Teunissen and Montenbruck (2017, Chapter 21) to be consistent with the IGS convention.

The precise corrections include the GNSS satellite orbits and clocks, of which the clocks are defined according to ionosphere-free (IF) combinations of signals in the case of IGS products. Single-frequency users will also require DCBs and potentially ionospheric delay corrections. In PPP, the tropospheric delays are often also parameterized in addition to using a-priori tropospheric corrections, leading to an additional estimable parameter for the troposphere in the PPP model. The a-priori correction usually addresses the hydrostatic (dry) component as this can be modelled with high accuracy, while the estimable part is usually meant to account for the wet component that is much more difficult to model accurately (Teunissen and Montenbruck, 2017, Chapter 6 & 25).

Similarly to SPP, both one or more frequencies and/or constellations can be considered in a PPP model. In general, the presence of phase observations introduces two additional types of parameters: the receiver phase hardware bias and the phase ambiguities. Since this results in a linearly dependent system, specific linear combinations of parameters must be defined to ensure a full-rank system. Although certain biases are then lumped into the estimable parameters, the observation equations remain correctly formulated and consistent with the model when fully written out. The exact formulation of each estimable parameter (i.e., which bias terms are present), including the estimable receiver clock, depends on the type of model employed, considering the number of frequencies, number of constellations, and whether the ionospheric delay is corrected for or estimated.

A general form of the dual-frequency PPP model is presented below in Equation 3.29, obtained from Teunissen and Montenbruck (2017, Chapter 21). Here, only new symbols are briefly described below. It can be noted that only observations from a single constellation are included for simplicity, multi-constellation considerations are similar to those described in Section 3.2.1. As mentioned, the **phase ambiguities** are also estimable parameters. Though these are integers, they are not estimable as such, as they are **biased by the satellite hardware delays**. This leads to longer convergence times when using PPP, about 30 minutes for static PPP and 60 minutes for kinematic PPP to reach accuracies of <1 dm (Teunissen and Montenbruck, 2017, Chapter 21).

$$\left(\left[\begin{array}{c} \Delta\tilde{\boldsymbol{p}}_{r,1}(t) \\ \Delta\tilde{\boldsymbol{p}}_{r,2}(t) \\ \hline \Delta\tilde{\boldsymbol{\varphi}}_{r,1}(t) \\ \Delta\tilde{\boldsymbol{\varphi}}_{r,2}(t) \end{array}\right]\right) = \left[\begin{array}{ccccccc} \mathbf{G}_r(t) & \boldsymbol{u}_m & \mathbf{0} & \mathbf{0} & \mu_1\mathbf{I}_m & \mathbf{0} & \mathbf{0} \\ \mathbf{G}_r(t) & \boldsymbol{u}_m & \mathbf{0} & \mathbf{0} & \mu_2\mathbf{I}_m & \mathbf{0} & \mathbf{0} \\ \hline \mathbf{G}_r(t) & \boldsymbol{u}_m & \boldsymbol{u}_m & \mathbf{0} & -\mu_1\mathbf{I}_m & \lambda_1\mathbf{C}_m & \mathbf{0} \\ \mathbf{G}_r(t) & \boldsymbol{u}_m & \mathbf{0} & \boldsymbol{u}_m & -\mu_2\mathbf{I}_m & \mathbf{0} & \lambda_2\mathbf{C}_m \end{array}\right] \left[\begin{array}{c} \boldsymbol{x}_r(t) \\ d\tilde{t}_r(t) \\ \tilde{\delta}_{r,1} \\ \tilde{\delta}_{r,2} \\ \tilde{\boldsymbol{I}}_r(t) \\ \tilde{\boldsymbol{N}}_{r,1} \\ \tilde{\boldsymbol{N}}_{r,2} \end{array}\right] \tag{3.29}$$

- The index r refers to a specific **receiver**, while the indices 1 and 2 denote the various **signals (frequencies)** that can be included in the model. The index m refers to the **total number of observed satellites**.
- All parameters are given in units of meters, apart from the phase ambiguities, which are considered in units of cycles.
- $\Delta\varphi_{r,j}(t)$ are the **(observed-minus-computed) phase observations** for the corresponding signals j.
- Following the formulation presented in Teunissen and Montenbruck (2017, Chapter 21), the vector $\boldsymbol{x}_r(t)$ contains the Zenith Tropospheric Delay (ZTD) parameter along with with the position vector:

$$\boldsymbol{x}_r(t) = \left[\Delta\boldsymbol{r}_r(t)^\top, T_r^z(t)\right]^\top \tag{3.30}$$

  - This corresponds to the following formulation to map the tropospheric delay to the local zenith, with the a-priori tropospheric correction $T^s_{\mathrm{r},0}(t)$ and the mapping function $m_r^s(t)$. As previously mentioned, the a-priori correction usually accounts for the dry component of the tropospheric delay, while the estimable parameter usually accounts for the wet component.

$$T_r^s(t) = T^s_{\mathrm{r},0}(t) + m_r^s(t)T_r^z(t) \tag{3.31}$$

  - Accordingly, the matrices $\mathbf{G}_r(t) = \left[\boldsymbol{g}_r^1(t), \dots, \boldsymbol{g}_r^m(t)\right]^\top$ have the form:

$$\boldsymbol{g}_r^s(t) = \begin{bmatrix} -\boldsymbol{e}^s_{LOS,r}(t) \\ m_r^s(t) \end{bmatrix} \tag{3.32}$$

- The matrices $\mathbf{C}_m$ are of size $m \times (m-1)$ and are **identity matrices with the p-th column removed**, where p corresponds to the satellite designated as the ***pivot satellite***, which is used in the expression of the estimable parameters. Using a pivot satellite is a strategy to address rank deficiency by estimating ambiguity parameters as "between-satellite differences" relative to the pivot satellite, rather than estimating the undifferenced ambiguities directly (Teunissen and Montenbruck, 2017, Chapter 21).
- $\tilde{d}_{r,j}$ are the **additional estimable satellite code hardware delays**, for each additional frequency $j \geq 3$.
- $\tilde{\delta}_{r,j}$ are the **estimable satellite phase hardware delays** for each frequency j.
- $\tilde{\boldsymbol{N}}_{r,j}$ are vectors of the $(m-1)$ **estimable phase ambiguity parameters** for each frequency j, namely excluding that of the pivot satellite p:

$$\tilde{\boldsymbol{N}}_{r,j} = \left[\tilde{N}^1_{r,j}, \dots, \tilde{N}^{p-1}_{r,j}, \tilde{N}^{p+1}_{r,j}, \dots, \tilde{N}^m_{r,j}\right]^\top \tag{3.33}$$

3.2.3. Precise Point Positioning Ambiguity Resolution (PPP-AR)

As mentioned, the estimable phase ambiguities contain the satellite code and phase hardware biases and are consequently not integer estimable in the PPP model. This leads to the PPP Ambiguity Resolution (PPP-AR) method, in which **corrections for these satellite biases** are provided so that the integer ambiguities can be obtained, enabling quicker convergence. The satellite bias corrections are determined by a reference network and subsequently provided to users. The various methods in which the PPP-AR can be parameterized to resolve the integer ambiguities are considered beyond the scope of this thesis, though more information on these methods can be found in Teunissen and Montenbruck (2017). A distinction can also be noted here between PPP-AR and PPP-RTK (Real-Time Kinematic), namely that the latter also includes precise (local) atmospheric corrections, though this distinction is not uniform across literature. It can again be noted here that there is no established way to determine LEO-PNT satellite code and phase biases other than using a ground segment.

3.2.4. Impact of LEO-PNT on User Positioning

This subsection examines the impact of including LEO-PNT observations for SPP, PPP, and PPP-AR users based on commonly used navigation performance concepts and the existing LEO-PNT studies that have been reviewed. A more detailed synthesis of the results presented in the reviewed literature was summarized in the literature study corresponding to this thesis.

SPP

A common quantity for navigation performance is the navigation error as the product of the Dilution of Precision (DOP) and the User Equivalent Range Error (UERE) (Teunissen and Montenbruck, 2017). The UERE further consists of the Signal-in-Space Range Error (SISRE) and the User Equipment Error (UEE). The SISRE takes the space and control segment errors into account, while the UEE accounts for the user-specific errors. The DOP reflects the impact of the geometry between the satellites and receiver, see Figure 3.1, where favourable geometries correspond to lower DOP values. The DOP can provide an indication of the (SPP) performance improvement (Teunissen and Montenbruck, 2017) when including a LEO constellation.

In general, one can expect that additional satellites in orbits different from traditional GNSS will diversify the geometry and provide extra observations. However, the challenge with LEO-PNT lies in the smaller footprint of the satellites due to their closer proximity to Earth, leading to the need for many satellites in cleverly placed orbits to achieve consistent global coverage. Li et al. (2019c), Su et al. (2019), and Hong et al. (2023) showed decreasing DOPs with increasing numbers of LEO satellites. Ge et al. (2020b) showed that the performance can be evened out across all latitudes by using a combination of orbital inclinations in addition to increasing the number of satellites. Su et al. (2019) also directly evaluated the performance of SPP with a single GNSS constellation and 120 LEO satellites, noting a relatively moderate improvement in positioning accuracy. These were improvements of about 4-34% with North, East, and Up components still in the order of 0.9-2.9 m.

Figure 3.1: 2D representation of Dilution of Precision (DOP) for different relative satellite geometries, where the strips indicate the uncertainty in range to a specific satellite. A smaller overlap area of these strips corresponds to a lower DOP and a lower uncertainty in user position.

PPP

As described so far, one of the main expected advantages of LEO-PNT satellites compared to their MEO GNSS counterparts is their more rapid geometrical variations. It is foreseen that this can mainly help to improve the PPP convergence times, which has subsequently been the topic of many LEO-PNT studies so far. One of the first studies to investigate this was conducted by Ge et al. (2018) using an Iridium-like constellation of 66 LEO satellites. The best improvements reduced PPP convergence times from 25-35 minutes to only 5 minutes. However, from this study, it already becomes apparent that when using only polar orbiting satellites at lower numbers (<100 LEO satellites), the improvement at lower latitudes remains fairly limited, only improving from 38 to 30 minutes in this study.

This is further confirmed by Li et al. (2019c), showing improvements from 7.4 to 0.6 minutes and 15.4 to 2.4 minutes for high and low latitudes respectively, when adding 288 LEO satellites to PPP with GPS, GLONASS, Galileo, and BDS (GREC). This study also showed a 6.5-minute convergence time when using 192 LEO satellites without any MEO GNSS. Ge et al. (2020b) shows a more evened-out PPP convergence across latitudes when using a combination of inclinations, achieving 1.1 minutes over all latitudes with GREC and 240 LEO satellites. The studies of Su et al. (2019), Hong et al. (2023), and Li et al. (2023) show similar achievements, namely that **PPP convergence times in the order of 1-3 minutes can be achieved at all latitudes when augmenting both single and multi-GNSS with around 150+ LEO satellites**. Single-GNSS augmentation experiences the best improvement, usually from around 15-30 minutes, while multi-GNSS usually starts at 10-15 minutes.

Xu et al. (2024) and Li et al. (2024) are the first studies to assess LEO-augmented PPP convergence using actual observations from experimental CentiSpace satellites that are in orbit. A modest improvement in convergence time was demonstrated, as these studies only use additional observations from one and two LEO satellites respectively. The best PPP convergence was around 5.7 minutes when using GEC multi-GNSS, an improvement from 14.2 minutes. Some of the mentioned studies also looked into the potential improvement in PPP positioning accuracy, though only fairly modest improvements were found, further reinforcing the idea that one of the main benefits of LEO-PNT for PPP lies in the reduction in its convergence time.

PPP-AR

As described, PPP-AR involves the resolution or "fixing" of the integer ambiguities, which can provide even better positioning performance. Some studies have also investigated the potential impact of LEO-PNT on PPP-AR. A common performance metric reported in these studies is the "Time To First Fix" (TTFF)[6]. Hong et al. (2023) and Li et al. (2023) have looked into using the additional LEO observations to improve the ambiguity resolution for GNSS specifically. Both of these studies indeed found reductions in TTFF compared to situations without LEO-PNT. Li et al. (2023) did show that the improvement in TTFF was less pronounced compared to the improvement in convergence time of the regular PPP. Furthermore, the study also noted a reasonably limited improvement in terms of positioning accuracy itself. The study of Xu et al. (2024) based on actual measurements also found a PPP-AR improvement in TTFF when using additional observations from the LEO satellites.

Based on the slightly more limited improvements seen in literature for both SPP and PPP-AR, it was chosen to for float-PPP the main focus of this study in terms of user positioning performance. More specifically, the potential reduction in PPP convergence time was identified as one of the main topics of interest. However, one of the key aspects to be addressed in this research is also whether the magnitude of LEO satellite orbit and clock errors could possible degrade the PPP convergence time and positioning accuracy. Having provided the relevant background information, the subsequent chapters will present the new research that was conducted during this thesis.

[6]It should be noted that these studies use the term 'Time To First Fix' (TTFF) to denote the time needed to fix the phase ambiguities, though the use of the term Time To First Fix in the field of GNSS typically refers to the time needed for a receiver to provide its first position solution (Teunissen and Montenbruck, 2017, Chapter 18). Furthermore, the exact definition of this TTFF (of ambiguities) differs in each referenced study. In this subsection, the use of TTFF when referring to the time needed to fix the phase ambiguities is used anyway to maintain consistency with the literature being referred to.

4
Mission & Data

This chapter presents the various sources of data that were used in this study. In Section 4.1, Sentinel-6A is introduced as the selected representative LEO mission with a brief overview of the mission and its data. Then, in Section 4.2, the various GNSS products are presented and analyzed.

4.1. Sentinel-6A Mission & Data

As there were no known dedicated LEO-PNT satellites in orbit with publicly available data at the time of this thesis, a representative LEO mission with real and available GNSS measurements had to be selected. The Sentinel-6 "Michael Freilich" satellite was identified as a suitable candidate, as its mean orbital altitude is 1336 km and it is equipped with a dual-constellation GNSS receiver providing high-quality measurements that are made publicly available. Also known as Sentinel-6A (S6A), it was the first and is currently the only satellite in orbit for the Sentinel-6 mission, which is part of the Copernicus program. Sentinel-6 uses radar altimetry for ocean surface topography monitoring, and serves as a continuation of the TOPEX/Poseidon and Jason missions (Donlon et al., 2021). An overview of the Sentinel-6A mission characteristics is given in Table 4.1.

The satellite carries a number of POD instruments, as accurate orbit solutions are essential to meeting its science objectives. This includes two redundant "PODRIX" multi-frequency GPS/Galileo receivers (Peter et al., 2022a), which can track up to 24 satellites in single frequency or up to 18 satellites in dual frequency (Donlon et al., 2021). An overview of the signals that can be tracked by S6A's PODRIX is shown in Table 4.2. The default signal tracking configuration for GPS consists of the L1 C/A code for all satellites, the L2C signal for the modernized GPS satellites (IIR-M, IIF, III), and L1 P(Y) and L2 P(Y) for the legacy satellites (IIR). For Galileo, the E1 and E5a pilot signals are tracked, and it can be noted that the unusable satellites E14 and E18 are not tracked by S6A's PODRIX (Montenbruck et al., 2022). The types of data relating to Sentinel-6A used in this study can be listed as follows:

- **GNSS measurements:** This data is available on the Copernicus Data Space Ecosystem (CDSE) platform. These are daily files in RINEX format generated by the Copernicus POD Service (CPOD) (Fernández et al., 2024). It can be noted that the data includes both code and carrier measurements using the first four GPS signals presented in Table 4.2, as well as for both of the Galileo signals.
- **Satellite quaternions:** This data provides the necessary attitude information that is a prerequisite for performing POD. The quaternions are also generated by CPOD from on-board star tracker measurements (Fernández et al., 2024) and made available on the CDSE in daily files.
- **Spacecraft description:** Spacecraft information such as the mass, center of mass, surface data, antenna positions, and antenna phase center corrections are also needed for the POD processing. These were provided by researchers from DLR (Calliess et al., 2024) in a format already compatible with the GHOST POD software (Wermuth et al., 2010), with more up to date values for the mass, center of mass, and maneuvers obtained from the International DORIS Service (IDS) data center. It can be noted that no maneuvers took place over the period considered in this study, which will be presented in the next section.

- **Precise reference orbits:** These are also made available under the name "Precise Orbit Ephemeris" (POE) on the CDSE. They are provided in daily files that have been generated by CNES. The precise S6A orbits are used in this work as a reference to compare POD solutions to. In addition, a reference trajectory is also needed as an input to GHOST's POD functions for data editing purposes. The POE products can be used for this, circumventing the need for additional steps within the POD processing chain.

Table 4.1: An overview of the characteristics of the Sentinel-6A mission (Donlon et al., 2021), which has been selected as a suitable reference mission for this study due to its orbit and its publicly available GNSS measurements and spacecraft data.

Mission purpose	Ocean surface topography	**Launch**	21 Nov. 2020
Nominal lifetime	5 years	**Operated by**	EUMETSAT
Orbit type	LEO, non sun-synchronous	**Inclination**	66°
Mean altitude	1336 km	**Orbital period**	112.4 min
Orbit repeat cycle	9.92 days	**POD instruments**	GPS+Galileo, DORIS, SLR

Table 4.2: An overview of the frequencies that can be tracked by the PODRIX receiver on the Sentinel-6A satellite, as presented in Fernández et al. (2024). The default configuration consists of L1 C/A for all GPS satellites, L1 P(Y) and L2 P(Y) for the legacy GPS satellites, L2C for the modernized GPS satellites, and both signals for the Galileo satellites.

Constellation	Signal	GNSS Blocks	Code tracking
GPS	L1 C/A	All	
	L1 P(Y)	IIR, IIR-M, IIF, III	Semi-codeless
	L2 P(Y)	IIR, IIR-M, IIF, III	Semi-codeless
	L2-CL	IIR-M, IIF, III	Long
	L5-Q	IIF, III	Pilot
Galileo	E1-C	All	BOC (1,1) pilot
	E5-Q	All	Pilot

4.2. GNSS Products

The quality of GNSS orbit and clock products plays an important role in the overall achievable accuracy of GNSS-based POD. In particular, POD conducted on-board and in real-time is ultimately limited by the quality of the broadcast ephemerides (Montenbruck et al., 2022). Options for precise correction data that can be delivered to LEO satellites remain fairly limited at the moment of writing. Currently, the only freely and globally available option for this is Galileo's High Accuracy Service (HAS) (Hauschild et al., 2022). Accordingly, the GNSS products selected for this study are listed and described below, where the abbreviation for each product that will be used in the remainder of this report is given between brackets.

- **CODE MGEX Final products (COD):** The Center for Orbit Determination in Europe (CODE) is one of the global analysis centers that contributes to the International GNSS Service (IGS) and produces precise GNSS products (Prange et al., 2020). The Multi-GNSS EXperiment (MGEX) was launched in 2012 by the IGS to prepare services for the upcoming GNSS and RNSS, such as Galileo and BeiDou, as well as to adapt to modernisations occurring in GPS and GLONASS (Prange et al., 2017). The CODE MGEX solution comprises the five systems of GPS, GLONASS, Galileo, BeiDou, and QZSS (Dach et al., 2024). The CODE MGEX final orbit and clock products are used in this study as precise references to assess the quality of the real-time products listed below. Furthermore, these products are also used as inputs for the Sentinel-6A POD to illustrate the best possible accuracy that can be achieved with the implemented POD method.

- **CNES Real-Time products (CRT):** The Centre National d'Études Spatiales (CNES) is also one of the global analysis centers participating in the IGS services. Due to the high demand for real-time precise corrections, the IGS began providing its Real-Time Service (RTS) in 2013 (Li et al., 2022). The RTS consists of a global network of analysis centers that broadcast State Space Representation (SSR) corrections for the navigation messages over the Internet. CNES consolidates their real-time corrections into daily products which are publicly stored online in SP3 and CLK formats (Laurichesse, 2011). For this reason, these products were chosen to be used as a reference for the quality of products that can be generated and disseminated in real-time. However, it should be noted that in this case, there is currently no dedicated free service that could provide the CNES corrections to LEO satellites in (near) real-time.

- **Galileo High Accuracy Service Signal-In-Space (HAS):** As previously introduced, HAS provides GPS and Galileo corrections in real-time through the E6 signal (Naciri et al., 2023). As these corrections are globally transmitted by the Galileo constellation, this makes HAS a feasible solution for the direct provision of precise orbit and clock products to LEO satellites in real time. In practice, HAS corrections are provided in an SSR format packaged into HAS messages according to a specific strategy (Hauschild et al., 2022), which are then embedded in the CNAV navigation message on the E6-B signal. For this study, ESA was able to provide orbit and clock product files in SP3 and CLK format which already had the HAS corrections applied. These were provided for a limited number of days, dictating the seven-day data period of DOY 118 to 124 (27 April 2024 to 3 May 2024) used in this study.

- **Broadcast Ephemerides (BRD):** GNSS satellite orbit and clock data is available to LEO satellites through the broadcast ephemerides in the navigation message. Though these are not as precise as the aforementioned products, recent studies have shown to achieve suitable results when using the broadcast ephemerides for RT POD, as discussed in Section 3.1.2. Accordingly, these products are also used in this study and thus serve as a lower performance limit that can be achieved with the implemented POD method. The IGS maintains daily data files for the broadcast ephemerides of the various constellations in RINEX3 format.

4.2.1. CRT & HAS Availability

The data period selected for this study is DOY 118 to 124 in 2024. For CRT and HAS products, the availability of the orbit and clock corrections for each GNSS satellite was evaluated across the given data period. For the HAS products, it can be noted that two distinct data sets were provided by ESA, which will be referred to as HAS Batch 1 and HAS Batch 2, according to the order that they were provided in. The sampling rate for Batch 1 was 50 seconds for the orbits and 10 seconds for the clocks, which correspond to the data rates of the SSR corrections in the HAS stream (Hauschild et al., 2022). These rates were lower for Batch 2, namely at 5 minutes for the orbits and 30 seconds for the clocks.

Upon analyzing the first batch of data, it was noticed that there were significant gaps in its availability. This was particularly for most of the GPS satellites during the last two hours of each day, as well as more frequent gaps for all GPS satellites on DOY 123 and 124. This prompted the provision of a second batch from ESA, which did not exhibit these same periodic data gaps for GPS. The differences between the availability of the batches in time for the considered data period can been seen in Figure 4.1 and Figure 4.2 for the orbit and clock products respectively. Besides the periodic gaps in Batch 1, it can be seen that both batches experience intermittent gaps throughout the day, again mostly for GPS satellites. The behavior of intermittent gaps in HAS corrections is also recognized in other studies such as Naciri et al. (2023).

For both batches, it can be seen that the PRNs E14, E18, G01, G13, G22 are missing entirely. Satellites E14 and E18 have been set as "unusable" since February 2021, while G01 was set to "unusable" on 22 April 2024. G13 and G22 in turn were flagged as healthy during the considered period. The average availability percentage for each constellation during this period can be seen in Table 4.3, where the healthy satellites were included in the calculation, while the unusable satellites were not. Batch 2 shows a better average GPS availability than Batch 1, improving from around 82% to 88-90% for both orbits and clocks, while the Galileo availability in both batches remains high at

98-99%. However, it can be noted that due to the downsampling of the Batch 2 products, it could be that some of the shorter gaps from Batch 1 are potentially being interpolated over. Zhou et al. (2024) report similar average availabilities of 86.9% and 91.7% for GPS and Galileo respectively, where some PRNs were missing for multiple days at a time or from their entire data period as well. In this case, there were also Galileo satellites missing for days at a time, leading to its lower average availability as compared to the values reported here.

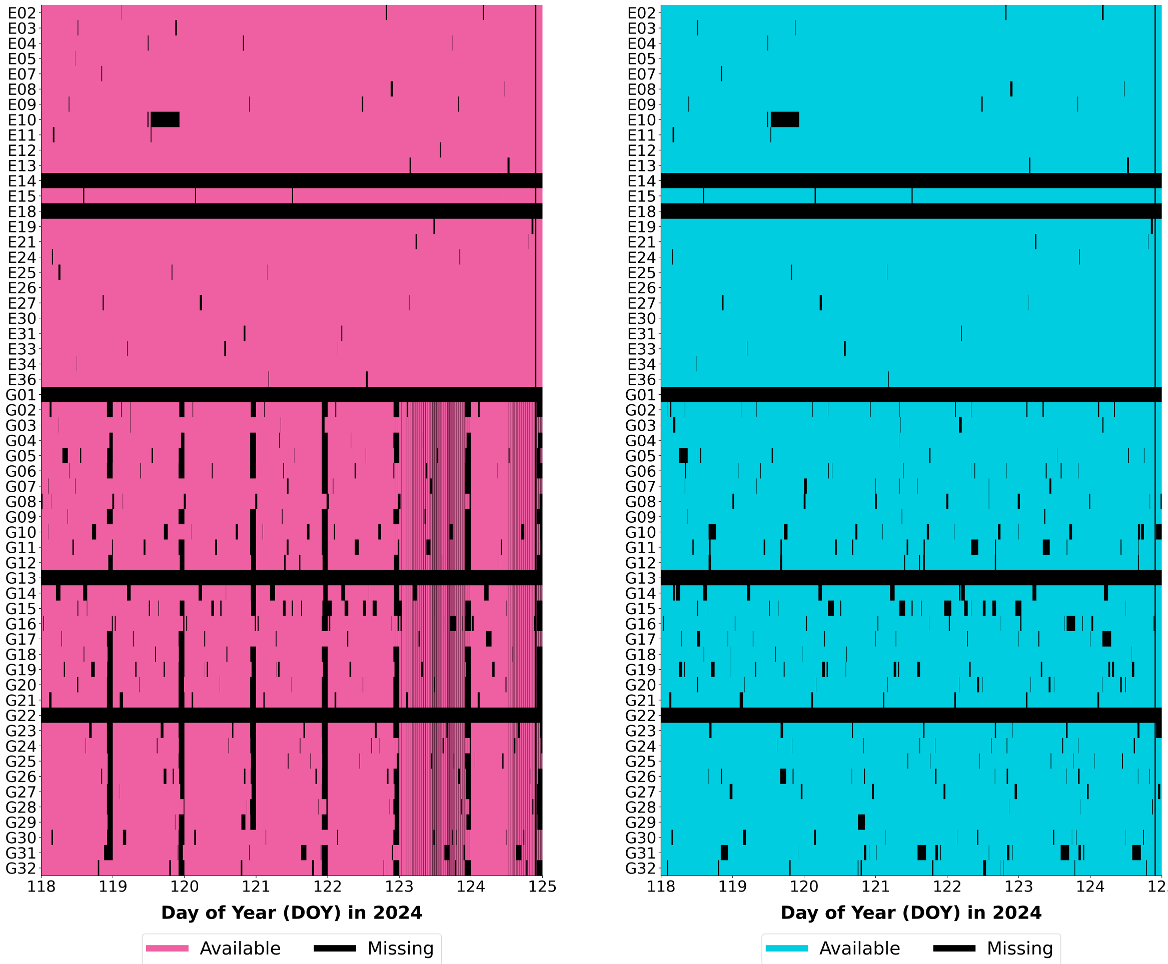

Figure 4.1: The **orbit** product availability per GPS (G) and Galileo (E) PRN for HAS Batch 1 (left) and Batch 2 (right). Batch 1 displays periodic data gaps at the end of each day and more frequent gaps on DOY 123 and 124 for most GPS satellites, which are not occurring in Batch 2. Both batches do experience other intermittent gaps, also primarily for GPS satellites.

Table 4.3: The average availability of the orbit and clock products for the Galileo (E) and GPS (G) constellations for the HAS and CRT from DOY 118 to 124 in 2024, excluding the unusable satellites E14, E18, and G01.

	Constellation	HAS Batch 1	HAS Batch 2	CRT
Orbit Availability [%]	E	99.1	99.2	91.3
	G	82.5	90.6	96.8
Clock Availability [%]	E	98.4	98.6	91.3
	G	82.6	88.5	96.8

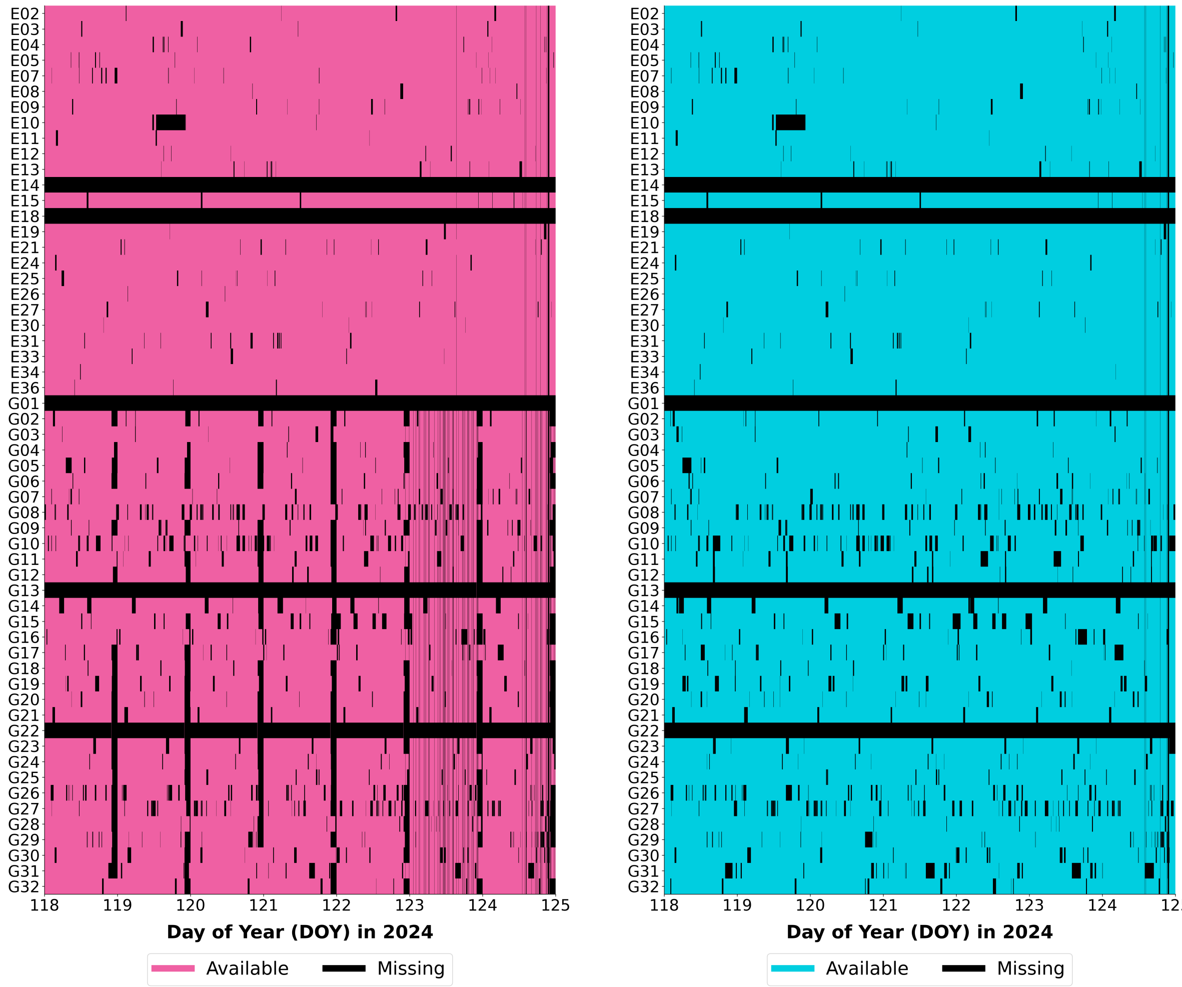

Figure 4.2: The **clock** product availability per GPS (G) and Galileo (E) PRN for HAS Batch 1 (left) and Batch 2 (right). Batch 1 displays periodic data gaps at the end of each day and more frequent gaps on DOY 123 and 124 for most GPS satellites, which are not occurring in Batch 2. Both batches do experience other intermittent gaps, also primarily for GPS satellites.

The higher sampling rate is notably the reason that the availability of Batch 1 is mentioned in this report, since the POD results did show a better performance in orbit accuracy for Batch 1 as compared to Batch 2, as shown in Figure 4.3 and Table 4.4. These POD results are presented here as an illustrative example, as the POD setup will be presented in Chapter 5.

The orbit errors for these POD results are calculated with respect to the precise Sentinel-6A reference orbits and are presented in the RTN satellite-coordinate system, which moves along with the satellite (Vallado, 2013, Chapter 3). RTN stands for Radial, Transverse, and Normal, and is also sometimes referred to as the Radial, Along-track, and Cross-track (RAC) directions, or with the letters RSW as presented in Vallado (2013, Chapter 3). The R-axis is in the direction from the Earth's center towards the satellite. The T-axis is perpendicular to R and is in the direction of the velocity vector, though it is not necessarily parallel to the velocity. The N-axis is perpendicular to both R and T, and is also normal to the orbital plane. The unit vectors for RTN directions relate to a satellite's position vector $\boldsymbol{r}$ and velocity vector $\boldsymbol{v}$ according to Equation 4.1 (Vallado, 2013, Chapter 3). The 3D error is taken as the Euclidean norm of the RTN components.

$$\boldsymbol{e}_R = \frac{\boldsymbol{r}}{||\boldsymbol{r}||} \quad \boldsymbol{e}_N = \frac{\boldsymbol{r} \times \boldsymbol{v}}{||\boldsymbol{r} \times \boldsymbol{v}||} \quad \boldsymbol{e}_T = \boldsymbol{e}_N \times \boldsymbol{e}_R \tag{4.1}$$

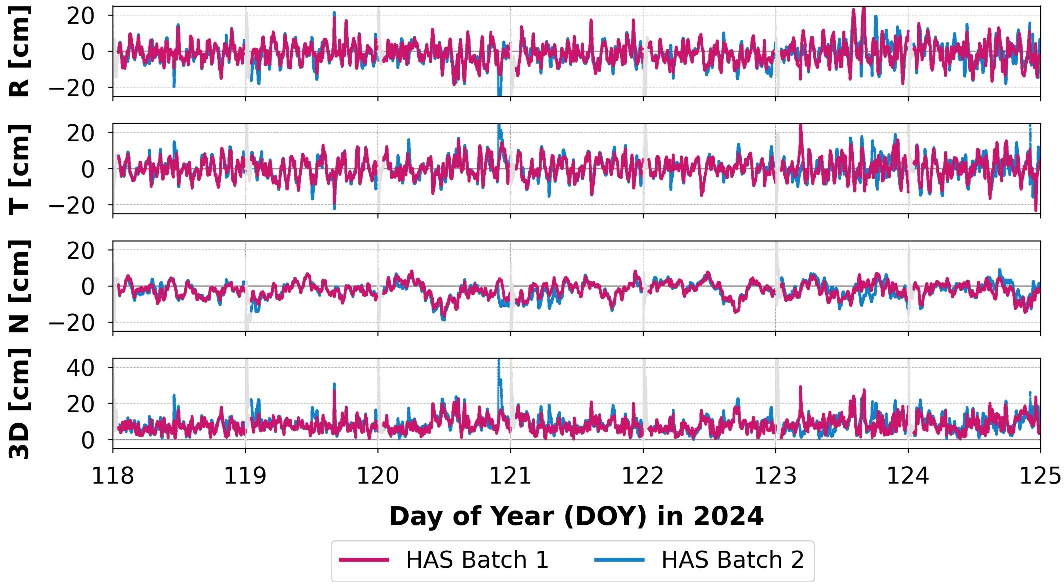

Figure 4.3: An illustrative example of the Sentinel-6A orbit errors using HAS Batch 1 and HAS Batch 2 products, where the exact POD setup will be presented in Chapter 5. The first hour of each day is grayed out, since this is not considered in the statistics to account for the initialization of the filter. The corresponding RMS values for each component are shown in Table 4.4.

Table 4.4: The RMS values for the Sentinel-6A orbit errors obtained from the POD using HAS Batch 1 and HAS Batch 2 over DOY 118-124 (2024), corresponding to Figure 4.3. The RMS of Batch 1 is lower than that of Batch 2, despite having the periodic data gaps shown in Figure 4.1 and Figure 4.2.

Batch	R [cm]	T [cm]	N [cm]	3D [cm]
HAS Batch 1	5.7	5.3	4.7	9.1
HAS Batch 2	6.1	5.9	5.0	9.9

These results show that the 3D RMS of Batch 1 was 9.1 cm, as compared to 9.9 cm for Batch 2, where the first hour of each day was excluded in these statistics to neglect the errors due the initialization of the filter. The improved POD accuracy of Batch 1 is suspected to be due to its higher sampling rate, even with the large GPS data gaps at the ends of the days, as the only difference in the POD configuration presented here is the use of HAS Batch 1 versus HAS Batch 2 products. This highlights the potential improvement in accuracy that can be offered by a higher product sampling rate. Despite this, the data gaps in Batch 1 were not found to be representative of realistic HAS conditions, leading to the choice of Batch 2 for the HAS data used in this study. **Therefore, the remainder of the report will refer to Batch 2 when considering HAS products.**

For CRT products, the PRNs E11, E14, E18, E19, G01, and G28 were missing entirely. As mentioned for the HAS data, satellites E14, E18, and G01 were designated as “unusable” during the considered data period. The rest of the satellites missing from the CRT products were flagged as healthy during this time. From consulting the online database of CRT products, it seems that this issue can come and go for these satellites, spanning several months at a time. Besides these missing satellites, there were no other data gaps present in the CRT orbit and clock products, meaning that the rest of the satellites had an availability of 100% of the time. Accounting for the missing healthy satellites while not including the unusable ones gives an average availability of 96.8% for GPS (G) and 91.3% for Galileo (E) for the CRT products over this period, as reported in Table 4.3. Between the two products, it can be noted that CRT has the higher availability for GPS, while HAS has the higher availability for Galileo.

4.2.2. CRT & HAS Accuracy

Following the availability analysis, the accuracies of the CRT and HAS products were analyzed by comparing the orbit and clock products to the precise CODE MGEX Final (COD) products. For the orbit errors, the `EphCmp` (Ephemeris Comparison) tool in GHOST was used to compare the SP3 files of the products. The resulting orbit errors for the HAS and CRT products over time, along with the distributions of these errors, are shown in Figure 4.4 and Figure 4.5 respectively. The distributions of the 3D orbit errors in particular are also displayed in Figure 4.6. For the RMS computations, outliers with values larger than 1.00 meter were filtered out for each component, which only resulted in the exclusion of 6 out of 46001 Galileo data points in the HAS orbit errors.

During the analysis, it was noted that the distribution of the radial component for the Galileo satellites in the CRT products in particular had a noticeable offset in the mean. It was chosen to de-bias this term for both constellations and both products to allow for a more realistic representation of this orbit error component, since a systematic bias found in all GNSS satellites would nonetheless be absorbed by the estimated receiver clock offset. For MEO GNSS, the radial component is also one of the main contributors to the Signal-In-Space Ranging Error (SISRE), which will be further defined below. The T and N components in turn contribute much less to the SISRE of MEO GNSS, meaning that any bias in these terms would not affect the receiver position estimate as much.

For the CRT products, the 3D RMS orbit errors in this study were found to be 6.6 cm and 9.5 cm for GPS and Galileo respectively. The 3D RMS orbit error for Galileo is around 3 cm larger than for GPS, which is consistent with Chen et al. (2024) who report 3D RMS orbit errors of 5.2 cm and 8.7 cm for GPS and Galileo respectively for DOY 220-226 in 2023. For the HAS products, the 3D RMS orbit errors in this study are similar for GPS and Galileo at 11.8 cm and 11.4 cm respectively. Furthermore, the HAS RTN RMS orbit errors shown in Figure 4.4 are quite consistent with the results presented in Zhou et al. (2024) for DOY 70-79 in 2023. They reported 3.7 cm, 10.6 cm, and 5.7 cm for the respective GPS RTN RMS orbit errors, and 3.2 cm, 9.4 cm, and 6.5 cm for those of Galileo. Lastly, it can be noted that the CRT orbit products have lower orbit errors than the HAS products.

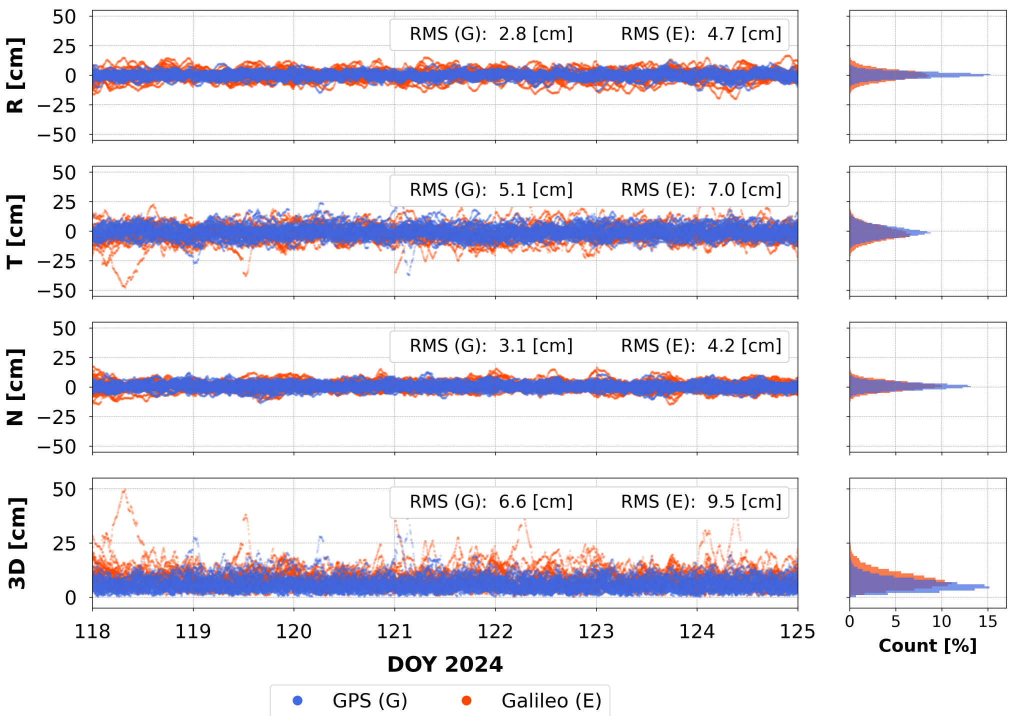

Figure 4.4: The **CRT** orbit product errors as compared to COD over the considered data period, where (only) the radial component has been de-biased. Bins of 1 cm have been used for the counts shown on the right. No outliers larger than 1.00 m were present.

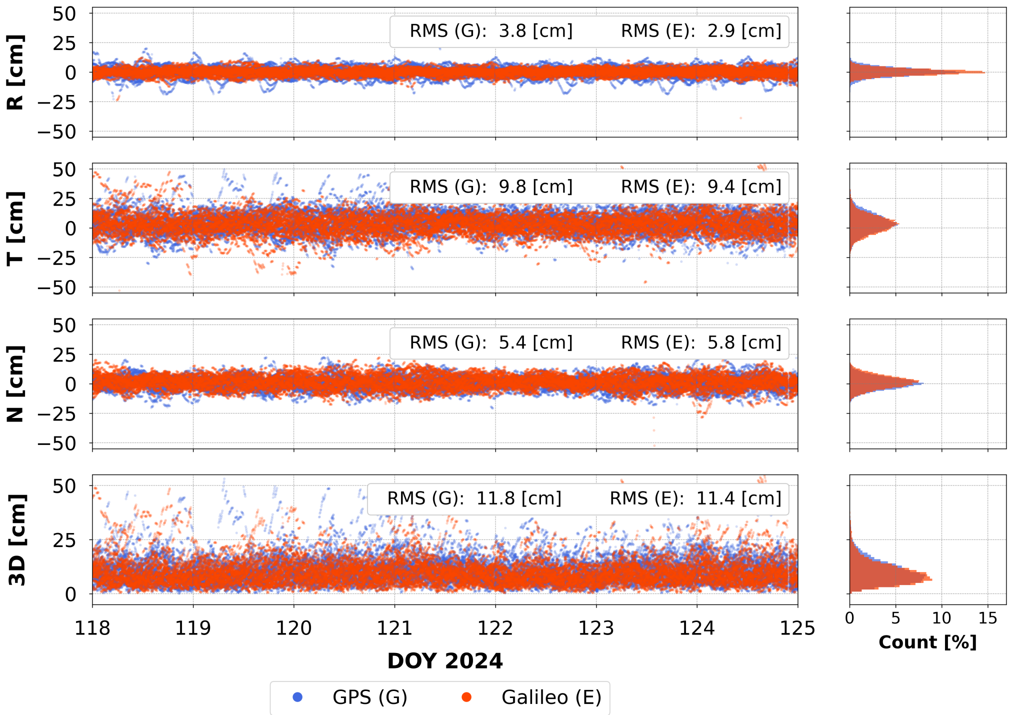

Figure 4.5: The **HAS** orbit product errors as compared to COD over the considered data period, where (only) the radial component has been de-biased. Bins of 1 cm have been used for the counts shown on the right. For Galileo, 6 outliers larger than 1.00 m out of 46001 data points were excluded, while no outliers were present for GPS.

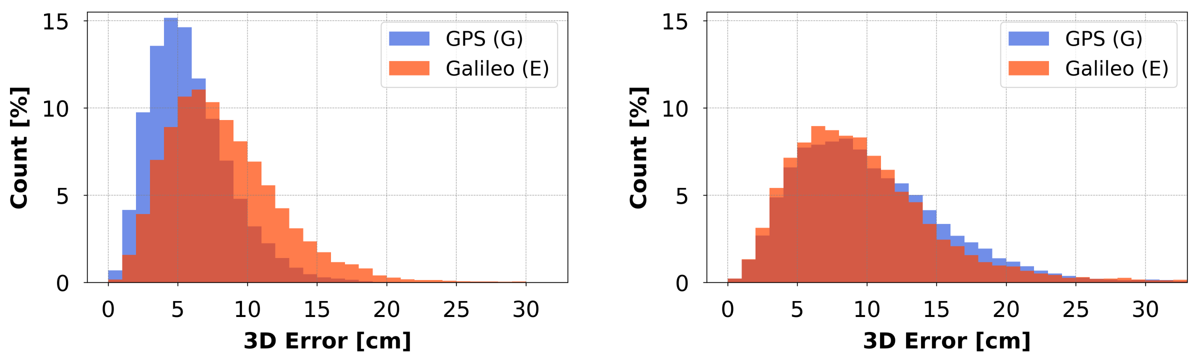

Figure 4.6: The distributions of the 3D orbit product errors of CRT (left) and HAS (right) as compared to COD over the considered data period, where bins of 1 cm have been used.

The clock errors for the HAS and CRT products were analyzed by comparing them to the COD products, where two operations were performed for a more realistic assessment. First, the constellation mean at each epoch was removed from the satellites in the corresponding constellation. This removes common variations that can be present among satellites within the same constellation, which can vary per analysis center due to differences in their product generation methods (Naciri et al., 2023). In practice, each satellite product is determined with respect to certain reference signals. Each choice of reference signal gives a corresponding bias, as explained in Section 3.2. When comparing two types of products, both products should be referenced to the same signals, which can be achieved by applying bias corrections if this was not already the case. In this work, the clock differences between the products were corrected by removing the 24-hour satellite mean from each individual satellite, based on the assumption that the bias correction for each satellite remains fairly stable over a day.

After removing the constellation mean per epoch and the 24-hour mean per satellite, these adjusted clock differences are shown for the CRT products in Figure 4.7 for the entire data period. The HAS (Batch 2) clock products, however, have extreme outliers before and after the midnight of DOY 119, as can be noted from Figure 4.8. As these outliers were of different magnitudes and durations for each satellite, the previously mentioned mean-removals were not effective for adjusting the clocks on DOY 118 and 119. Further analysis showed that HAS Batch 1 did not exhibit such clock outliers on these days at all, but only the gaps that were described in the previous section.

Figure 4.9 shows a comparison of the periods where HAS Batch 1 had clock gaps and the HAS Batch 2 had clock outliers. For GPS, it can be seen that these align quite well for most satellites, where there are a few satellites such as G23, G26, and G31 that do have a gap but not an outlier. For most of Galileo satellites, as well as G14 and G15, there are outliers in Batch 2 starting on DOY 119 without corresponding gaps (or outliers) in Batch 1. For these reasons, it is suspected that these HAS Batch 2 outliers have occurred due to an error in the generation of the product file itself, rather than an issue in the HAS corrections themselves. More typical behavior for the HAS clock errors, where such high outliers have not occurred, can be observed from DOY 120 to 124, as shown in Figure 4.10.

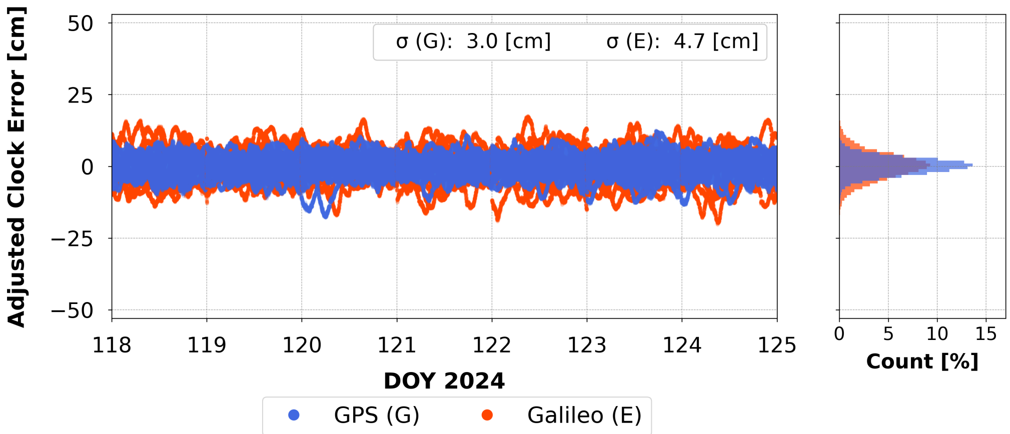

Figure 4.7: The adjusted CRT clock product errors as compared to COD over the considered data period, after removing the constellation mean per epoch and the 24-hour mean per satellite. Bins of 1 cm have been used for the counts shown on the right. No outliers larger than 1.00 m were present.

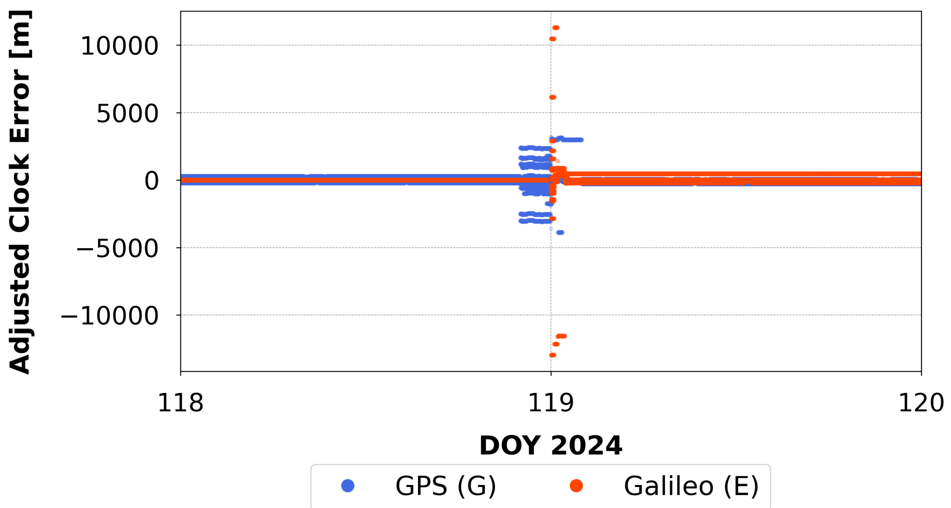

Figure 4.8: Outliers in the HAS clock products as compared to COD on DOY 118 and 119 (2024), after removing the constellation mean per epoch and the 24-hour mean per satellite. The outliers are suspected to be due to errors in the generation of the product file as further shown in Figure 4.9.

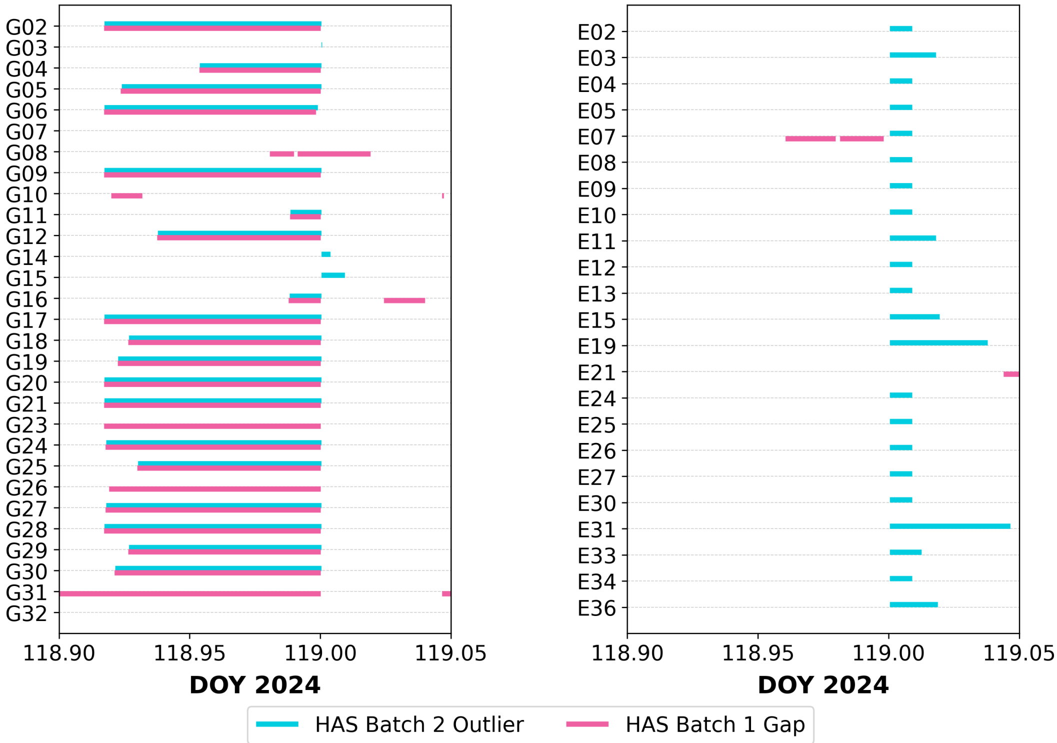

Figure 4.9: Comparison of the presence of **outliers** in the HAS Batch 2 clock products and **gaps** in the HAS Batch 1 clock products. For most GPS satellites, the Batch 2 outliers align almost exactly with the Batch 1 gaps. Batch 2 outliers after midnight on DOY 119, namely for G14, G15, and most of the Galileo satellites, occur while there are no gaps (or outliers) in Batch 1. This suggests that the discrepancies are likely not due to systematic issues with HAS but rather errors in the generation of the product files.

Similar to the orbit errors, GPS has lower CRT clock errors as compared to Galileo, with standard deviations of 3.0 cm and 4.7 cm respectively. For GPS, this value is similar to the 2.8 cm reported by Chen et al. (2024) for DOY 220-226 in 2023, while for Galileo it is around 1 cm higher than their value of 3.9 cm. The standard deviations of the nominal HAS clock errors here are 7.7 cm and 4.7 cm for GPS and Galileo respectively. These values are within 0.5 cm of the average HAS clock error standard deviations reported by Zhou et al. (2024) for DOY 70-79 in 2023, which were 7.2 cm and 5.4 cm for GPS and Galileo respectively. When comparing the CRT and HAS clock errors to each other, they are lower for GPS than Galileo in the CRT products and vice versa for HAS.

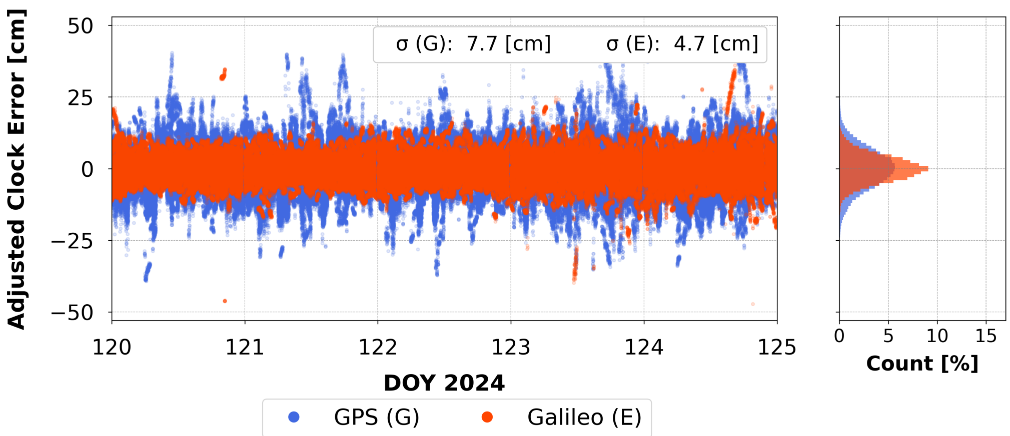

Figure 4.10: Nominal behavior for the adjusted HAS clock product errors as compared to COD over part of the data period, after removing the constellation mean per epoch and the 24-hour mean per satellite. Bins of 1 cm have been used for the counts shown on the right. Over this period, no outliers larger than 1.00 m were present.

The impact of the orbit and clock errors on user performance can be evaluated with the Signal-In-Space Range Error (SISRE) (Montenbruck et al., 2015). The contribution of the orbital error for a user at a specific location depends on the projection of this error onto the line-of-sight between the satellite and the user. When assessing the SISRE, a common approach is to consider a global average of points visible to a given satellite. This can be done with the following expressions (Montenbruck et al., 2015), where the SISRE(orb) considers only the orbit errors and the SISRE also includes the clock error:

$$\text{SISRE(orb)} = \sqrt{w_R^2 \Delta r_R^2 + w_{T,N}^2 \left(\Delta r_T^2 + \Delta r_N^2\right)} \tag{4.2}$$

$$\text{SISRE} = \sqrt{\left(w_R \Delta r_R - \Delta dt\right)^2 + w_{T,N}^2 \left(\Delta r_T^2 + \Delta r_N^2\right)} \tag{4.3}$$

As described in Montenbruck et al. (2018), these expressions can be used for computing the instantaneous SISRE, as well as the overall RMS of the SISRE. Here, Δr_R, Δr_T, and Δr_N are the orbit errors in the radial, transverse, and normal directions respectively. Δdt is the clock error, given here in units of length. The weights w_R and $w_{T,N}$ are constellation-specific and depend on the altitude of the satellites. The values for the GPS and Galileo weights used in this work were taken from Montenbruck et al. (2015) and are shown in Table 4.5. The values for each constellation differ slightly, as the weights are altitude-dependent and Galileo is around 3000 km higher in altitude than GPS.

Table 4.5: SISRE weights for GPS and Galileo, as obtained from Montenbruck et al. (2015).

System	w_R	$w_{T,N}$
GPS	0.98	$\sqrt{1/49}$
Galileo	0.98	$\sqrt{1/61}$

In this manner, the SISREs computed over time are shown in Figure 4.11 and Figure 4.12 for the CRT and HAS products respectively. It can be noted that due to the HAS clock error outliers on DOY 118 and 119, it was chosen to present the HAS SISREs from DOY 120 to 124. It can also be noted that values above 1.00 meter for any component were filtered out in this RMS computation, which only resulted in the exclusion of 3 outliers out of 32531 observations in the HAS data for the Galileo constellation and no exclusions from the GPS observations.

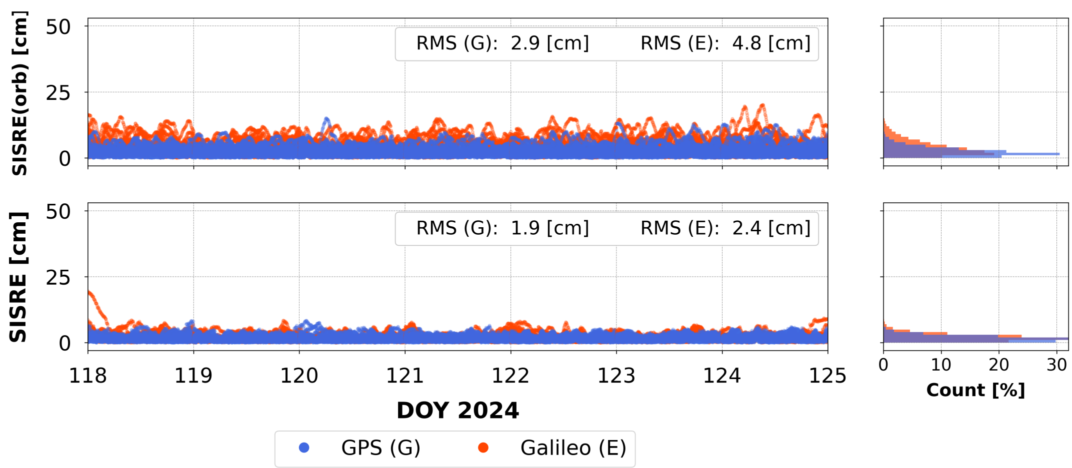

Figure 4.11: Signal-In-Space Ranging Errors (SISRE) for the CRT products for the considered data period, where bins of 1 cm have been used for the counts shown on the right. No outliers larger than 1.00 m were present.

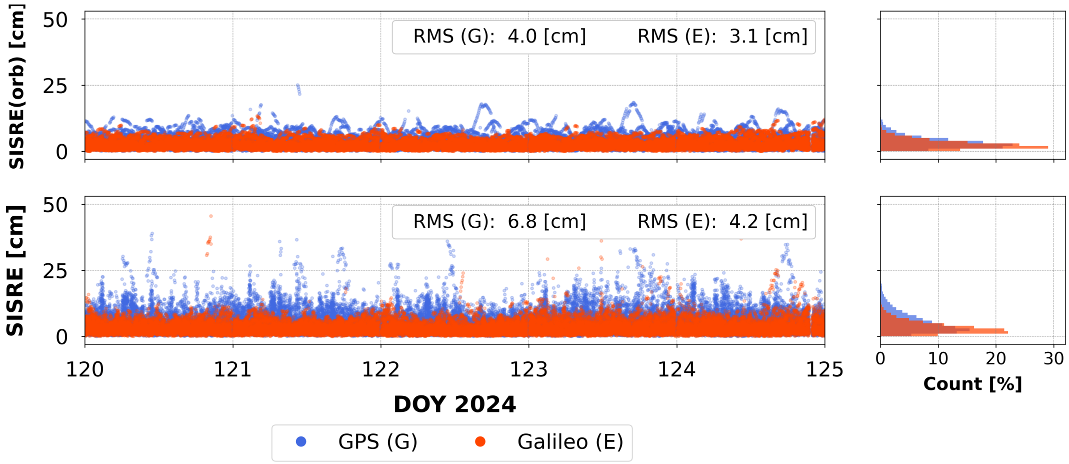

Figure 4.12: Signal-In-Space Ranging Errors (SISRE) for the HAS products over the part of the considered data period with nominal HAS clock errors, where bins of 1 cm have been used for the counts shown on the right. For Galileo, 3 outliers larger than 1.00 m out of 32531 data points were excluded, while no outliers were present for GPS.

For the CRT products, the SISRE RMS values were 1.9 cm for GPS and 2.4 cm for Galileo. These values are similar to the 1.6 cm and 2.3 cm SISRE RMS reported by Kazmierski et al. (2020) for GPS and Galileo respectively, where data from January 2017 to November 2019 was considered. Chen et al. (2024) report slightly higher SISRE RMS values of 2.6 cm and 3.9 cm for GPS and Galileo respectively for DOY 220-226 in 2023. Both of these references reported lower SISRE RMS errors as compared to the SISRE(orb), which is also observed here with SISRE(orb) RMS values of 2.9 cm and 4.8 cm for GPS and Galileo respectively. As mentioned by Montenbruck et al. (2015), a lower SISRE than SISRE(orb) can potentially occur due to correlations in the orbit and clock determination process.

For the HAS products, the SISRE(orb) RMS values were 4.0 cm for GPS,and 3.1 cm for Galileo. These SISRE(orb) RMS values are quite similar to the mean SISRE(orb) RMS reported by Mao et al. (2024), which were 4.2 cm and 3.0 cm for GPS and Galileo respectively for DOY 060-193 in 2023. Their SISRE RMS values of 13.7 cm (G) and 6.0 cm (E) were in turn larger than the 6.8 cm (G) and 4.2 cm (E) reported in here, especially for GPS. These differences can potentially be explained by comparing the SISRE RMS per satellite, as shown in Figure 4.13 and Figure 4.14 for the CRT and HAS products in this study respectively. In Mao et al. (2024), there are six GPS satellites with a SISRE RMS of larger than 20 cm and even one that is almost 40 cm, while here it does not reach over 10 cm for any satellite.

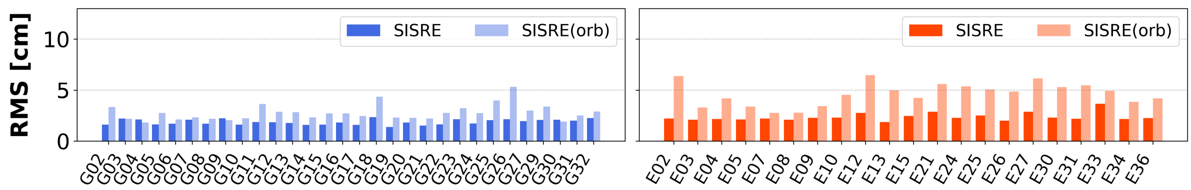

Figure 4.13: SISRE statistics per PRN for the **CRT** products over DOY 118 to 124. No outliers larger than 1.00 m were present.

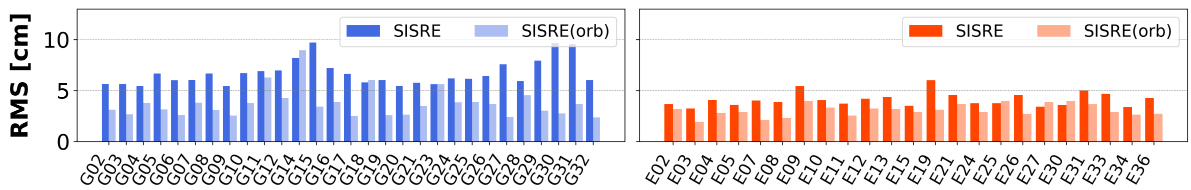

Figure 4.14: SISRE statistics per PRN for the **HAS** products over DOY 120 to 124, considering the part of the data period with nominal HAS clock errors. For Galileo, 3 outliers larger than 1.00 m out of 32531 data points were excluded, while no outliers were present for GPS.

5
POD Setup

Building up on the reduced-dynamic orbit determination method and GHOST tools introduced in Chapter 3, and the data that has been presented in Chapter 4, this chapter will cover the setup that was implemented for the POD study. First, Section 5.1 will present the reduced-dynamic Extended Kalman Filter (EKF) POD configuration that was used. Second, Section 5.2 will highlight the specific real-time considerations that have been taken in to account to better approximate what is possible when using on-board POD. Then, Section 5.3 will describe the filter settings that were tuned. Finally, Section 5.4 will briefly mention the strategy for estimating the clock errors.

5.1. General POD Configuration

As described in Section 3.1.3, the reduced dynamic orbit determination method was selected for this study. Accordingly, the `FAST` reduced-dynamic tool in GHOST (Wermuth et al., 2010) introduced in Section 3.1.4 was used for simulating on-board real-time GNSS-based POD, as it performs sequential estimation using an Extended Kalman Filter (EKF). The configuration of this reduced-dynamic EKF tool used in this study for the POD of Sentinel-6A (S6A) is introduced in this section.

The following signals are used to obtain the GNSS observations according to the default configuration of Sentinel-6A's receiver, as described in Section 4.1. The L1 P(Y) and L2 P(Y) are used for the legacy GPS satellites, L1 C/A and L2C are used for the modernized GPS satellites, and the E1 and E5a pilot signals are used for all Galileo satellites. In this POD setup, the dual-frequency Ionosphere-Free (IF) combinations of these signal pairs were used for the code and phase observations, which are shown in Table 5.1 with their corresponding RINEX identifiers (Romero, 2020). As discussed in Section 4.1, the S6A GNSS observations were obtained from the Copernicus Space Data Ecosystem (CDSE), where they are provided at a sampling rate of 10 seconds and in daily files.

The four GNSS product types introduced in Section 4.2 are used for the GNSS orbits and clocks, as summarized in Table 5.1. The igs20.atx antenna models were used for the transformation between the Antenna Phase Center (APC) and Center of Mass (COM) of the GNSS satellites for the COD, CRT, and HAS products. No GNSS antenna models were needed for the BRD products, since the broadcast ephemerides already refer to the APC. As mentioned in Section 3.1.4, the reference frame for the modeled observations is implied by the GNSS products that are used. For the precise products, this is the International Terrestrial Reference Frame ITRF2020. For the broadcast products, these are the terrestrial frame realizations corresponding to each constellation, namely WGS84 (GPS) and GTRF (Galileo). Following Montenbruck et al. (2022), the differences between the constellation frames and the ITRF are at cm-level and can be neglected here.

For Sentinel-6A, the primary GNSS POD antenna was used during the considered data period (DOY 118 to 124 in 2024), with its Antenna Reference Point (ARP) located at x = 2.475 m, y = 0.000 m, and z = −1.080m in the spacecraft's coordinate system (Cullen et al., 2021). An in-flight calibrated antenna pattern model for the Phase Center Offsets (PCO) and Phase Center Variations (PCV) similar to the one presented in Montenbruck et al. (2021) was used. The attitude information of S6A is obtained from quaternion data provided by the CDSE, which has included a yaw bias correction of -0.43°since September 23rd, 2023 (Calliess et al., 2024).

Table 5.1 lists the models for the gravitational and non-gravitational forces that were used for the satellite trajectory modeling as described in Section 3.1.4. The nominal setting for the degree and order of the gravity model used in the reduced-dynamic EKF was 45. For the S6A spacecraft parameters, the values for the mass and the center of mass were obtained from the International DORIS Service (IDS) online repository and are shown in Table 5.1. For the surface forces, the 8-panel macro model described in Montenbruck et al. (2021) was used.

As introduced in Section 3.1.4, the parameters that are estimated in the reduced-dynamic EKF at each epoch can be described as follows, where the selected estimation rate is every 10 seconds. First, there are the satellite position $\boldsymbol{r}$ and velocity $\boldsymbol{v}$ vectors in the inertial International Celestial Reference Frame (ICRF), which are propagated in the time-update step according to the described trajectory model. Second, there are the empirical accelerations in the RTN directions $\boldsymbol{a}_{\mathrm{emp}} = (a_R, a_T, a_N)$, which are predicted according to a Gauss-Markov process at the end of the time-update step. The remaining parameters are propagated as constant between the measurement epochs. These are the scaling factors for the aerodynamic drag C_D, solar radiation pressure C_R, and Earth radiation pressure C_E, the receiver clock offset dt_r with reference to the GPS constellation and an ISB parameter for Galileo, and the phase ambiguities A_r^s for each tracked GNSS satellite. The weights and constraints that were selected for the reduced-dynamic EKF POD setup are further discussed in Section 5.3. First, several real-time considerations relating to this POD setup are highlighted in the next section.

Table 5.1: An overview of the nominal models used in the reduced-dynamic EKF POD setup. The GNSS signal combinations are indicated with the corresponding RINEX identifiers (Romero, 2020), where "IF" stands for the Ionosphere-Free combination of two signals. The coordinates for Sentinel-6A are given in its satellite reference frame (Cullen et al., 2021).

Model	**Description**
GNSS observations	GPS Legacy: Code IF(C1W,C2W), Phase IF(L1C,L2W);
	GPS Modernized: Code IF(C1C,C2L), Phase IF(L1C,L2L);
	Galileo: Code IF(C1C,C5Q), Phase IF(L1C,L5Q);
	10-second sampling, daily arcs
GNSS orbits and clocks	CODE MGEX Final (COD): 5-minute orbits/30-second clocks;
	CNES Real-Time (CRT): 5-minute orbits/5-second clocks;
	Galileo HAS Signal-In-Space (HAS): 5-minute orbits/30-second clocks;
	Broadcast Ephemerides (BRD): LNAV (GPS) & INAV (Galileo)
GNSS transmitter antennas	igs20.atx for COD, CRT, HAS; None for BRD
S6A receiver antenna	Primary GNSS POD antenna at (+2.4748, +0.0001, −1.0803) (Cullen et al., 2021);
	In-flight calibrated PCO and PCV map (Montenbruck et al., 2021)
S6A attitude	From quaternions
Carrier phase wind-up	Modeled
Signal-to-Noise editing threshold	5.0 dB-Hz
Elevation editing threshold	0.0°
Spacecraft mass	1180.352 kg
Center of mass	(+1.53300, -0.00700, +0.03700)
Surface model	8-panel macro model (Montenbruck et al., 2021)
Earth gravity	GOCO03s (45×45) (Mayer-Gürr et al., 2012)
Third body gravity	Sun & Moon point-masses with analytical ephemeris (Montenbruck and Gill, 2000)
Solid Earth and pole tides	IERS2010 (Petit and Luzum, 2010)
Ocean tides	FES2004 (Lyard et al., 2006)
Solar radiation pressure	Conical Earth shadow
Earth radiation pressure	CERES Earth radiation data (Priestley et al., 2011)
Atmospheric drag	Jacchia 71 density model (Jacchia, 1971);
	NOAA/SWPC solar flux and geomagnetic activity data
Maneuvers	None during DOY 118-124 (2024)
Earth orientation parameters	CODE Final or Predicted

5.2. Real-Time and On-board Considerations

The previous section described the general POD implementation, along with the models that were available in the tool. As mentioned, a reduced-dynamic extended Kalman filter was used in this work for the on-board real-time POD. This section will cover several more real-time considerations that were implemented in the POD setup to better mimic what would be achievable on board a satellite.

- **Forward-only Kalman filtering:** In addition to a forward filter, the EKF can allow for the use of a backwards filter that runs in the reverse direction in time, allowing to “smooth” the estimation results. This would help to reduce the initialization effect of the filter. In real-time, however, it would only be possible to use data from the past. Thus, the forward-only filter setting was selected.

- **Model degradations:** Among the models presented in Table 5.1, the ones highlighted in Table 5.2 could on the one hand be implemented “as best as possible” with the given tool and software. Using these would represent the best achievable results given the available tools, which could be used to validate the POD setup through comparison with other state-of-the-art Sentinel-6A POD results. It can be noted that this validation is presented in the discussion of the POD results given in Chapter 6. On the other hand, these models could be “degraded”, which corresponds to implementing a less accurate model or omitting it entirely. This can be done for the sake of reducing computational complexity, while still potentially achieving sufficiently accurate results. This can be preferable in the case of limited on-board computational capabilities and/or the desire to reduce the latency of the POD computation.

  Accordingly, the possible degradations that could be configured in this study are shown in Table 5.2 and can be described as follows. The surface model degradation consists of using a simplified cannonball model instead of the more realistic 8-panel macro model for the surface force modeling. If no surface forces are modeled, such as in the case of no drag, SRP, and ERP modeling, then the satellite surface model is also not needed. For the EOPs, their final value would not be available in real time. Here, the predicted EOPs provided by CODE can be used instead, though in practice these would need to be uploaded to the satellites. Similar to the EOPs, the solar flux and geomagnetic activity would also not be available in real time, though these are not needed if the drag is also not modeled. Next, the accuracy of the Earth gravity model is dictated by the degree and order of spherical harmonics included in the gravity potential model, where higher degree and order values correspond to a higher accuracy. Lastly, the tide models shown in Table 5.1 can also be excluded.

  The impact of each possible degradation was checked individually by degrading each one at a time in the POD setup and performing the POD for the considered data period of DOY 118 to 124 in 2024. The gravity model degradation was checked by degrading the degree and order of the model in steps of 5, and was checked both individually, as well as in combination with all other degradations activated. The results of these checks are shown in Figure 5.1 by means of the 3D RMS orbit errors of the S6A POD conducted with the each of the described degradations, as compared to the precise S6A reference orbits provided by the Copernicus Space Data Ecosystem (CDSE). The numerical values corresponding to these results are given in Table 5.3.

  For all products, no significant reduction in accuracy was found when using a gravity model with a degree and order of around 35 and up. It can be seen that a small increase in error occurs at degree and order 25, while from 20 and lower this is increasing quite rapidly. Besides this, only the omission of the tide modeling had a more noticeable impact on the accuracy than the other individual degradations. This is in line with the expectations based on the magnitudes of the perturbing accelerations given in Montenbruck and Gill (2000, Chapter 3), which show a larger acceleration from the tides as compared to that of the drag, SRP, and ERP at the altitude of Sentinel-6A. Based on these findings, the final selected configuration consists of degree and order 25 for the gravity model and maintaining the tide modeling, while all other effects were set to the degraded setting. The 3D RMS orbit errors corresponding to this choice are highlighted at the bottom of Table 5.3. These are within 1 cm of the non-degraded case for the COD, CRT, and HAS products, while for the BRD products it is around 2 cm higher. Although absolute computation times depend on the processor used, the degraded settings provided approximately a 33% reduction in computation time on the platform used in this study. It is also worth noting that the EKF tool that was used has not been optimized for real-time processing.

- **Input reference orbit:** As mentioned in Section 4.1, a reference orbit is used in the FAST reduced-dynamic EKF tool for data pre-editing purposes. A coarse navigation solution would be representative of what could be available for this on-board. The SPPLEO tool in GHOST, which is a kinematic least squares estimator using only pseudorange measurements, could provide such a coarse reference orbit. However, to limit the number of steps in this POD simulation, it was checked whether the precise reference orbits for Sentinel-6A could be used for this instead, without artificially improving the POD accuracy due to an improved reference orbit.

  One of the data pre-editing steps in FAST checks the difference between the observed and modeled carrier phases, where the reference orbit is used to calculate the modeled measurement. It was found that a stringent setting for this difference (less than 2.0) results in the rejection of many more observations when using the less accurate reference orbit from SPPLEO, leading to a worse POD solution. By making this setting less stringent (more than 2.0), it was found that the POD results using either of the reference orbits were equal to the mm-level. Therefore, it was determined that the precise Sentinel-6A orbits could be used as input reference orbits to FAST without comprising the real-time and on-board characteristics.

Table 5.2: The possible degradations that can be implemented in the reduced-dynamic EKF POD setup to better reflect real-time characteristics, including the final selected settings corresponding to the results presented in Chapter 6.

Setting	Non-degraded	Degraded	Selection
Surface model	Macro model (8 panels)	Cannonball (1 sphere with surface area of 1 m^2)	**Degraded**
EOPs	Final	Predicted	**Degraded**
Drag modeling	ON	OFF	**Degraded**
SRP modeling	ON	OFF	**Degraded**
ERP modeling	ON	OFF	**Degraded**
Tide modeling	ON	OFF	**Non-degraded**
Gravity degree & order	> 35	< 35	**Degraded (25)**

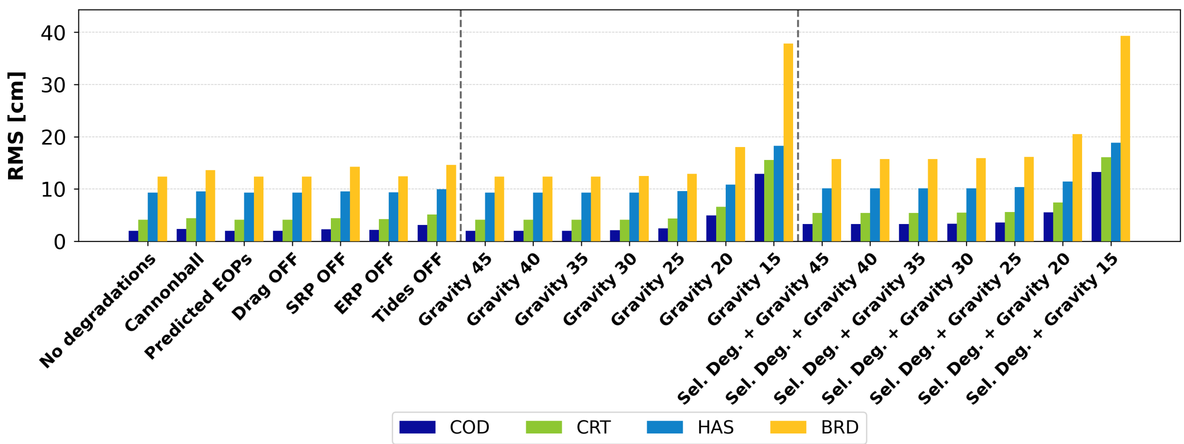

Figure 5.1: The 3D RMS orbit errors for the Sentinel-6A POD conducted with the various degradation configurations of the reduced-dynamic EKF POD setup, shown for the various GNSS products. The first option in the group on the left corresponds to no degradations at all. The rest of the group on the left represent the cases where each individual degradation mentioned is the only one that is degraded at a time. For the center group, the only setting that is degraded is the degree and order of the gravity model, while the rest of the settings are not degraded. On the right, “**All**” indicates that all of the individual degradations from the left group are enabled, in combination with the mentioned gravity model degree and order.

Table 5.3: The 3D RMS orbit errors in cm for each of the degradation configurations for the Sentinel-6A POD using a reduced-dynamic EKF, corresponding to the descriptions given in Figure 5.1. The final selected configuration is shown at the bottom and highlighted in green. It includes all individual degradations (predicted EOPs, drag OFF, SRP OFF, ERP OFF) **except for** the tides which remain ON, along with a gravity model degree and order of 25.

Degradations	COD	CRT	HAS	BRD
No degradations	2.0	4.1	9.3	12.4
Cannonball	2.3	4.4	9.6	13.6
Predicted EOP	2.0	4.1	9.3	12.4
Drag OFF	2.0	4.1	9.3	12.4
SRP OFF	2.3	4.4	9.6	14.2
ERP OFF	2.2	4.2	9.4	12.4
Tides OFF	3.1	5.1	10.0	14.6
Gravity 45x45	2.0	4.1	9.3	12.4
Gravity 40x40	2.0	4.1	9.3	12.4
Gravity 35x35	2.0	4.1	9.3	12.4
Gravity 30x30	2.1	4.1	9.3	12.5
Gravity 25x25	2.5	4.4	9.6	12.9
Gravity 20x20	4.9	6.6	10.8	18.0
Gravity 15x15	12.9	15.6	18.3	37.8
All + Gravity 45x45	3.3	5.4	10.1	15.7
All + Gravity 40x40	3.3	5.4	10.1	15.7
All + Gravity 35x35	3.3	5.4	10.1	15.8
All + Gravity 30x30	3.4	5.5	10.1	15.9
All + Gravity 25x25	3.6	5.6	10.4	16.1
All + Gravity 20x20	5.5	7.4	11.4	20.5
All + Gravity 15x15	13.3	16.1	18.9	39.3
Final selected degradations	2.8	4.7	9.9	14.5

5.3. Tuning of Settings

This section will describe the settings of the reduced-dynamic EKF that were tuned to improve the filter performance for the case of Sentinel-6A with respect to the precise reference orbits provided by the Copernicus Space Data Ecosystem (CDSE). The standard deviations of the pseudorange and carrier phase measurement noise, which are used for the observation weighting within the filter, are shown in Table 5.4. All of the constraints relating to the parameters estimated in FAST using the setup described in Section 5.1 are presented in Table 5.5. This setup originates from one that was provided by researchers at DLR that is similar to the one used in Montenbruck et al. (2021), though it can be noted that the exact constraints that they are using for their real-time POD setup for Sentinel-6A specifically are not reported in literature.

The settings that were further tuned are the measurement standard deviations, and the constraints for the empirical accelerations and the phase ambiguities. This tuning was done with a parametric search and was guided by conventions found in the literature (Hauschild and Montenbruck, 2021), (Montenbruck et al., 2022), (Hauschild et al., 2022). For the measurement weights, a small search showed that the standard deviations of 1.0 m and 1 mm for the pseudorange and carrier phase measurements respectively were an optimal choice. Similarly, for the process noise of the empirical accelerations, steady-state standard deviations of 5.0, 5.0, and 10.0 nm/s^2 for the R, T, N directions respectively at a correlation interval of 600 seconds were found to give the best orbit accuracy as compared to the precise reference orbits. It can be noted that for simplicity it was chosen to obtain a single set of process noise settings for the empirical accelerations that would be suitable for all four of the GNSS product types considered in this study.

The phase ambiguities have been found to partly absorb slow-varying ephemeris errors when these ambiguities are estimated as random-walk parameters by adding white process noise in the time-update step (Montenbruck et al., 2022). This is most beneficial for the broadcast products, which exhibit the largest ephemeris errors out of the products considered in this study. Accordingly, phase ambiguity process noise standard deviations of 20 mm and 7 mm were selected for GPS and Galileo respectively for the BRD products, which were also used by Hauschild et al. (2022). Furthermore, through the parametric search it was found that a small amount of process noise for the phase ambiguities also improved the accuracy of the POD using the CRT and HAS products, leading to the selection of 1 mm for their phase ambiguity process noise standard deviations for both GPS and Galileo. For the highly-accurate COD products, adding process noise only deteriorated the POD accuracy, so the process noise standard deviation of the phase ambiguities was set to 0 in this case.

Furthermore, the time interval for the application of process noise to the ambiguities could also be selected. During the parametric search, it was found that for the more accurate products, a larger interval was more beneficial, as their errors are more slow-varying in time. The less accurate products, which may experience more variability in their ephemeris errors, instead benefited from somewhat shorter intervals, such as the 60 seconds used by Hauschild et al. (2022). For simplicity, it was preferred to select one value that gave a balanced performance for each of the products. Therefore, an interval of 300 seconds was selected for the CRT, HAS, and BRD products. Since there was no process noise added for COD, the time interval for these products was also set to 0. Lastly, the a-priori standard deviation of the phase ambiguities for all four products was set to 10 m, where this value was selected to avoid over-constraining the filter at the start of each interval. This concludes the explanation of the reduced-dynamic EKF POD setup, where the results using this setup are presented in the next chapter. Before presenting the POD results, the generation of the reference clock solutions using a reduced-dynamic Batch Least Squares (BLS) estimator is described in the last section of this chapter.

Table 5.4: The standard deviations of the pseudorange and carrier phase measurement noises for both GPS (G) and Galileo (E) observations. These are used for the observation weighting in the reduced-dynamic EKF as described in Section 3.1, and are adopted for each of the four types of GNSS products considered in this study.

Pseudorange	σ_{PR}	1.0 m
Carrier phase	σ_{CP}	1 mm

Table 5.5: The selected reduced-dynamic EKF constraints for each of the estimated parameters, which are used to set up the parameter covariance matrix as described in Section 3.1. Each parameter has an associated a-priori standard deviation. Process noise is added to the empirical accelerations according to a Gauss-Markov process, and to the receiver clock offset and the phase ambiguities according to a random walk process, where the corresponding steady-state standard deviations and time intervals are shown here. Each constraint is valid for "All" four of the GNSS products considered in this study, **except for** the phase ambiguity constraints, which are specified for each product individually. It can be noted that the FAST EKF tool did not have the option to set the constraint for the ISB parameter.

Type	Paremeter	GNSS Product	A-priori σ	Steady-state σ	τ
Position	$\boldsymbol{r}$	All	100 m	–	–
Velocity	$\boldsymbol{v}$	All	100 m	–	–
Scale factors	C_D	All	0.0001	–	–
	C_R	All	0.0001	–	–
	C_E	All	0.0001	–	–
Empirical accelerations	a_R	All	10 nm/s^2	5 nm/s^2	600 s
	a_T	All	10 nm/s^2	5 nm/s^2	600 s
	a_N	All	10 nm/s^2	10 nm/s^2	600 s
Receiver clock offset	dt_r	All	500 m	500 m	600 s
Phase ambiguities	A_r^s	COD	10 m	0 mm	0 s
		CRT	10 m	1 mm	300 s
		HAS	10 m	1 mm	300 s
		BRD	10 m	G: 20 mm; E: 7 mm	300 s

5.4. Reference Clock Estimation

As mentioned, the receiver clock offset is also one of the parameters that is determined in the POD. Similar to GNSS, the clock errors for the LEO-PNT satellites are also an important factor in the overall accuracy that is ultimately achievable for their users. As highlighted in Section 2.2.4 and Section 3.1.5, LEO-PNT users would need the LEO satellite *transmitter* clock offset, while it is the LEO satellite *receiver* clock offset that is estimated in the on-board POD. These clock offsets would differ in their respective hardware biases, and it could also be the case that different signals would be transmitted by the LEO-PNT satellites as compared to the MEO GNSS signals used in the LEO on-board POD. While these differences could be calibrated to a certain degree prior to launch, high-precision applications would likely require in-orbit estimation of these biases (Liu et al., 2024), which can only be done by receiving the LEO-PNT signals in the case of the transmitter biases. Despite these bias differences, the estimated receiver clock obtained from the Sentinel-6A POD can give an indication of the (receiver) clock errors that can be achieved using on-board real-time POD.

The DORIS Ultra-Stable Oscillator (USO) is the frequency reference for the PODRIX receiver on Sentinel-6A (Montenbruck et al., 2021). As opposed to the orbit errors, there is no S6A reference clock data that is made publicly available. Therefore, an alternative strategy to characterize the clock errors had to be devised for this study. In this case, a reduced-dynamic Batch Least-Squares (BLS) estimation tool was used to obtain a precise clock estimate that could be used as the reference clock solution. The BLS POD method used in the `RDOD` tool in GHOST was presented in Section 3.1, using the same models presented in Section 5.1. As opposed to the EKF POD setup, a gravity model degree and order of 70 and no other degradations were used in the BLS POD. Although, it can be noted that including the selected degradations did not make a noticeable difference in the receiver clock offsets estimated with BLS. Furthermore, only the COD GNSS products were used in the BLS POD as these are the most accurate ones considered in this study. The measurement noise standard deviations used in the BLS POD setup are the same as the ones given in Table 5.4. In the BLS POD, the estimated parameters are the initial position $\boldsymbol{r}_0$ and initial velocity $\boldsymbol{v}_0$, along with a single of each scaling factor C_D, C_R, and C_E for the entire arc. The empirical accelerations are independently estimated as piecewise constant over intervals of 600 seconds. The receiver clock offset referenced to GPS and the Galileo ISB parameter are estimated at each measurement epoch, which is also every 10 seconds. Lastly, the phase ambiguities are estimated for each continuous pass of a tracked GNSS satellite. The a-priori parameter standard deviations used in the BLS POD setup are presented in Table 5.6.

Table 5.6: The a-priori standard deviations for each of the parameters estimated in the BLS POD, which are used to set up the a-priori parameter covariance matrix as described in Section 3.1. It can be noted that the receiver clock offset dt_r and the ISB are not constrained in the `RDOD` BLS POD tool. The estimation interval τ for the empirical accelerations is 600 seconds.

Type	Paremeter	A-priori σ
Initial position	$\boldsymbol{r}_0$	100 m
Initial velocity	$\boldsymbol{v}_0$	100 m
Scale factors	C_D	0.0001
	C_R	0.0001
	C_E	0.0001
Empirical accelerations	a_R	4 nm/s^2
	a_T	8 nm/s^2
	a_N	15 nm/s^2
Phase ambiguities	A_r^s	10 m

The Sentinel-6A BLS POD results can briefly be described as follows. The orbit errors as compared to the precise reference orbits from the CDSE are presented in Figure 5.2. A 3D RMS orbit error of 1.8 cm is obtained over the considered data period of DOY 118 to 124 in 2024. The work of Montenbruck et al. (2021) uses a similar reduced-dynamic batch POD setup. Though they do not directly report the orbit errors of their solution using COD products as compared to another POD reference orbit, they do report a 3D RMS of 1 cm as compared to Satellite Laser Ranging (SLR) residuals. In contrast to this thesis, they are using ambiguity fixing in their POD, which can explain the slightly larger orbit errors obtained here. Chen et al. (2024) also report orbit errors for Sentinel-6A POD using a reduced-dynamic BLS approach, obtaining a 3D RMS of 2.9 cm when using COD products. As compared to these results from literature, the orbit errors obtained with reduced-dynamic BLS here are in line with the expectations.

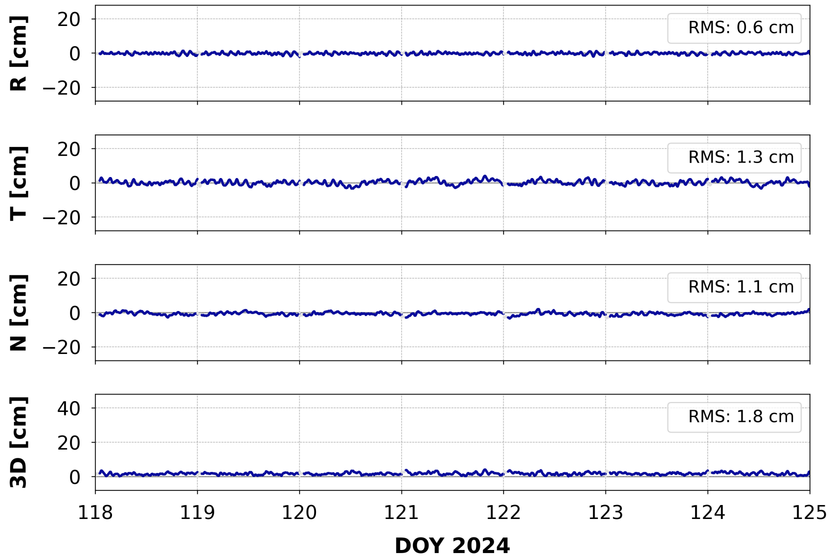

Figure 5.2: The Sentinel-6A orbit errors from using reduced-dynamic BLS with the COD GNSS products. The orbit errors are computed with respect to the precise S6A reference orbits provided by the Copernicus Space Data Ecosystem (CDSE). The RMS statistics are computed excluding the first hour of each day for consistency with the results presented in Section 6.1.

As mentioned, the purpose of using the BLS estimator in this work is to obtain reference clock offset values that can be used to assess the real-time S6A clock errors. Figure 5.3 shows the estimated receiver clock offset referenced to GPS time and the estimated ISB for Galileo for the example DOY 124 in 2024. The patterns and orders of magnitude of these curves are consistent with the S6A clock offset and ISB estimates presented by Montenbruck et al. (2021), Peter et al. (2022b), and Conrad et al. (2024), which have all also employed reduced-dynamic POD. This includes the parabolic shapes of the clock offset, which show local peaks that are attributed by Montenbruck et al. (2021) to passages of the South Atlantic Anomaly (SAA), where increased ionizing radiation levels affect the oscillator frequency. The frequent jumps in the ISB estimate were also noted in each of the references, which are attributed to phase jumps in the oscillators used for down-conversion in the front-end of the receiver (Montenbruck et al., 2021). These similarities with literature indicate that this is a suitable reference clock estimation method for the nature of this work.

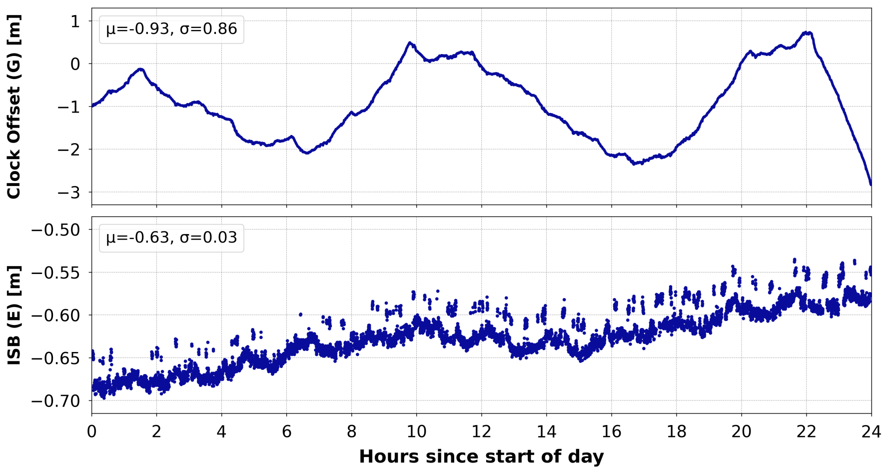

Figure 5.3: The Sentinel-6A estimated receiver clock offset with reference to GPS (G) and the estimated Galileo (E) ISB parameter determined using reduced-dynamic BLS, shown for a representative DOY 124 in 2024.

Ultimately, the clock error strategy outlined in this section is effectively only a comparison of processing methods (and GNSS products) using the same data as opposed to an independently obtained reference. However, it can provide a view on the different clock accuracies that are achievable using the various GNSS product options in real-time as opposed to post-processing. It can also be noted that a similar approach of comparing BLS and EKF POD solutions for Sentinel-6A was used by Kunzi and Montenbruck (2022) for their characterization of on-board precise time synchronization of LEO satellites. As such, the reference clock estimation method using reduced-dynamic BLS described here, along with the precise S6A reference orbits provided by the CDSE were used to assess to the reduced-dynamic EKF POD orbit and clock errors, which is described in the next chapter.

6 POD Results

This chapter presents the main results that have been obtained for the rela-time POD of Sentinel-6A (S6A), using the setup described in Chapter 5. This POD procedure has been conducted using each of the GNSS product types described in Chapter 4, namely COD, CRT, HAS, and BRD products. The presented POD results consist of the orbit errors in Section 6.1, the clock errors in Section 6.2, and the Signal-In-Space Range Error (SISRE) results in Section 6.3.

6.1. Orbit Errors

In this section, the time series' of the estimated Sentinel-6A orbit errors from the POD using each of the considered GNSS products are presented in Figure 6.1. It can be noted that these POD solutions have been computed using both GPS (G) and Galileo (E), as this study assumes that the LEO-PNT satellites would be equipped with a multi-constellation receiver. The orbit errors are computed as the difference between the orbit solutions from `FAST` and the precise Sentinel-6A reference orbits described in Chapter 4. Each figure shows the orbit errors in the R, T, and N directions, which follow the same definitions given in Section 4.2.2, along with the total (3D) orbit error which is taken as the Euclidean norm of the vector of the RTN components. It can be noted that the first hour of each day has been neglected to account for the initialization period of the filter, as the results were processed by individual days in arcs of 24 hours using only forward filtering. As expected, the results vary from best to worst according to the quality of the GNSS products employed, with 3D RMS orbit errors of 2.8 cm, 4.8 cm, 9.9 cm, and 14.5 cm for the real-time POD using COD, CRT, HAS, and BRD products respectively. The POD results using HAS products did not suffer from the HAS clock product outliers on DOY 118 and 119 presented in Section 4.2.2, since the corresponding GNSS observations were filtered out during the data pre-editing step.

The study of Darugna et al. (2022) also performs S6A POD using a reduced-dynamic EKF implementation and with GNSS products of varying quality, namely the CNES-CLS final products (G+E) which are comparable to the COD products here, the IGC real-time products (G only) which are comparable to the CRT products here, and the broadcast ephemerides (G+E). Though the exact setup is slightly different in terms of the exact models that are employed, as well as the selected values of the weights and constraints, the overall POD methodology is quite similar to the one adopted in this thesis. Comparing their precise CNES-CLS product results to the COD results in this work, their 3.8 cm 3D RMS is quite close to the 2.8 cm for COD reported here. This slight improvement is interesting to note, since the setup in this thesis is degraded, as opposed to Darugna et al. (2022) which has included drag and SRP modeling with a cannonball surface, along with an order and degree of 50 for the gravity model.

Another difference is the choice of pseudorange standard deviation (σ_{PR}) values, where 0.25-0.5 m were used in Darugna et al. (2022), as opposed to 1.0 m used here. During the setting tuning described in Section 5.3, it was found that a pseudorange standard deviation of 1.0 m instead of 0.5 m enabled improvements of about 1.0 cm in the 3D RMS for COD and CRT, which is in line with the previously mentioned COD 3D RMS difference between the works. For the real-time IGC product results in Darugna et al. (2022), only single-constellation results using GPS were reported. These had a 3D RMS of 6.8 cm (G-only) as opposed to the 4.8 cm (G+E) when using CRT products reported here. This improvement can be attributed to the use of two constellations, in addition to the choice in pseudorange standard deviation just discussed. Furthermore, Darugna et al. (2022) also uses a similar POD setup with the same CNES real-time SSR corrections. They achieve a 3D RMS of 5.8 cm using CRT products, though it can be noted that the exact constraints and weights are not reported in that work.

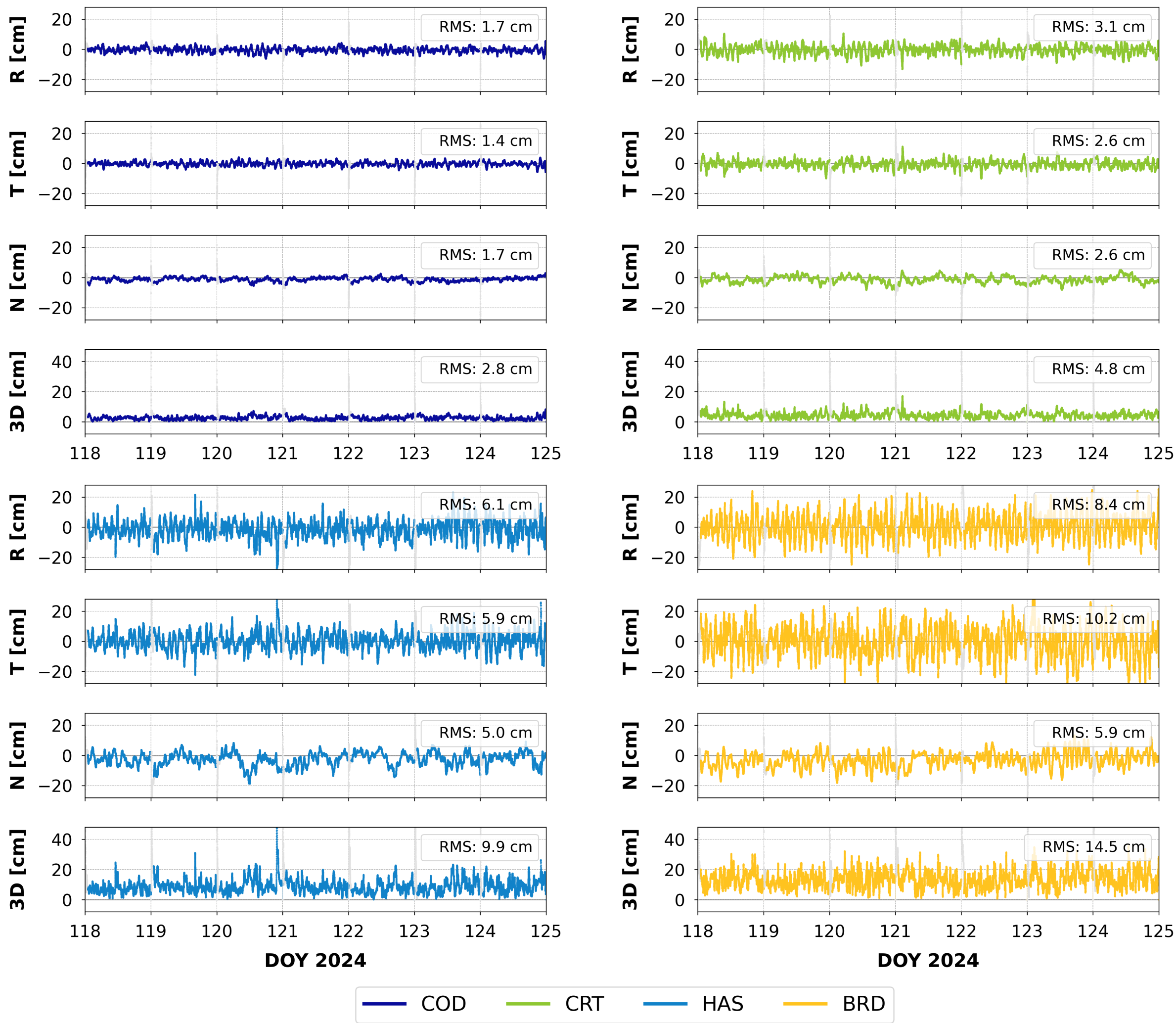

Figure 6.1: The Sentinel-6A orbit errors obtained using the reduced-dynamic EKF POD approach with the various types of GNSS products. The POD setup is the final selected degraded configuration presented in Section 5.2 using GPS+Galileo. The orbit errors are computed with respect to the precise S6A reference orbits provided by the Copernicus Space Data Ecosystem (CDSE). The RMS statistics are computed excluding the first hour of each day to account for the filter initialization.

For the real-time POD using BRD products, it can be noted that the results presented here exhibit larger orbit errors than those of Montenbruck et al. (2022), Darugna et al. (2022), Darugna et al. (2022), namely at 14.5 cm 3D RMS for the former as compared to 9.2 cm, 10.0 cm, and 11.0 cm respectively for the latter three in the GPS+Galileo case. However, as mentioned, the results presented here are obtained with degraded modeling settings as opposed to those from the reference studies. BRD orbit errors similar to Montenbruck et al. (2022) can be achieved by using the non-degraded settings for this setup and applying a dedicated tuning of the empirical accelerations, resulting in tighter constraints of 1.0 nm/s^2, 1.0 nm/s^2, and 5.0 nm/s^2 for the respective RTN empirical accelerations.

In this way, the following RMS orbit errors could be obtained using the BRD products: 3.2 cm, 7.8 cm, 3.4 cm, and 9.1 cm for R, T, N, and 3D RMS respectively. These results are consistent with the respective RMS orbit errors of 3-4 cm, 6–8 cm, 3-4 cm, and 9-10 cm reported by Montenbruck et al. (2022). Using the same non-degraded and constrained setup with the HAS products allows to achieve errors of 3.2 cm, 5.2 cm, 3.3 cm, and 6.9 cm for the R, T, N, and 3D RMS, which are in line with the results of Hauschild et al. (2022). The tighter constraints on the empirical accelerations when using non-degraded dynamic models would thus allow to further improve the BRD and HAS results as compared to the corresponding results reported in Table 5.3. This is expected, as the tighter constraints on the empirical accelerations correspond to a stricter adherence to the dynamical modeling, which is more accurate in the non-degraded case. These tighter constraints are less suitable for degraded modeling, as this limits the ability of the empirical accelerations to absorb the errors from the modeling discrepancies.

Overall, the orbit error results presented here are as expected considering the selected degraded settings. Comparison with other Sentinel-6A results in literature has shown that the POD results using COD and CRT and degraded dynamical modeling have 1-2 cm lower 3D RMS orbit errors, while for HAS and BRD this is 2-5 cm larger. This indicates that the more precise GNSS products are better able to cope with the errors introduced by degraded dynamical modeling than the less precise products are. As mentioned in Section 5.2, it was chosen for simplicity to tune for a single set of empirical acceleration settings for all of the GNSS product types with the selected degraded POD setup. Further improvements could potentially be achieved for the HAS and BRD orbit errors by tuning the settings for each product individually. Lastly, as shown, the POD using the HAS and BRD products could improve more from the less degraded modeling as compared to the POD using COD and CRT products. The degraded dynamical modeling could potentially be reconsidered following further analysis of the impact of the POD computation latency and whether the computational burden remains feasible for an on-board processor.

6.2. Clock Errors

The Sentinel-6A receiver clock offsets with respect to GPS time have also been estimated in the real-time POD. These clock estimates have been compared with the reference clock solution to obtain the clock errors, as described in Section 5.4. The LEO satellite clock error fluctuations are of interest for their impact on ground user positioning, since constant biases would be absorbed by the ground user receiver clock. Therefore, the S6A clock error results have been de-biased by their daily means.

An additional correction has been applied to only the clock error results of the POD using CRT products, due to a noticed systematic effect. This effect resembled the product clock differences between the COD and CRT clock products **before** removing the constellation mean per epoch, which was described in Section 4.2.2. This similarity is illustrated in Figure 6.2 by means of the following results shown for DOY 122 taken as a representative day:

1. The clock error result from the real-time POD using CRT products which has been de-biased by its daily mean, shown in black. A sinusoidal shape in this curve can be observed.
2. The GPS constellation mean per epoch of the CRT clock product errors, after having removed the 24-hour GPS constellation mean, shown in blue. This has a similar sinusoidal shape as in 1, though they do not align perfectly. This can be due to the fact that the CRT product mean considers all GPS satellites, while the receiver clock estimate only considers the GPS satellites tracked by S6A. Furthermore, the receiver clock estimate can also be absorbing other effects. This GPS constellation mean per epoch will be used as the correction.
3. The difference between 1 and 2, resulting in the corrected clock errors of the real-time POD using CRT products, shown in light green.

Figure 6.3 shows the same curves for the entire considered data period, further illustrating the periodic repetition of the systematic effect. It can be noticed that there is an artifact at the end of each day for the uncorrected clock error. This is for the last 5 minutes of each day due to the last epoch of the daily CRT orbit products being provided at 23:55:00 and the POD processing having been done in daily arcs until 24:00:00. This artifact remains in the corrected S6A clock errors, since it is not present in the CRT product mean correction.

As mentioned in Section 4.2.2, such systematic effects can arise due to differences in the time conventions used by the respective analysis centers. When comparing the EKF POD result using

CRT products (without correcting) to the BLS POD result using COD products, the receiver clock has absorbed this systematic effect coming from the COD and CRT clock products differences. This systematic difference did not occur when both the EKF and BLS POD used the CRT products. Therefore, this effect has been corrected for in the CRT clock errors by removing the de-biased GPS constellation mean per epoch of the CRT clock product errors as described above.

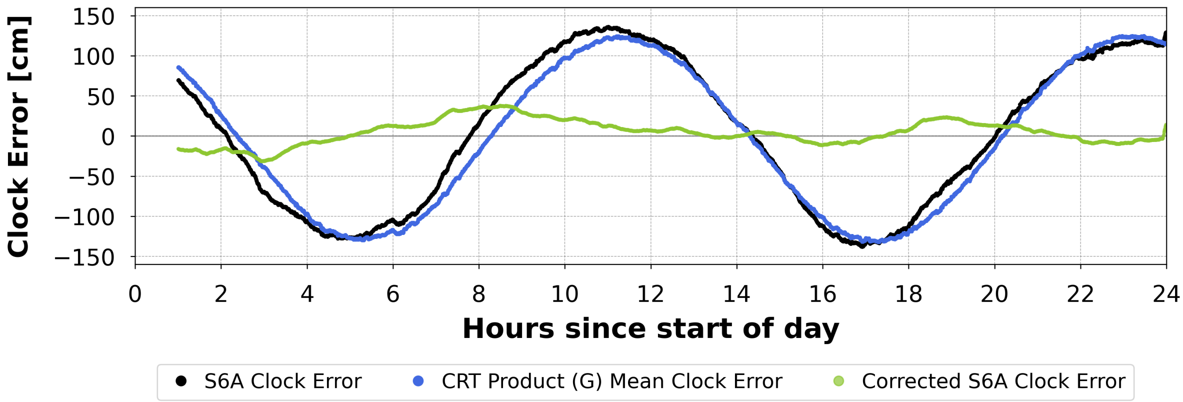

Figure 6.2: The Sentinel-6A clock error obtained using the reduced-dynamic EKF POD approach POD with CRT products on DOY 122 in 2024, which has been de-biased by its own daily mean and is shown in black. The de-biased epoch-wise GPS constellation mean of the CRT clock product errors (in short: CRT product mean) is shown in blue. The S6A clock error corrected by the CRT product mean is shown in light green.

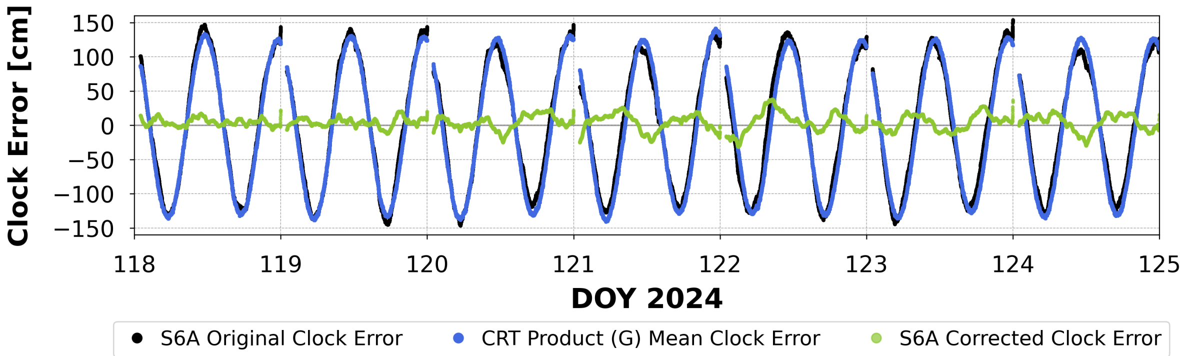

Figure 6.3: The Sentinel-6A clock error obtained using the reduced-dynamic EKF POD approach with CRT products, which has been de-biased by its own daily means and is shown in black. The CRT product mean (blue) and the corrected S6A clock error (light green) are shown here, following the same representation given in Figure 6.2. Here it can be seen that the systematic effect is present in the clock errors for the entire data period.

A similar check was performed for the HAS products, as shown in Figure 6.4. Here, the correction does not provide as much of a difference to the clock errors from the POD using HAS, since there is not such a pronounced systematic effect as there was with the CRT case. Furthermore, the HAS clock products themselves exhibit large outliers during DOY 118 and 119 which are considered to be processing errors, as shown in Section 4.2.2. Using the exact same a posteriori correction as for the CRT clock errors would thus introduce equivalently large outliers into the HAS clock error results for these affected days. It can be noted that, similar to the HAS POD orbit error results, the HAS clock product outliers have not affected the POD clock estimation itself thanks to the data pre-editing. In light of the current study, it was chosen not to correct the HAS clock errors in the same way as the CRT clock errors. This could be revisited upon the availability of HAS products without such processing errors, though the expected impact would be small.

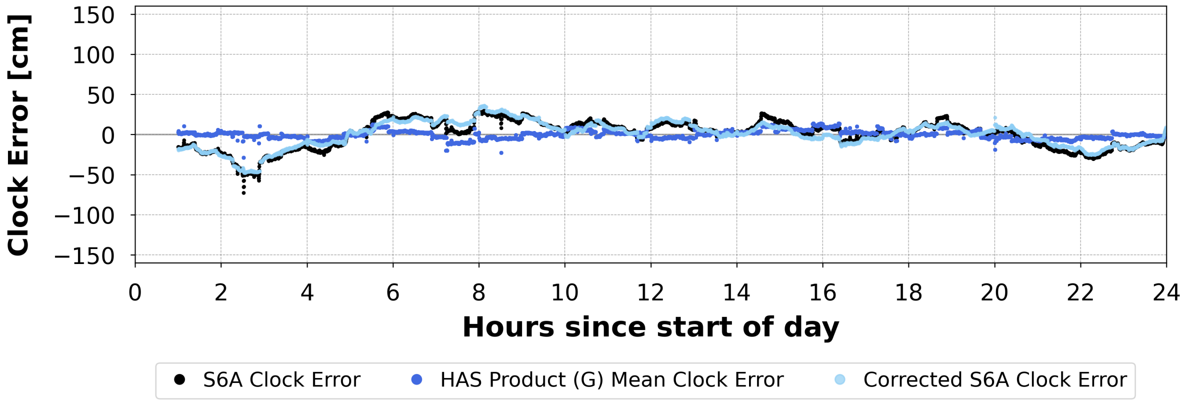

Figure 6.4: The Sentinel-6A clock error using the reduced-dynamic EKF POD approach with HAS products on DOY 122 in 2024, both uncorrected (black) and corrected (light blue) by the de-biased epoch-wise GPS constellation mean of the HAS clock product errors (blue). The uncorrected and corrected results are quite similar, since the HAS product mean does not exhibit any large systematic deviations under nominal circumstances.

Accordingly, the clock results of the real-time POD using each of the products are presented in Figure 6.5. In these results, the first hour is omitted to account for the initialization of the filter. Each figure reports the overall standard deviation, which is taken for the entire data period shown, after correcting for the daily mean and excluding the first hour of each day. Similar to the orbit error results, the clock error results range from best to worst in terms of standard deviation according to the quality of the GNSS products. These standard deviations were 9.9 cm, 10.7 cm, 15.9 cm, and 21.5 cm for the POD using COD, CRT, HAS, and BRD products respectively. When comparing the clock errors of the POD using COD and CRT products, a similar periodic pattern of parabolic-like peaks every 12 hours can be observed. This effect is less visible in the HAS and BRD clock error results due to the noise of the less precise products.

Kunzi and Montenbruck (2022) have performed a similar study of comparing Sentinel-6A clock estimates determined with an EKF and broadcast ephemerides, to those determined with a batch estimator and precise COD GNSS products, both in the reduced-dynamic sense. Kunzi and Montenbruck (2022) also observe periodic variations with parabolic shapes, with the largest time deviations also occurring at 12-hour sampling intervals. Kunzi and Montenbruck (2022) mention that they were unable to fully characterize the cause of this systematic behavior. They potentially attribute this to a difference in GPS time realization between the COD and BRD products. However, they did not present POD clock errors using the same products in the different processing methods as is done in this study, where this periodic pattern was also observed. The standard deviation results reported in Kunzi and Montenbruck (2022) for the clock errors using BRD products are around 20-30 cm, depending on the selected ISB process noise value (which could not be configured in this thesis in the `FAST` tool). Their result is similar to the 21.5 cm standard deviation for the BRD clock errors reported here, indicating that this result is in line with the expectations.

A similar approach was also adopted by Wu et al. (2024) to assess the clock estimate error for Sentinel-3B on DOY 227 in 2018. In that study, COD products were used for the reduced-dynamic batch estimation and CRT products for the real-time filter that was, however, implemented in the kinematic sense. Wu et al. (2024) report a standard deviation of around 6 cm for this clock error, though they did not report their corresponding orbit errors. The difference between the 3D RMS of the S6A orbit errors using the BLS with COD products and the EKF with CRT products presented in this thesis is around 3 cm. This would lead to the expectation that the corresponding clock errors would be of a similar order. This indicates that the 6 cm difference reported by Wu et al. (2024) could also potentially be attributed to differences in the processing methods to a certain degree, though this result was for a different satellite during a different period. As mentioned, a direct comparison using the same GNSS products and considering the same LEO satellite would allow for a better assessment of this, though such a comparison was not found in other literature.

The standard deviations for the S6A clock errors using COD and CRT products presented here are much larger than the corresponding POD orbit errors, indicating that these could be overly pessimistic. As highlighted above, this could also potentially be attributed to the limitation that this clock error analysis is ultimately between two processing methods, especially considering the exact same products were used for the COD clock error results. However, from the work in Kunzi and Montenbruck (2022) a 10 cm improvement in the standard deviation of the clock error was obtained from the ISB process noise tuning. It can be noted that the dedicated tuning described in Section 5.3 was only focused on improving the orbit errors and not necessarily the clock errors. With further tuning and the availability of an ISB process noise setting, the presented clock errors could potentially be improved. Furthermore, as mentioned in Section 5.4, it can be noted that the degraded dynamical models did not have a noticeable impact on the clock error results. Lastly, no reference in literature was found as yet to directly compare the clock errors of POD using HAS products. The standard deviations of the clock errors are around 6-7 cm larger than the 3D RMS orbit errors for each of the corresponding GNSS products, including HAS. Therefore, the clock errors of the POD using HAS products are considered to be in line with the expectations for this study.

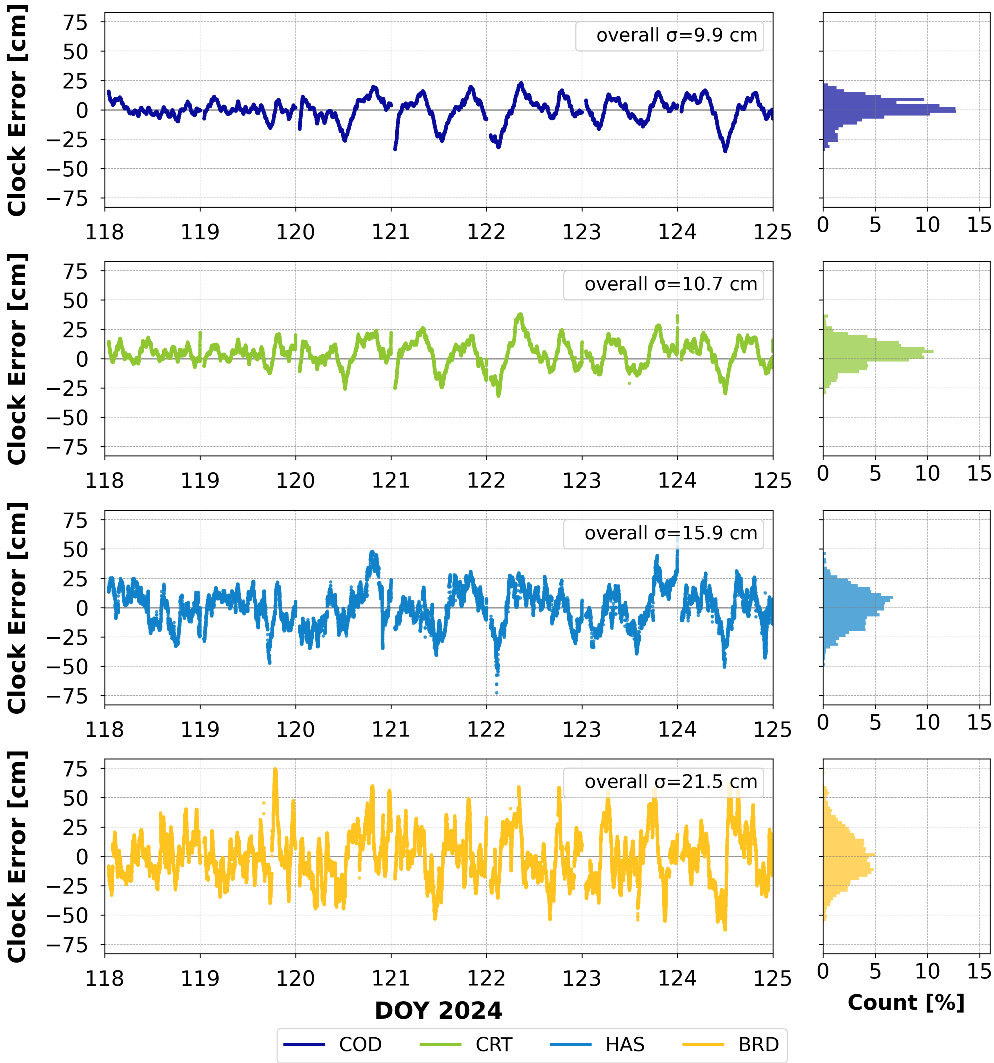

Figure 6.5: The Sentinel-6A clock errors obtained using the reduced-dynamic EKF POD approach with the various types of GNSS products. The S6A clock estimates have been computed with respect to GPS time, and the clock errors are taken with respect to the reference clocks computed using reduced-dynamic BLS with only COD products, as described in Section 5.4. The clock errors have been de-biased by their daily mean and the standard deviation was computed excluding the first hour of each day to account for the filter initialization. The clock errors from the POD using CRT products have additionally been corrected by the de-biased GPS constellation mean per epoch of the CRT products.

6.3. Signal-In-Space Range Errors (SISRE)

As mentioned in Chapter 4, the combined effect of the orbit and clock errors can be evaluated using the Signal-In-Space Range Error (SISRE). The weights used in Equation 4.2 and Equation 4.3 are determined based on the orbital height of the GNSS constellation. Accordingly, a PNT constellation situated in LEO would constitute different SISRE weights than those used for MEO GNSS, depending on the altitude that the constellation is placed at. In the case of Sentinel-6A, the mean altitude is 1336 km. Based on this, the weights of w_R = 0.617 and $w_{T,N}$ = 0.556 were selected, corresponding to the weights given in Reid et al. (2020b) for an altitude of 1200 km.

Using these weights, the SISRE results are presented for each product in Figure 6.6. These were 1.7 cm, 2.9 cm, 5.6 cm, and 8.4 cm for the SISRE(orb) RMS and 10.0 cm, 12.4 cm, 16.6 cm, and 23.5 cm for the SISRE RMS of the POD using COD, CRT, HAS, and BRD products respectively. As mentioned, the orbit and clock errors are used to compute the SISRE, where the statistics for all of these results are summarized together in Figure 6.7. As presented in Section 4.2.2, the weights for MEO GNSS are much higher for the R and clock errors as compared to the T and N components due to the high orbital altitude. These weights are much more balanced between all of the components for LEO satellites, as these are situated much closer to Earth than MEO GNSS. Accordingly, the SISRE(orb) results are as expected, being more or less in between the values of the individual RTN components. Furthermore, the SISRE values themselves are dominated by the clock errors, due to the larger values of the clock errors as compared to the orbit errors.

Kunzi et al. (2023) present a LEO-PNT payload concept using similar GNSS-based on-board reduced-dynamic EKF POD with only broadcast ephemerides, and a Chip-Scale Atomic Clock (CSAC) that is actively aligned to the GPS time through clock-steering. In that work, they report a 3D RMS orbit error of 11 cm for Sentinel-6A reduced-dynamic EKF POD using BRD products on DOY 362 in 2022. They present a clock error standard deviation of 23 cm based on ground-based tests of the CSAC clock-steering. With these S6A orbit errors and CSAC clock errors, they report a SISRE RMS of 24 cm, which is close to the 23.5 cm when using BRD products reported here. This indicates that the SISRE results of the POD using BRD products presented here are in line with the expectations of this type of LEO-PNT navigation payload concept. It should be noted that though the USO on Sentinel-6A is a more stable clock, as mentioned by Kunzi and Montenbruck (2022), it was not designed to be kept synchronized to the GPS time. Since the S6A USO is free-running, its real-time clock offset estimates may not fully capture longer-term effects, potentially contributing to the clock errors that are more similar to those of the steered CSAC.

The SISRE results of the POD using COD and CRT products may be too pessimistic due to the larger clock errors as compared to the corresponding orbit errors. However, the reader is reminded that these would not directly be readily available to operational LEO-PNT satellites, making this a less relevant result for the purposes of this study. Based on the previous discussion of the clock errors of the real-time POD using HAS products, the corresponding results are also considered to be in line with the expectations for this study. Therefore, the POD results presented in this chapter are considered to be sufficiently representative of the orbit and clock errors that can be obtained from on-board real-time GNSS-based POD for LEO-PNT satellites within the described limitations of this study. Accordingly, these orbit and clock errors have been used in end-to-end PPP simulations to quantify their impact on PPP user performance, which is described in the next two chapters.

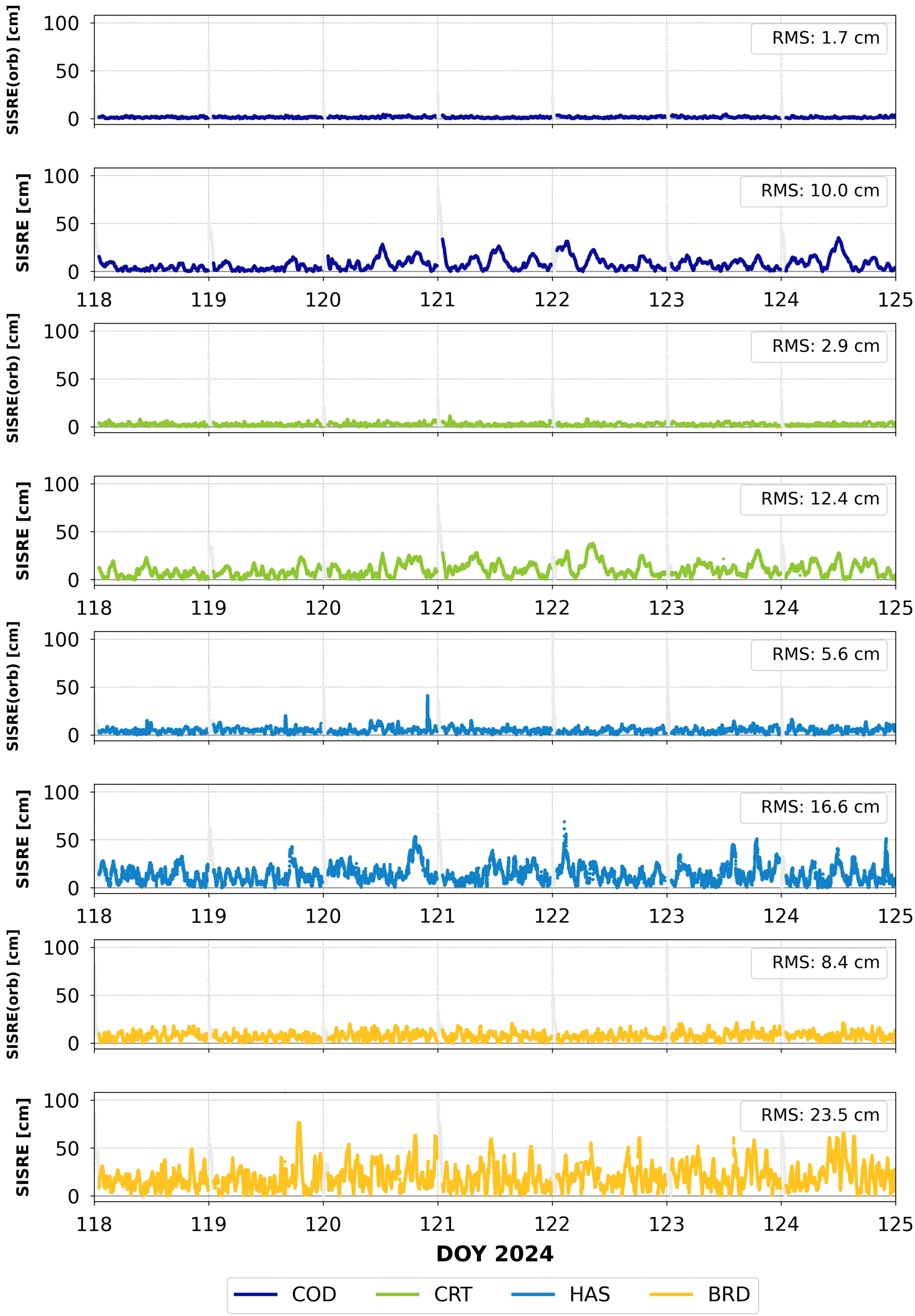

Figure 6.6: The Sentinel-6A Signal-In-Space Ranging Errors (SISREs) obtained using the reduced-dynamic EKF POD approach with the various types of GNSS products. These have been computed using the previously presented S6A orbit and clock errors shown in Figure 6.1 and Figure 6.5 respectively. The RMS statistics are computed excluding the first hour of each day to account for the filter initialization.

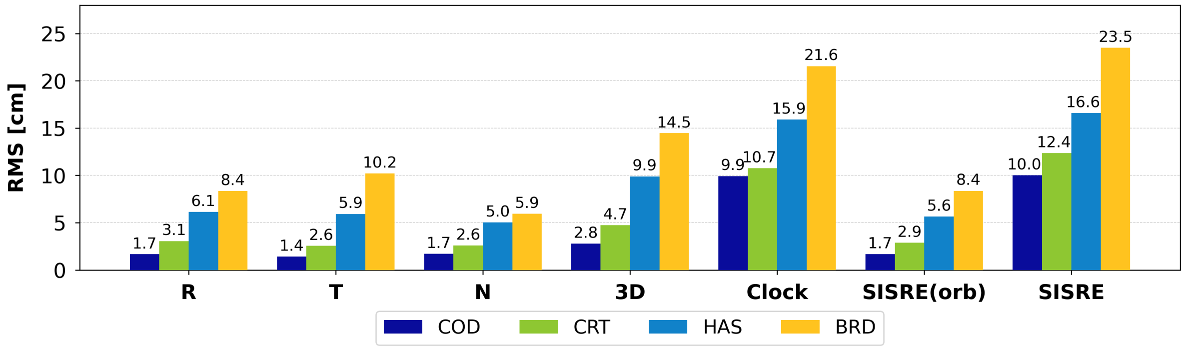

Figure 6.7: Summary of the statistics of the Sentinel-6A POD errors obtained using the reduced-dynamic EKF POD approach with each of the considered products over the considered data period of DOY 118 to 124 in 2024. The first hour of each day is neglected to account for the initialization of the filter.

7

PPP Setup

This chapter will first introduce the tool that was used to evaluate the impact of the LEO satellite orbit and clock errors on PPP performance in Section 7.1. Then, the more specific aspects of settings up the MEO and LEO space segments in this tool for this study are discussed Section 7.2 and Section 7.3 respectively. Finally, Section 7.4 will describe the ground user segment and user performance metrics considered in the PPP analysis.

7.1. LEOPARD: In-house End-to-End PPP Simulation Tool

A tool called LEOPARD (Massarweh, 2024a), which stands for “LEO-enhanced Positioning with Ambiguity Resolution Demonstrator”, was available for performing the PPP analysis in this study. The tool can be described as an end-to-end simulator that can first generate code and phase observations based on a configured space segment and user segment, and then perform PPP(-AR) using these observations, as shown in Figure 7.1. While the general mathematical approach to PPP was described in Section 3.2.2, the exact observation generation and PPP(-AR) algorithms implemented in the LEOPARD tool are internal to its developer and are considered beyond the scope of this thesis, and will therefore not be further elaborated in this work. Furthermore, only float-PPP will be considered in this study, as PPP-AR has also been deemed beyond the scope of this thesis. Additionally, literature has shown that more significant improvements in convergence time from using LEO-PNT are expected for float-PPP users, as fixed-PPP solutions can already achieve rapid convergence of less than 10 minutes with multi-GNSS alone (Li et al., 2023).

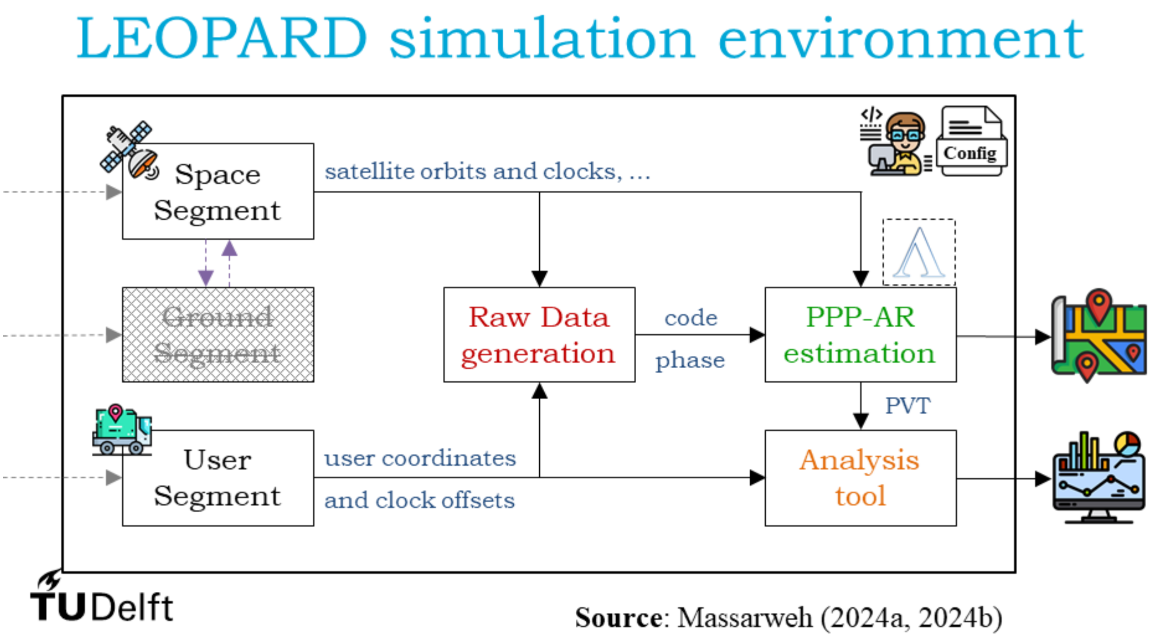

Figure 7.1: A graphical representation of the LEOPARD tool architecture (Massarweh, 2024a), (Massarweh, 2024b).

A short overview can be given for the LEOPARD configuration used in this study, which is based on the setup presented by Massarweh (2024b). This study will consider a MEO space segment for GPS and Galileo, and a LEO space segment for the LEO-PNT satellites. As shown in Figure 7.1, the correction estimation performed by the ground segment is not simulated within the LEOPARD tool. Instead, real-world data is used for the MEO space segment, namely the GNSS orbit and clock products presented in Section 4.2. For the LEO space segment, on-board real-time orbit and clock estimation is assumed. Additionally, the case where the LEO satellite orbit errors are determined on board and the LEO satellite clock errors are determined on ground is also considered, similar to the approach adopted by Li et al. (2024). This is done by only considering the on-board LEO satellite orbit errors and no LEO satellite clock errors, thus assuming that the LEO satellite clocks have already been (perfectly) corrected. More details on the specific configuration of these space segments will be given in the next two sections, followed by the configuration of the user segment given in the last section.

Once the space segment and user segment are defined, the LEOPARD tool generates the observation data between these two segments by modeling, which includes the following realistic error sources. The observation noise is taken as Gaussian with zero mean. The receiver clock offset is modeled as a random walk, and an ISB parameter modeled as a constant process is included for each additional constellation. This is also valid for the LEO-PNT constellation as it is assumed to have its own system time. For the atmospheric effects, a single-layer ionosphere is modeled at 450 km, and the GPT2w model (Böhm et al., 2015) is used for the hydrostatic and wet tropospheric delays. Furthermore, corrections for the relativistic effects, Earth rotation during signal propagation, phase wind up, and phase center offset and variations are applied. The solid Earth and ocean tides are modeled following the IERS2010 convention. It can be noted that in this study, no cycle slips or multipath effects are modeled.

Once the observations have been generated, these are then used in the PPP estimation. For the float-PPP estimation, a Kalman filter is used. The estimated parameters are the (ground user) receiver position, the receiver clock offset and ISBs, the ionospheric delays, and the (zenith) wet troposphere delay. In the estimation, the corrections for the relativistic effects, Earth rotation, phase wind up, PCOs and PCVs, (zenith) hydrostatic troposphere delay, and solid Earth tides are modeled in exactly the same way as is done in the data generation. Meanwhile, the ocean tide modeling is neglected in the estimation. Furthermore, the initial ground user position error is set to 10 km, while the process noise for position, receiver clock, and ionospheric delays are set to 1 km/$\sqrt{\text{s}}$, and for the ZWD this is set to 0.1 mm/$\sqrt{\text{s}}$.

7.2. MEO Space Segment Configuration

For the MEO space segment, the GPS and Galileo constellations were simulated using the GNSS orbit and clock products introduced in Chapter 4. The COD orbit products were used as the nominal (error-free) positions of the MEO GNSS satellites. For the PPP analysis, only CRT and HAS GNSS products were considered for the MEO constellations. Both the CRT and HAS products are available to ground users in real time through the Internet, and the HAS products are also available through Galileo's E6 signal, as described in Section 4.2. The GNSS broadcast ephemerides (BRD products) were not considered to be used by the ground user in this study as these are less suitable for PPP. Accordingly, the CRT and HAS RTN orbit errors that were presented in Section 4.2.2 were applied to the Nominal (COD) orbits in the PPP simulations. As each of the orbit products are given at a rate of 5 minutes, these values were interpolated to obtain the desired time step (10 seconds) for the PPP simulation. An 11th order Lagrange polynomial interpolator (Teunissen and Montenbruck, 2017, Annex A) was used, as this was found to provide interpolation errors of less than mm-level, which would not have a noticeable impact on the PPP performance.

As previously introduced in Section 4.2.1, there were also specific healthy satellites entirely missing from each of the CRT and HAS GNSS products, as well as data gaps present in the HAS products. During such data gaps, no PPP observation data was generated for the missing satellite(s), replicating the real-world conditions of using such product streams. However, as the interpolation process relied on windows centered on the desired epoch, approaching a data gap meant that there were insufficient points within the window to perform a reliable interpolation. Corresponding to the 11th order Lagrange interpolator, one window consisted of 12 reference data points spaced at the 5-minute intervals. Consequently, the first and last 30 minutes of any sufficiently long data arc (longer than one interpolation window), as well as data arcs shorter than one window duration could not be interpolated reliably. These epochs were considered as extensions of the data gaps, during which no observations were generated for those satellites. It is worth noting that this interpolation approach is employed due to the use of CRT and HAS products in SP3 format. In a practical real-time setup, the latest available corrections from the CRT or HAS SSR streams still within their validity period would be used in the event of such data gaps. In this regard, the longer data gaps due to the interpolation approach adopted in this study lead to a more pessimistic scenario for the MEO constellation availabilities as compared to a real-world setup.

The MEO GNSS satellite clock errors were also incorporated into the PPP simulation. The adjusted CRT and HAS clock errors as compared to the COD clock products, as presented in Section 4.2.2, were then used along with their corresponding orbit errors. The CRT and HAS clock products were provided at rates of 10 and 30 seconds respectively. Thus, the HAS clocks were linearly interpolated to obtain the desired PPP observation time step of 10 seconds. Furthermore, the HAS clock products also exhibited data gaps, and it can be noted that these did not always coincide with the gaps in the orbit data. A similar strategy was adopted, where no observations were generated for a given satellite during the epochs with gaps in its clock data. As will be mentioned in the following section, only DOY 121 in 2024 is considered for the PPP analysis. Therefore, the HAS clock outliers on DOY 118 and 119 presented in Section 4.2.2 are not a concern here.

A summary of the total number of satellites considered per constellation and per product is given in Table 7.1, based on the nominal product availabilities per satellite discussed in Section 4.2.1. Furthermore, two frequencies were used for each of the MEO constellations, namely L1/L2 for GPS (G) and E1/E5a for Galileo (E). Lastly, following Massarweh (2024a), the noise applied to the measurements was done with standard deviations of 30 cm and 3 mm for the pseudorange and carrier phase observations respectively for each of the frequencies.

Table 7.1: Overview of the space segment configuration for PPP simulation. The unusable satellites E14, E18, and G01 have been left out for all products. The healthy satellites entirely missing in the CRT products are E11, E19, and G28; and for the HAS products G13 and G22 are missing.

Frequencies	**GPS (G)**	L1 (1575.42 MHz) & L2 (1227.60 MHz)
	Galileo (E)	E1 (1575.42 MHz) & E5a (1176.45 MHz)
	LEO (L)	E1 (1575.42 MHz) & E5a (1176.45 MHz)
Measurement noise (standard deviation)	**Pseudorange**	30 cm
	Carrier phase	3 mm
Total number of satellites per MEO product	**COD (nominal)**	G: 31; E: 23
	CRT	G: 30; E: 21
	HAS	G: 29; E: 23

7.3. LEO Space Segment Configuration

As described, the main topic of interest in this research is the impact that the LEO satellite orbit and clock errors determined using on-board real-time POD could have when they are included in PPP that is already using MEO GNSS. This section will describe how the LEO satellite orbit and clock errors presented in Chapter 6 are incorporated into the PPP simulation. In this study, the following two approaches to constructing the LEO space segment were considered.

In the first approach, a single LEO satellite corresponding exactly to the Sentinel-6A (S6A) orbit was used. Here, the precise Sentinel-6A reference orbits provided by the Copernicus Data Space Ecosystem (CDSE) were used as the nominal (error-free) orbits. The differences between the nominal orbits and the POD results presented in Chapter 6, namely the S6A orbits determined using COD, CRT, HAS, and BRD products, were then used to emulate the corresponding error levels of such on-board determined “LEO products”. This approach is the most realistic in terms of the time series of errors corresponding to the trajectory flown by the satellite. However, due to the nature of the low Earth orbit, a single satellite is only in view of a specific user a few times a day and for short periods of time. This leads to a limited expected impact of a single additional LEO satellite for a ground PPP user. For this reason, the analysis of the single-LEO approach has been limited to only including the LEO satellite orbit errors and not yet considering LEO satellite clock errors.

In the second approach, a small constellation of satellites in S6A-like orbits is simulated. For simulating such a LEO constellation, first nominal orbits are generated by propagating the Keplerian parameters corresponding to Sentinel-6A's orbit, as given in Table 7.2 (Cullen et al., 2021). Multiple planes are created and are spaced evenly in Right Ascension of the Ascending Node (RAAN). Furthermore, multiple satellites can be added to each plane. The S6A orbit errors computed in the RTN frame are then added to the nominal orbits generated for the constellation. The S6A clock errors presented in Chapter 6 were also incorporated into the constellation study. Using this method, the total number of satellites that could be incorporated was limited by the amount of data that was generated in the POD part, which in turn was dictated by the 7 days of HAS data that was provided for this study, as described in Section 4.2.

Based on the 7 days of POD results, the selected LEO constellation configuration consisted of 7 planes with 4 satellites per plane, leading to a total of 28 LEO satellites. The POD data from a single day in the data period (DOY 118-124 in 2024) was used for the time series of the orbit and clock errors for each plane, leading to the choice of 7 planes. It was found that with 4 evenly-spaced satellites per plane, there would be at least 1 LEO satellite in view for 100% of the time for the selected user. Furthermore, at 4 satellites per plane there would be no overlap of satellites from a single plane for the user, meaning there would not be any 2 or more satellites with the same error time series in view at the same time. As mentioned, this constellation configuration was selected based on the availability of the data and its validity for using the S6A POD results. It can therefore be noted that as the focus of this work is the impact of the LEO satellite orbit and clock errors, it does not represent a study on the design and optimization of the constellation configuration itself.

Furthermore, contrary to the MEO satellite orbit and clock errors, as the LEO POD results were obtained at a rate of 10 seconds, no interpolation was needed for the LEO satellite orbits and clock errors that were provided as inputs to the PPP tool. The precise reference orbits for S6A, however, did need to be interpolated, as these were provided per 60 seconds. A similar strategy as for the MEO interpolation was used for this, and no gaps were present. Furthermore, the LEO satellites were simulated to transmit at E1/E5a as well, and the same measurement noise as MEO was also adopted for the LEO satellites, as summarized in Table 7.1.

Table 7.2: Simulated LEO constellation configuration, based on the Sentinel-6A reference orbital parameters given in Cullen et al. (2021). The planes are spaced evenly over the Right Ascension of the Ascending Node (RAAN) and the satellites are spaced evenly within a plane.

Parameter	**Value**
Semi-major axis	7714.432 km
Eccentricity	0.000098
Inclination	66.042°
Number of planes	7
Satellites per plane	4

As described in the previous sections, this study considers various options for the constellation configuration and satellite orbit and clock error levels for the MEO and LEO space segments. These options are summarized as follows:

- **MEO space segment:**
  - **Constellation configurations:** GPS-only (G), Galileo-only (E), or GPS+Galileo (G+E).
  - **Orbit and clock errors:** Nominal (no errors), CRT GNSS products, or HAS GNSS products.
- **LEO space segment:**
  - **Single LEO satellite configuration:**
    - **Only on-board orbit errors and no clock errors:** Nominal (no errors), or LEO products obtained from on-board real-time POD using COD, CRT, HAS, or BRD GNSS products.
  - **28-satellite LEO constellation configuration:**
    - **Only on-board orbit errors and no clock errors:** Nominal (no errors), or LEO products obtained from on-board real-time POD using COD, CRT, HAS, or BRD GNSS products.
    - **Both on-board orbit and clock errors:** LEO products obtained from on-board real-time POD using CRT or HAS GNSS products.

The cases considered in this study consist of the various possible combinations of the above-listed options. For the single LEO and the LEO constellation configurations, each of the LEO product types were analyzed considering only LEO satellite orbit errors and no LEO satellite clock errors. For the analysis using LEO satellite orbit and clock errors, only a subset of cases were selected. Lastly, it can be noted that the Nominal LEO satellite orbits were also used in the PPP computations as a sanity check, though the results for these cases will not be presented in this report since they have limited real-world applicability. In turn, the Nominal MEO cases are still presented to isolate the effects of the LEO satellite orbit and clock errors.

7.4. User Segment Configuration and User Performance Metrics

In the previous sections, the setups for the MEO and LEO space segment configurations considered in this study were defined. For the user segment, the scenario of kinematic float-PPP was assessed for a static ground user located at a position of 5° longitude, 50° latitude, and at a height of 370 m, which is approximately the location of the Redu station in Belgium. The PPP analysis was conducted for the time period of 01:00 to 23:00 on DOY 121 in 2024, which was selected a representative day. The first hour of the day was neglected to account for the larger LEO satellite orbit errors due to the initialization of the POD filter. The last hour of the day was neglected to account for the MEO satellite orbit product interpolation ending around 23:30. As described in Section 7.1, the code and phase observations are generated based on these defined space and user segments, where the observations are then used in the PPP estimation procedure. Lastly, it can be noted that an elevation mask of 7° was employed in the estimation procedure for the considered user. This PPP simulation setup represents an optimistic scenario, considering open-sky viewing conditions free from obstructions, along with no cycle-slips or multipath effects.

The PPP simulations for this thesis have been conducted based on the configurations outlined in this chapter. The results of these simulations will be presented in the next chapter, where the following metrics have been adopted to assess the PPP user performance:

- **Convergence time:** The PPP convergence time was statistically assessed by computing the solutions for 1261 windows of 60 minutes, each shifted by 1 minute starting from 01:00 to 23:00 on the selected day, and subsequently taking the 90th percentile of these results. The criterion for convergence was set at the first epoch where the rest of the epochs after it are below 20 cm, which was considered for each of the components: East (E), North (N), Up (U), 2D (Euclidean norm of E and N), and 3D (Euclidean norm of E, N, and U). It can be noted that only the latter two will be presented in the results for brevity.

- **Positioning accuracy after convergence:** The PPP accuracy after convergence was statistically assessed by computing solutions for a single window from 01:00 to 23:00 on the selected day. Then, the RMS for each component (E/N/U/2D/3D) was computed for the period of 02:00 to 23:00, where the first hour of the window was neglected to account for the PPP convergence time. Furthermore, the cumulative distribution of the position errors was also computed according to the percentage of epochs from 02:00 to 23:00 that were below certain error values. Similar to the convergence time results, only the 2D and 3D accuracy results will be presented in this report for brevity.

8 PPP Results

This chapter presents the PPP results that were obtained following the setup described in Chapter 7. First, the performance of MEO GNSS alone is characterized in Section 8.1. Next, the results considering a single LEO satellite in addition to MEO GNSS are presented Section 8.2. Then, the results for MEO GNSS augmented by a constellation of 28 LEO satellites are given in Section 8.3. That section is further divided into Section 8.3.1 where only LEO satellite orbit errors have been considered, and Section 8.3.2 where both LEO satellite orbit and clock errors have been included.

8.1. MEO GNSS-Only Performance

This section first characterizes the performance of the PPP setup and scenario described in Chapter 7 considering only the use of the MEO GNSS space segment and not yet considering any LEO satellites. As mentioned in Section 7.2, there are 3 types of MEO GNSS products that have been considered. These are the COD, CRT, and HAS products, where the COD products are used here as the Nominal orbits and clocks with no errors, thus representing a perfect case. Furthermore, the cases of using GPS-only (G), Galileo-only (E), and GPS+Galileo (G+E) have also been considered. As mentioned in Section 7.4, a kinematic float-PPP user located at Redu, Belgium has been considered for the period of 01:00 to 23:00 on DOY 121 in 2024 in this analysis. The number of GPS and Galileo satellites used in this scenario is shown in Figure 8.1. Here, the nominal number of satellites is given based on the COD GNSS products, along with the number of satellites missing from the CRT and HAS GNSS products as compared to COD. These differences are due to data gaps or entirely missing healthy satellites in these real-time products, as described in Section 7.2. These missing satellites illustrate that differences in PPP performance between the MEO GNSS products is not necessarily only due to the level of orbit and clock errors of the products, but also potentially due to having less satellites in view at a given epoch.

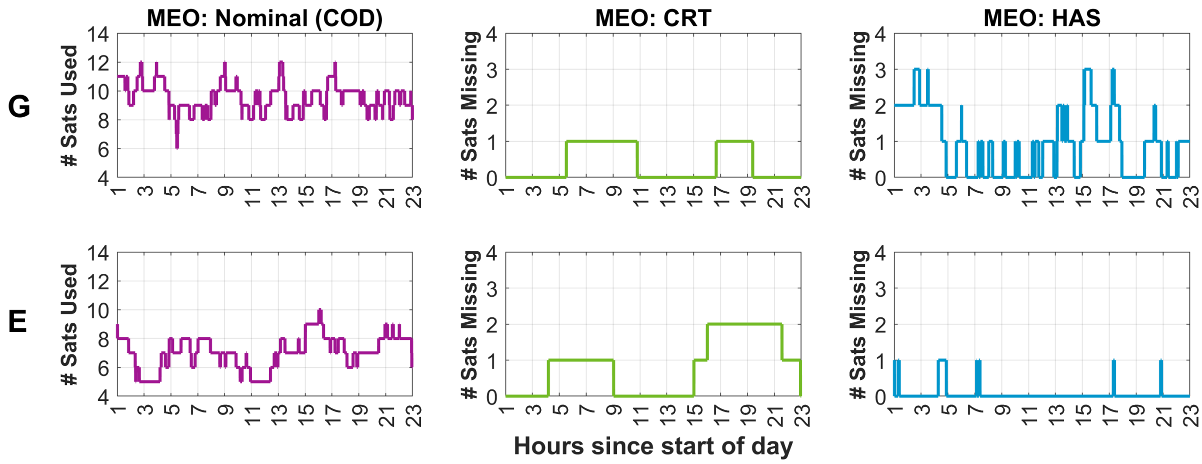

Figure 8.1: The nominal number of satellites used by the selected user at Redu from 01:00 to 23:00 on DOY 121 (2024) based on the COD GNSS products, along with the number of satellites missing in the CRT and HAS GNSS products as compared to the COD products, which occur due to data gaps and entirely missing healthy satellites.

The positioning errors for the MEO GNSS-only PPP scenarios over the considered period of 01:00 to 23:00 on DOY 121 in 2024 are shown in Figure 8.2 for each combination of MEO GNSS product type (Nominal (COD), CRT, HAS) and GNSS constellation(s) (G, E, G+E). The 2D and 3D RMS errors are shown in Table 8.1, which have been computed from 02:00 to 23:00 on the selected day for the PPP accuracy metric as described in Section 7.4. The RMS positioning error values from the PPP simulations here fairly align with the expectations based on recent publications using real-world data.

For the CRT GNSS products, Gao et al. (2023) have computed the average kinematic float-PPP positioning errors of 37 global stations over the period of 20 days. Their positioning accuracy results consist of 2D RMS errors of 2.8 cm, 4.5 cm, and 2.2 cm, and 3D RMS errors of 5.1 cm, 7.7 cm, and 4.1 cm for GPS-only, Galileo-only, and GPS+Galileo respectively. Furthermore, Du et al. (2022) have also studied kinematic float-PPP with CRT products, reporting 2D RMS errors of 3.2 cm and 2.5 cm, and 3D RMS errors of 5.2 cm and 4.3 cm for GPS-only and GPS+Galileo respectively, computed as an average of 90 global stations over a period of 31 days. These values are in approximately the same order as the corresponding results using CRT GNSS products presented in Table 8.1. It can be noted that the 3D positioning accuracy of G+E with CRT products reported here is slightly worse than that of G-only with CRT products. This is expected to be due to the larger errors in the Galileo CRT GNSS orbit and clock products as compared to those of GPS.

As Galileo HAS is a fairly new service, not many comparable publications on its kinematic PPP performance were found at the time of writing. The recent publication of Gao et al. (2025) report 2D RMS errors of 13.2 cm and 10.4 cm, and 3D RMS errors of 21 cm and 15.9 cm for GPS-only and Galileo-only respectively for the average kinematic float-PPP accuracy of 56 global stations over 7 days, which are slightly better than the results reported in Table 8.1.

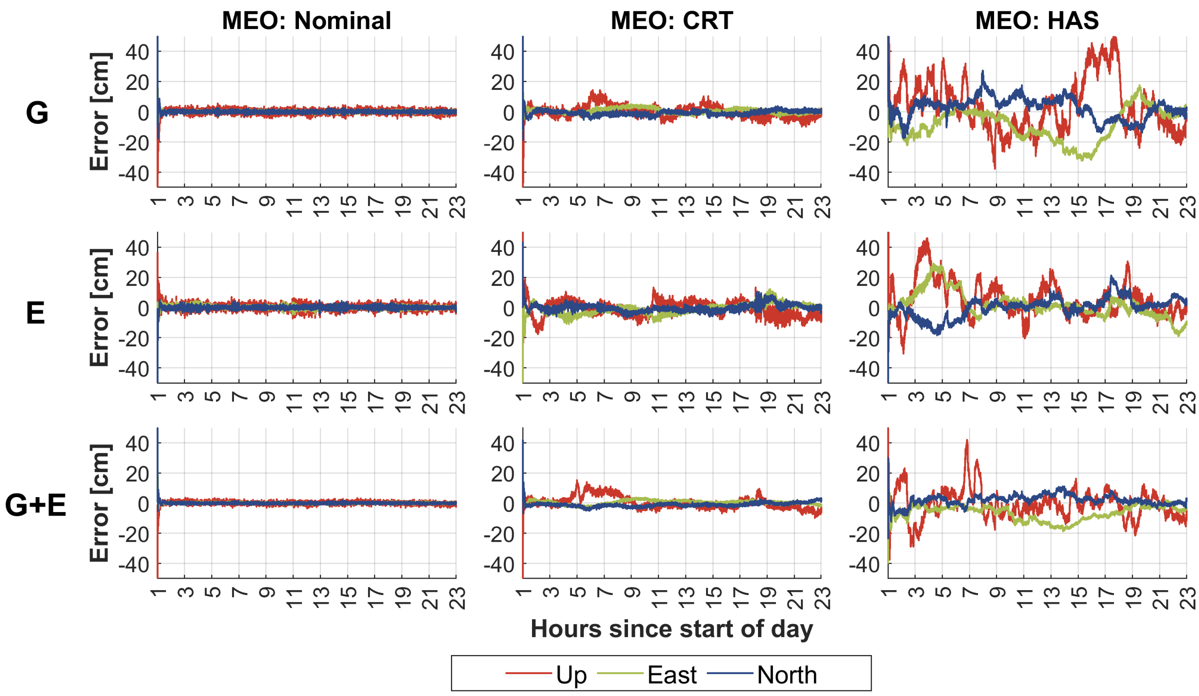

Figure 8.2: positioning errors for a kinematic float-PPP user located at Redu, Belgium over the considered period of 01:00 to 23:00 on DOY 121 in 2024. These results are given for the various combinations of MEO GNSS products (Nominal (COD), CRT, HAS) and constellation combinations (G, E, G+E), where no LEO satellites have been considered as yet.

Table 8.1: RMS of the 2D and 3D positioning errors in cm computed from 02:00 to 23:00 on DOY 121 in 2024 for a kinematic float-PPP user located at Redu, Belgium using MEO GNSS, corresponding to the results of the MEO GNSS product and constellation combinations presented in Figure 8.2.

	MEO: Nominal		**MEO: CRT**		**MEO: HAS**	
	2D	**3D**	**2D**	**3D**	**2D**	**3D**
MEO: G	0.9	1.6	2.3	4.4	15.8	23.9
MEO: E	1.3	2.2	4.1	6.1	11.1	17.2
MEO: G+E	0.6	1.1	2.2	4.7	8.9	13.2

As described in Section 7.4, the 2D and 3D convergence time was assessed by performing the PPP simulations for 1261 windows of 60 minutes each, that have been taken 1 minute apart from 01:00 to 23:00 on DOY 121 in 2024. Figure 8.3 shows the results for each of the 1261 windows in thin lines colored for the example case of using HAS GNSS products and only GPS, along with the 50th and 90th percentile which are indicated by the thick dotted and thick solid line respectively. Accordingly, the 90th percentile convergence results for all of the MEO GNSS-only cases are shown in Figure 8.4, and their convergence times to 20 cm are reported in Table 8.2.

As mentioned in Section 7.4, the 90th percentile was selected to statistically assess the convergence time. However, as can be noted from the HAS GPS-only case, this 90th percentile can be more susceptible to some outlying cases. This is suspected to have occurred in this HAS GPS-only case due to the previously mentioned HAS GPS data gaps. For example, an outlying group of blue thin lines corresponding to windows starting from 07:00-08:00 can be observed. From Figure 8.1 it can be seen that this was a period with less nominal GPS satellites in view (8-9 satellites as opposed to 10-12 satellites over other periods), as well as around 1 satellite missing from the HAS data. Furthermore, the convergence at the 50th percentile is not as affected by such outlying cases, as shown by the dotted line in Figure 8.3.

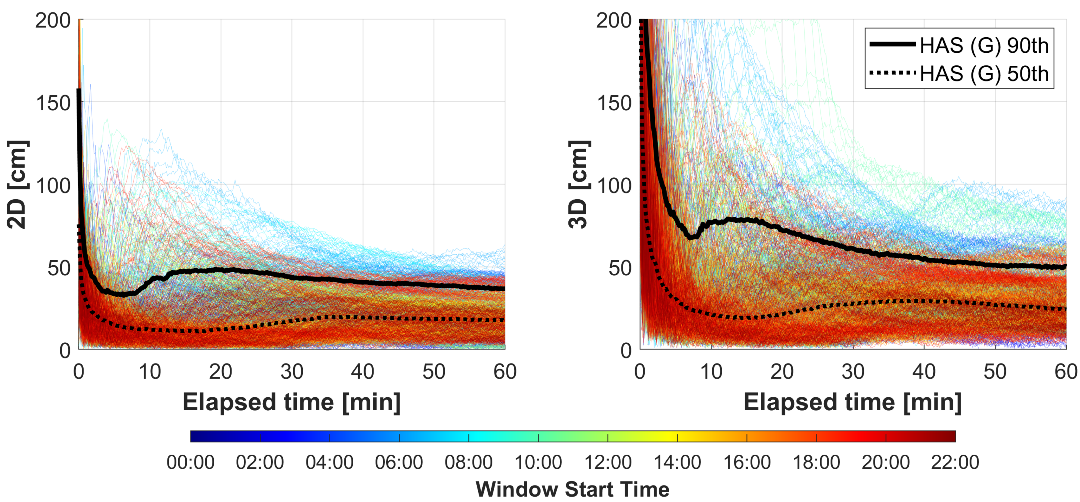

Figure 8.3: 2D and 3D positioning errors for a kinematic float-PPP user located at Redu, Belgium for 1261 windows of 60 minutes taken over the considered period of 01:00 to 23:00 on DOY 121 in 2024 for the example case of using HAS GNSS products and GPS-only. Each of the 1261 windows is illustrated by the faint blue lines, and the 50th and 90th percentiles of these results are illustrated by the dotted and solid thick lines respectively.

Comparing the convergence results to existing literature is less straightforward due to differences in the selected convergence criteria and statistical metrics. For the CRT products, the mean convergence times to 10 cm reported in Gao et al. (2023) are 24.2 minutes, 27.4 minutes, and 20.5 minutes for GPS-only, Galileo-only, and GPS+Galileo respectively. At this threshold of 10 cm, the convergence times in the results of this thesis are 31.5 minutes and 18.7 minutes for GPS-only and GPS+Galileo respectively. The result for Galileo here did not converge to 10 cm within 60 minutes, which could partly be due to the missing Galileo satellites in the CRT products.

For the HAS products, Gao et al. (2025) consider 20 cm and 40 cm thresholds for horizontal and vertical respectively, which is less stringent than the criteria in this work. They report maximum convergence times of around 52-57 minutes, while the 2D convergence to 20 cm is not achieved within 60 minutes in the 90th percentile results here. This indicates that the HAS PPP results are more on the pessimistic side, which could be due to the HAS data gaps.

Table 8.2: Convergence times to 20 cm in minutes (90th percentile) for a kinematic float-PPP user located at Redu, Belgium on DOY 121 in 2024 using MEO GNSS, corresponding to the results of the MEO GNSS product and constellation combinations presented in Figure 8.4.

	MEO: Nominal		**MEO: CRT**		**MEO: HAS**	
	2D	**3D**	**2D**	**3D**	**2D**	**3D**
MEO: G	4.0	7.3	4.8	10.2	x	x
MEO: E	8.3	27.2	17.0	41.5	x	x
MEO: G+E	2.2	4.7	2.7	6.0	x	x

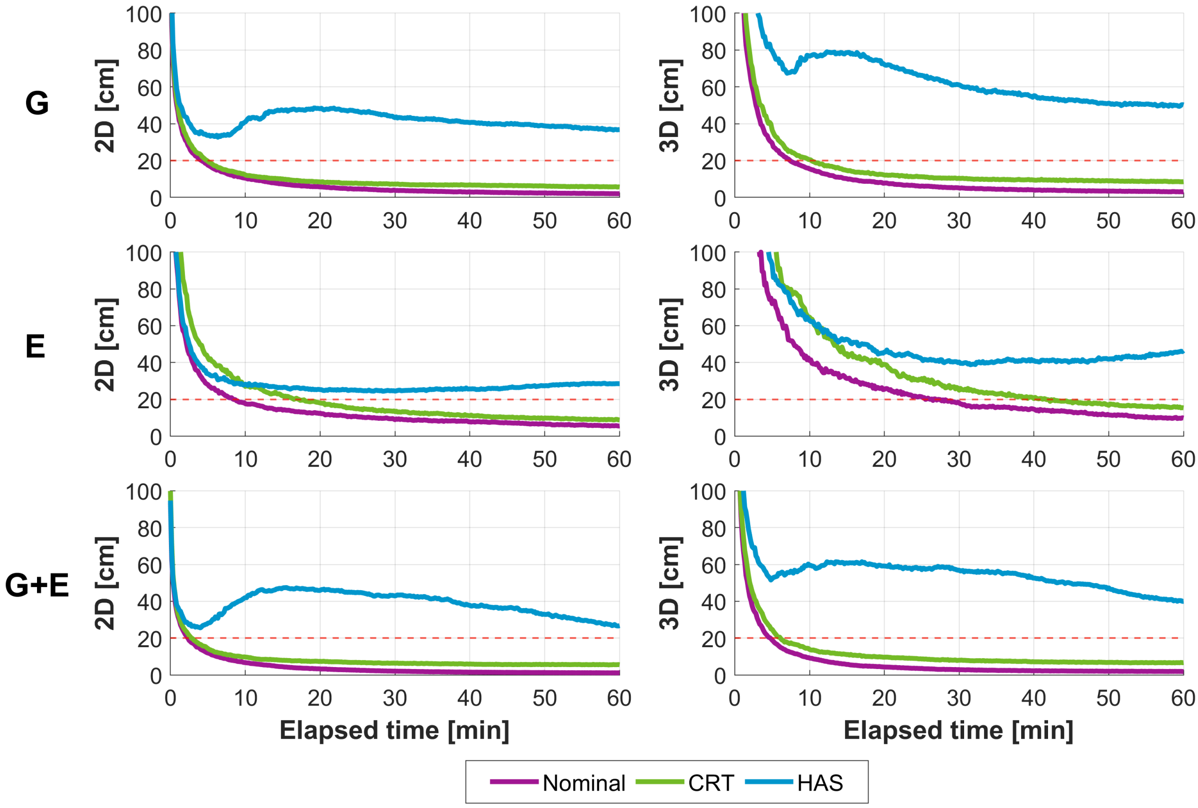

Figure 8.4: 2D and 3D convergence performance of a kinematic float-PPP user located at Redu, Belgium on DOY 121 in 2024, taken as the 90th percentile of 1261 windows of 60 minutes, each shifted by 1 minute from 01:00 to 23:00 on the selected day. These results are given for the various combinations of MEO GNSS products (Nominal (COD), CRT, HAS) and constellation combinations (G, E, G+E), where no LEO satellites have been considered as yet. The dashed red line indicates the convergence threshold set at 20 cm.

8.2. MEO GNSS & Single LEO Satellite (Sentinel-6A)

As mentioned in Section 7.3, first the case of using a single LEO satellite in addition to MEO GNSS for the selected kinematic float-PPP user is considered. This single LEO satellite is placed in exactly the same orbit as Sentinel-6A. The Sentinel-6A passes for the user located at Redu, Belgium on DOY 121 in 2024 are illustrated in Figure 8.5, along with the skyplot for the entire day. As expected from a single LEO satellite, the duration of a single pass (around 15 minutes) and the number of passes per day for a given user are quite limited, leading to a low expected impact of the single LEO satellite in addition to MEO GNSS. However, this analysis can show whether even a single LEO with less precise products can potentially disrupt the PPP performance as compared to only using MEO GNSS without LEO satellites.

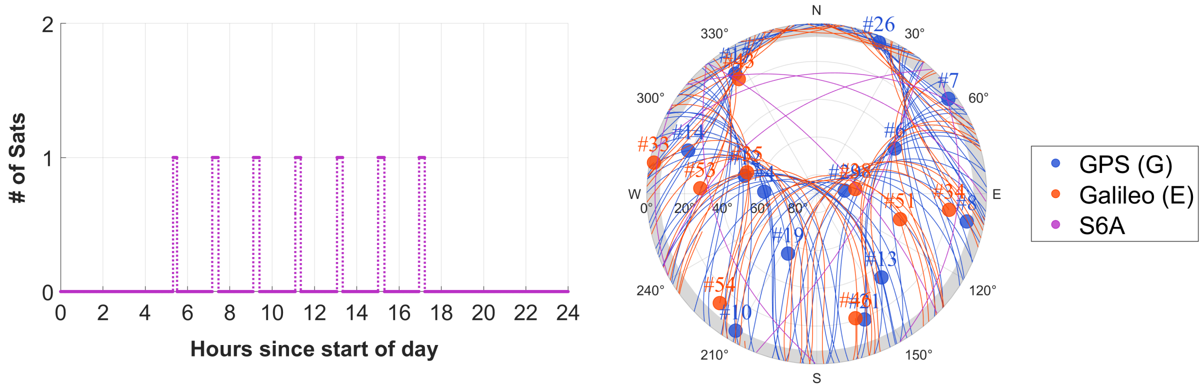

Figure 8.5: The epochs that Sentinel-6A is in view of the selected user at Redu, Belgium on DOY 121 in 2024 (left) and the corresponding skyplot for the entire day including Sentinel-6A, GPS, and Galileo satellites (right).

Since the impact of adding single LEO satellite was expected to be low, this single-LEO PPP analysis was limited to the cases in which only LEO satellite orbit errors and no LEO satellite clock errors were considered, as described in Section 7.3. The 3D convergence and positioning errors presented in Figure 8.6 and Figure 8.7 respectively show that the impact of a single LEO satellite is limited. Furthermore, the overlapping colored lines show that there is not much difference between the results using the various LEO products.

For brevity, the numerical results for the convergence time and accuracy following the metrics defined in Section 7.4 are only presented for the case of adding a LEO satellite with BRD-level orbit errors in Table 8.3 and Table 8.4 respectively. This case was chosen since it could be expected to have the largest negative impact (if any) out of the considered LEO products. A brief description of the main trends observed in the PPP results of MEO GNSS augmented by a single LEO satellite for each of the performance metrics are given below.

PPP Convergence Time

- **Nominal MEO GNSS (no errors):** While using MEO GNSS with no errors is not a realistic scenario, adding a single LEO satellite did not have a significant impact in 2D or 3D convergence time for any of these cases. This was valid for all of the considered LEO satellite orbit error levels.
- **MEO GNSS with CRT products:** The convergence time results for MEO GNSS with CRT products augmented by a single LEO satellite were similar to the Nominal MEO results. Namely, no significant difference in convergence time was observed for most of the cases. Only the case of Galileo-only with the LEO with BRD-level orbit errors had a degradation of around 12 minutes in 3D convergence time. As previously mentioned, the CRT GNSS products are missing 2 healthy Galileo satellites. These results indicate that a single LEO satellite with BRD-level orbit errors (and no LEO satellite clock errors) could result in a noticeable degradation of convergence time in the case of using a limited number of MEO GNSS satellites with CRT MEO GNSS products.

- **MEO GNSS with HAS products:** When using MEO GNSS with HAS products, none of the MEO GNSS-only cases achieved 3D convergence within the considered 60-minute windows. Furthermore, none of the cases with an additional single LEO satellite enabled 2D or 3D convergence time within 60 minutes at the 90th percentile. However, a small improvement in the overall convergence behavior could be noted for all of the LEO cases, as shown for GPS+Galileo as an example case in Figure 8.6. These results indicate that when using MEO GNSS with HAS products, even a single LEO satellite with BRD-level orbit errors (and no clock errors) can slightly reduce the convergence time, though still not achieving 20 cm 3D convergence within one hour.

Table 8.3: Convergence times to 20 cm in minutes (90th percentile) for a kinematic float-PPP user located at Redu, Belgium on DOY 121 in 2024 using **MEO GNSS augmented by a single LEO satellite**, with **only LEO satellite orbit errors and no LEO satellite clock errors**. An 'x' indicates that convergence was not achieved within the considered 60-minute windows.

		MEO: Nominal		MEO: CRT		MEO: HAS	
		2D	**3D**	**2D**	**3D**	**2D**	**3D**
MEO: G	No LEO	4.0	7.3	4.8	10.2	x	x
	LEO: BRD	4.0	7.5	4.7	10.0	x	x
MEO: E	No LEO	8.3	27.2	17.0	41.5	x	x
	LEO: BRD	8.7	26.8	15.8	53.7	x	x
MEO: G+E	No LEO	2.2	4.7	2.7	6.0	x	x
	LEO: BRD	2.2	4.5	2.8	6.2	x	x

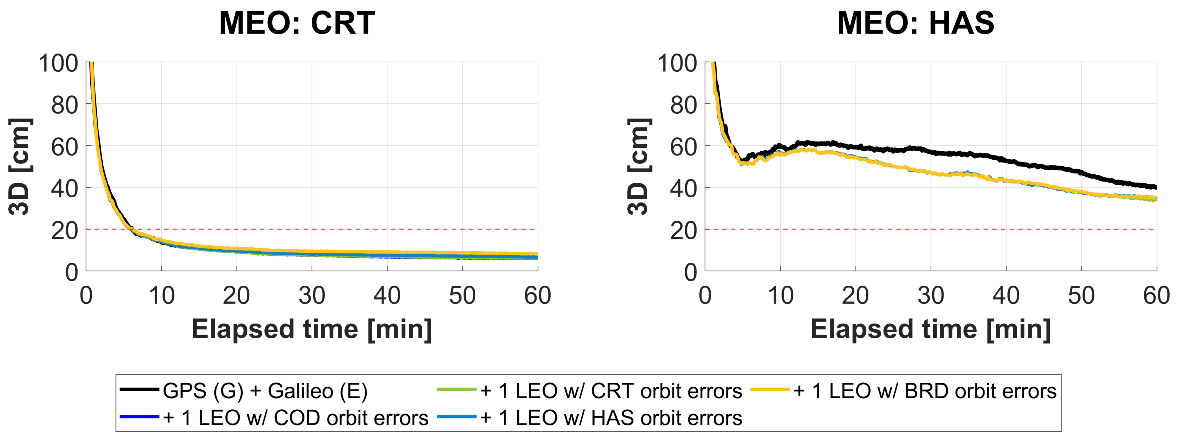

Figure 8.6: 2D and 3D convergence performance of a kinematic float-PPP user located at Redu, Belgium on DOY 121 in 2024, taken as the 90th percentile of 1261 windows of 60 minutes, each shifted by 1 minute from 01:00 to 23:00 on the selected day. The results are shown for the example case of **GPS+Galileo augmented by a single LEO satellite** with varying LEO satellite orbit error levels.

PPP Accuracy

- **Nominal MEO (no errors):** For the ideal case of perfect MEO GNSS orbits and clocks, adding a single LEO satellite with BRD-level orbit errors (and no LEO satellite clock errors), the single-GNSS constellation cases were degraded by up to 2-3 cm in 3D RMS, but only by up to 0.5 cm for GPS+Galileo. These results indicate that even a single LEO satellite could slightly degrade the Nominal MEO GNSS PPP accuracy, though it could be limited to only a few cm.
- **MEO with CRT products:** TThe PPP accuracy degradations for adding a single LEO satellite to MEO GNSS using CRT products were similar to but slightly lower than those for the Nominal GNSS products case. In this case, the worst 3D RMS degradation was around 1-2.5 cm when adding the LEO satellite with BRD-level orbit errors to single-GNSS. Therefore, the impact of a single LEO is still quite limited when using MEO GNSS with CRT products.

- **MEO with HAS products:** The single LEO satellite has a more noticeable impact for the case of using MEO GNSS with HAS products. Here, the positioning accuracy was improved by around 7 cm when adding a single LEO satellite to GPS-only, likely due to the lower quality and data gaps of the HAS GPS products. For Galileo-only and GPS+Galileo, this improvement was limited to 1 cm or less.

Table 8.4: RMS of the 2D and 3D positioning errors in cm computed from 02:00 to 23:00 on DOY 121 in 2024 for a kinematic float-PPP user located at Redu, Belgium using **MEO GNSS augmented by a single LEO satellite**, with **only LEO satellite orbit errors and no LEO satellite clock errors**.

		MEO: Nominal		MEO: CRT		MEO: HAS	
		2D	3D	2D	3D	2D	3D
MEO: G	No LEO	0.9	1.6	2.3	4.4	15.8	23.9
	LEO: BRD	1.9	3.3	3.0	5.6	9.7	16.7
MEO: E	No LEO	1.3	2.2	4.1	6.1	11.1	17.2
	LEO: BRD	3.8	5.3	6.2	8.7	10.4	17.0
MEO: G+E	No LEO	0.6	1.1	2.2	4.7	8.9	13.2
	LEO: BRD	0.9	1.6	2.4	4.9	7.4	12.3

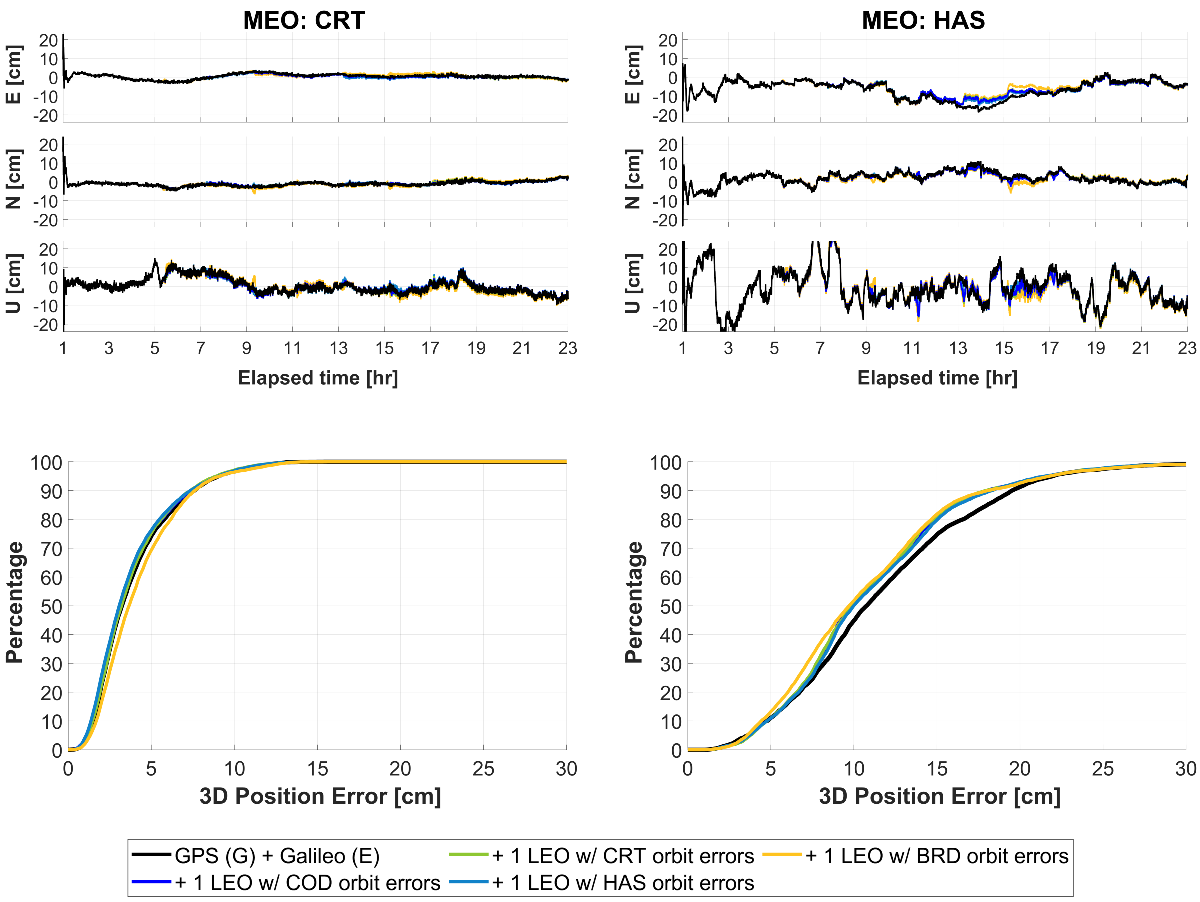

Figure 8.7: Positioning errors for a kinematic float-PPP user located at Redu, Belgium on DOY 121 in 2024, shown for the example case of **GPS+Galileo augmented by a single LEO satellite** with varying orbit error levels.

These results show a more limited improvement as compared to the real-world kinematic float-PPP results from the ESAT1 experiment by CentiSpace (Xu et al., 2024). They used the WUM final GNSS products for both the POD of ESAT1 and as the MEO GNSS products in the ground user PPP, neither of which are realistic for use in real-time PPP. Out of the cases considered in this thesis, MEO GNSS with CRT products and a LEO satellite with COD-level orbit errors would be the most similar. The additional LEO satellite had no noticeable impact on the convergence time or the positioning accuracy in this case. In turn, Xu et al. (2024) reported an average GPS+Galileo convergence time reduction from 8.6 to 6.6 minutes. However, their convergence criteria were set at 20 cm and 40 cm for the horizontal and vertical directions respectively. Their 3D RMS positioning error improvements were around 3-4 cm for the GPS-only/Galileo-only cases and 1 cm for the GPS+Galileo case. Their improved results are likely due to their statistics being based on only 23 windows where ESAT1 was tracked for at least 3 minutes. This is as opposed to the 1261 windows considered in this work, where there were only 7 LEO passes as shown in Figure 8.5, leading to the low expected impact of the single LEO satellite here. Furthermore, ESAT1 was situated at an altitude of 700 km and a different user location was considered, also leading to potential differences.

8.3. MEO GNSS + Simulated LEO Constellation

This section presents the PPP results for the cases of MEO GNSS augmented by a LEO constellation of 28 satellites. As described in Section 7.3, the considered LEO constellation consists of 7 planes of S6A-like orbits that are evenly spaced in the RAAN and have 4 satellites per plane. The number of LEO satellites in view of the selected user over the DOY 121 in 2024 is shown in Figure 8.8. With the selected LEO constellation configuration, 2.2 LEO satellites are in view on average and there is always at least 1 LEO satellite at any given epoch. Furthermore, the skyplots for the ground user are shown in Figure 8.9. The 1-hour skyplot particularly illustrates the more rapid passes of the LEO satellites as compared to the MEO ones.

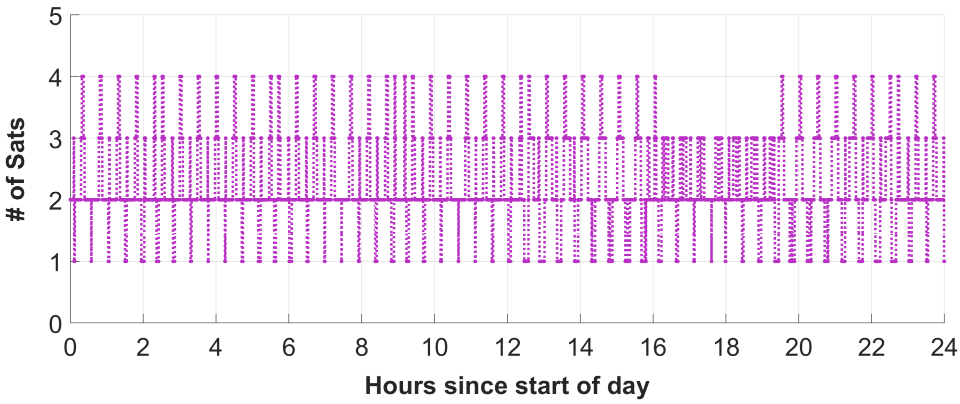

Figure 8.8: The number of LEO satellites from the simulated 28-satellite LEO constellation in view for the selected user at Redu, Belgium on DOY 121 in 2024.

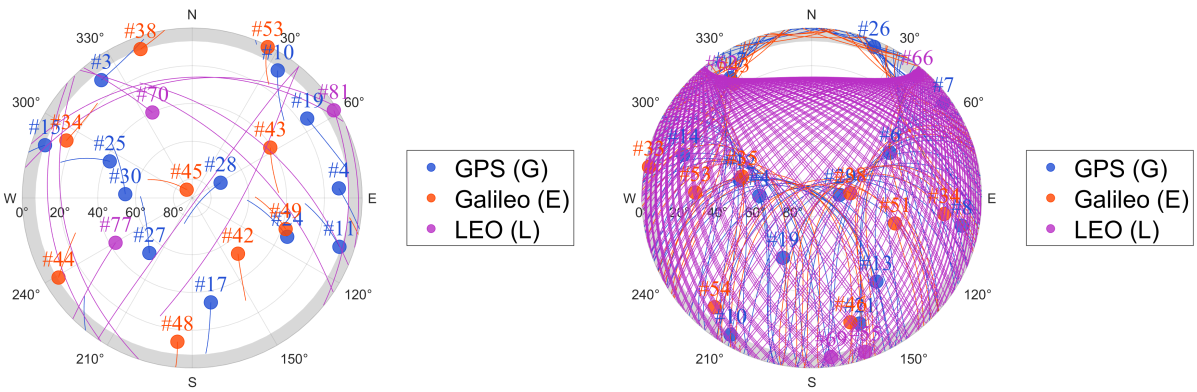

Figure 8.9: Skyplots of satellites in view of the selected user at Redu, Belgium for 1 hour from 08:00-09:00 (left) and 24 hours (right) on DOY 121 in 2024, including the satellites from GPS, Galileo, and the simulated LEO constellation of 28 satellites.

First, Section 8.3.1 presents the PPP results for the cases where only orbit errors and no clock errors from the on-board real-time POD have been considered for the LEO satellites. These results can be representative of the PPP performance that is achievable in the case that the LEO satellite clock corrections are (perfectly) estimated on ground, while the LEO satellite orbits are still estimated on-board. It should be noted that completely excluding the LEO satellite clock errors represents an ideal case, since in a real-world scenario the LEO satellite clocks estimated on ground would also have some level of error. Then, Section 8.3.2 presents the PPP results where both the on-board determined LEO satellite orbit and clock errors were considered.

8.3.1. MEO GNSS + Simulated LEO Constellation with Only LEO Satellite Orbit Errors & No LEO Satellite Clock Errors

This subsection presents the PPP results for the cases using MEO GNSS and a simulated LEO constellation of 28 satellites, where only orbit errors and no clock errors were considered for the LEO satellites. The 2D and 3D convergence time and accuracy results based on the metrics given in Section 7.4 are shown in Table 8.5 and Table 8.6 respectively, and the trends observed in these results are discussed under the corresponding headings below.

PPP Convergence Time

- **Nominal MEO GNSS (no errors):** When considering MEO GNSS with no orbit or clock errors, the LEO satellites with COD/CRT-level orbit errors provide a substantial reduction in convergence time for all three MEO GNSS cases. This is more pronounced for Galileo-only, since the convergence times using only MEO GNSS for GPS-only and GPS+Galileo are already quite short thanks to the higher number of satellites. These results indicate that even with perfect MEO GNSS orbits and clocks, a LEO constellation with COD/CRT-level orbit errors and no clock errors can still offer an improvement in convergence time when augmenting MEO GNSS.

  The LEO satellites with HAS-level orbit errors provide an improvement in 2D convergence time for all three MEO GNSS cases. In 3D, this improvement in convergence time is limited to the Galileo-only case. This indicates that a LEO constellation with HAS-level orbit errors might not always have a positive impact on the convergence time. Using LEO satellites with BRD-level orbit errors significantly increase both the 2D and 3D convergence times for all three MEO GNSS cases. This indicates that a LEO constellation with BRD-level orbit products, even with no clock errors, could degrade the convergence time as compared to using MEO GNSS alone.

- **MEO GNSS with CRT products:** The trends for the cases of using CRT GNSS products for the MEO satellite orbits and clocks are similar to those for the Nominal MEO satellite orbits and clocks. Here, the LEO satellites with COD/CRT-level orbit errors are also reduce the convergence time, with the most pronounced improvement being for Galileo-only going from 41.5 minutes to around 5.5-6 minutes to achieve 3D convergence. The convergence time improvements for GPS-only and GPS+Galileo are more moderate, reducing from approximately 10 to 4.5 minutes and 6 to 3.5 minutes respectively in 3D.

  Also similar to the Nominal MEO cases, the LEO satellites with HAS-level orbit errors improve the 2D convergence time, while in 3D this only happens when augmenting Galileo-only. Meanwhile, the LEO satellites with BRD-level orbit errors cause a degradation in convergence for all three of the MEO GNSS cases. These convergence behaviors are further illustrated by the example case of GPS+Galileo given in Figure 8.10. Here, the initial rapid convergence is present for all the LEO cases, though for the HAS-level and BRD-level LEO satellite orbit errors this rapid convergence stops sooner than for the MEO GNSS-only, leading to the delayed 3D convergence times.

- **MEO GNSS with HAS products:** As mentioned, the MEO GNSS-only cases with HAS products did not converge within 60 minutes. Once augmenting with LEO satellites, 2D convergence was achieved for all LEO satellite orbit error levels (assuming no clock errors) for the considered PPP user. The best 2D convergence times were obtained for GPS+Galileo, which is also shown as an example case in Figure 8.10, where even using LEO satellites with HAS-level orbit errors reached 2D convergence in less than 3 minutes. Even adding LEO satellites with BRD-level orbit errors to GPS-only resulted in 2D convergence in 22 minutes.

The LEO satellites with CRT-level orbit errors enabled 3D convergence within 13 minutes for each of the single and dual MEO GNSS cases. The LEO satellites with HAS-level orbit errors enabled 3D convergence for Galileo-only and GPS+Galileo at 16.7 and 18.3 minutes respectively, though for GPS-only 3D convergence was still not achieved within the 60 minutes, likely due to the gaps and lower accuracy of the HAS GPS products. The LEO satellites with BRD-level orbit errors also improve the 3D convergence performance, though only the GPS+Galileo case converges within one hour at 52 minutes.

Table 8.5: Convergence times to 20 cm in minutes (90th percentile) for a kinematic float-PPP user located at Redu, Belgium on DOY 121 in 2024 using **MEO GNSS augmented by a simulated LEO constellation of 28 satellites**, with **only LEO satellite orbit errors and no LEO satellite clock errors**. Improvements compared to MEO GNSS-only cases are shown in green, while degradations are shown in red. An 'x' indicates that convergence was not achieved within the considered 60-minute windows.

		MEO: Nominal		**MEO: CRT**		**MEO: HAS**	
		2D	**3D**	**2D**	**3D**	**2D**	**3D**
MEO: G	No LEO	4.0	7.3	4.8	10.2	x	x
	LEO: COD	1.8	3.7	1.8	4.2	5.3	12.2
	LEO: CRT	2.0	3.8	2.0	4.5	6.0	13.0
	LEO: HAS	2.2	8.2	2.5	10.0	9.8	x
	LEO: BRD	17.8	37.2	18.2	38.3	22.0	x
MEO: E	No LEO	8.3	27.2	17.0	41.5	x	x
	LEO: COD	2.3	5.0	2.7	5.7	2.8	6.7
	LEO: CRT	2.3	5.0	2.7	6.0	3.0	7.8
	LEO: HAS	3.3	13.7	4.0	13.8	4.5	16.7
	LEO: BRD	22.0	x	24.3	x	21.5	x
MEO: G+E	No LEO	2.2	4.7	2.7	6.0	x	x
	LEO: COD	1.2	2.8	1.3	3.2	1.8	9.5
	LEO: CRT	1.2	3.0	1.3	3.5	2.0	10.8
	LEO: HAS	1.5	4.7	1.5	6.8	2.7	18.3
	LEO: BRD	16.3	30.0	16.3	29.8	17.8	51.8

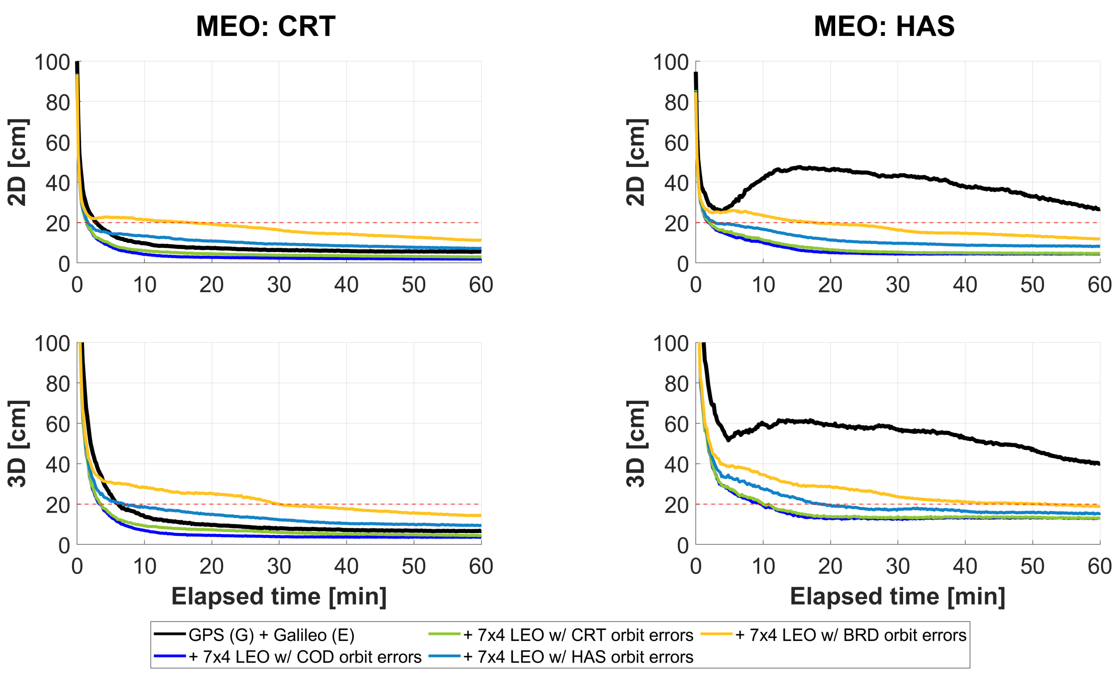

Figure 8.10: 2D and 3D convergence performance of a kinematic float-PPP user located at Redu, Belgium on DOY 121 in 2024, taken as the 90th percentile of 1261 windows of 60 minutes, each shifted by 1 minute from 01:00 to 23:00 on the selected day. The results are shown for the example case of **GPS+Galileo augmented by a simulated LEO constellation of 28 satellites** with **varying LEO satellite orbit error levels and no LEO satellite clock errors**.

PPP Accuracy

- **Nominal MEO GNSS (no errors):** For the Nominal MEO GNSS cases, almost all cases including LEO satellites resulted in a positioning accuracy degradation. This was even when using LEO satellites with CRT-level orbit errors, though this was only an increase of around 1 cm in the RMS positioning error. For the case of including LEO satellites with HAS and BRD-level orbit errors, the RMS positioning error is increased by around 1-5 cm and 2-9 cm respectively. These upper bounds are similar to the corresponding SISRE(orb) values presented in the POD results, which were 5.6 cm and 8.4 cm for the real-time POD using HAS and BRD products respectively. Overall, these results indicate that, as opposed to the convergence time results, even using CRT-level LEO satellite orbit products and considering perfect LEO satellite clocks lead to a positioning accuracy degradation.

- **MEO GNSS with CRT products:** Positioning errors of cm-level are achieved here for the PPP with only MEO GNSS with CRT products. The addition of LEO satellites with COD/CRT-level errors offer a small improvement of around 0.5-2 cm in 3D RMS error. Adding LEO satellites with HAS and BRD-level orbit errors increase the positioning error, which in the worst case was a 3D RMS error increase of 7.2 cm. These trends are illustrated in the 3D positioning error time series and cumulative distribution shown in Figure 8.11. For the example case of GPS+Galileo, adding the LEO constellation with COD/CRT-level orbit errors offers an improvement (both having 91% at 5 cm) as compared to GPS+Galileo alone (74% at 5 cm), while for HAS/BRD-level orbit errors this is not the case (72% and 54% at 5 cm respectively).

- **MEO GNSS with HAS products:** As previously presented, the 3D RMS positioning error for the MEO GNSS-only cases using HAS products are around 13-24 cm. Adding LEO satellites offered an accuracy improvement for all of the LEO satellite orbit error levels, achieving 3D RMS errors of around 7.5-15 cm instead. This improvement for all of the LEO satellite orbit error levels can also be noted from the cumulative 3D positioning errors shown in Figure 8.11 for the example case of GPS+Galileo, where all of the LEO cases had 88-94% at 15 cm as opposed to 75% for MEO GNSS alone. As previously mentioned, these improvements might be overly optimistic due to the data gaps in the HAS MEO GNSS products, in addition to the fact that LEO satellite clock errors are not considered here.

Table 8.6: RMS of the 2D and 3D positioning errors in cm computed from 02:00 to 23:00 on DOY 121 in 2024 for a kinematic float-PPP user located at Redu, Belgium using **MEO GNSS augmented by a simulated LEO constellation of 28 satellites**, where **only LEO satellite orbit errors and no LEO satellite clock errors** are considered. Improvements compared to MEO GNSS-only cases are shown in green, while degradations are shown in red.

		MEO: Nominal		**MEO: CRT**		**MEO: HAS**	
		2D	**3D**	**2D**	**3D**	**2D**	**3D**
MEO: G	No LEO	0.9	1.6	2.3	4.4	15.8	23.9
	LEO: COD	0.9	1.8	1.5	3.1	5.1	11.3
	LEO: CRT	1.4	2.6	1.8	3.4	5.3	11.5
	LEO: HAS	2.8	5.8	3.0	6.4	5.8	13.2
	LEO: BRD	4.4	7.8	4.8	8.6	7.6	14.8
MEO: E	No LEO	1.3	2.2	4.1	6.1	11.1	17.2
	LEO: COD	1.2	2.2	2.0	3.8	3.0	6.9
	LEO: CRT	1.9	3.5	2.5	4.6	3.3	7.4
	LEO: HAS	3.8	7.1	4.9	9.2	4.9	10.5
	LEO: BRD	6.5	11.1	7.7	13.3	7.1	12.3
MEO: G+E	No LEO	0.6	1.1	2.2	4.7	8.9	13.2
	LEO: COD	0.6	1.3	1.4	3.1	4.8	9.2
	LEO: CRT	1.0	1.8	1.6	3.2	4.9	9.2
	LEO: HAS	1.8	3.8	2.3	4.8	5.0	10.3
	LEO: BRD	2.9	5.5	3.4	6.3	6.0	10.5

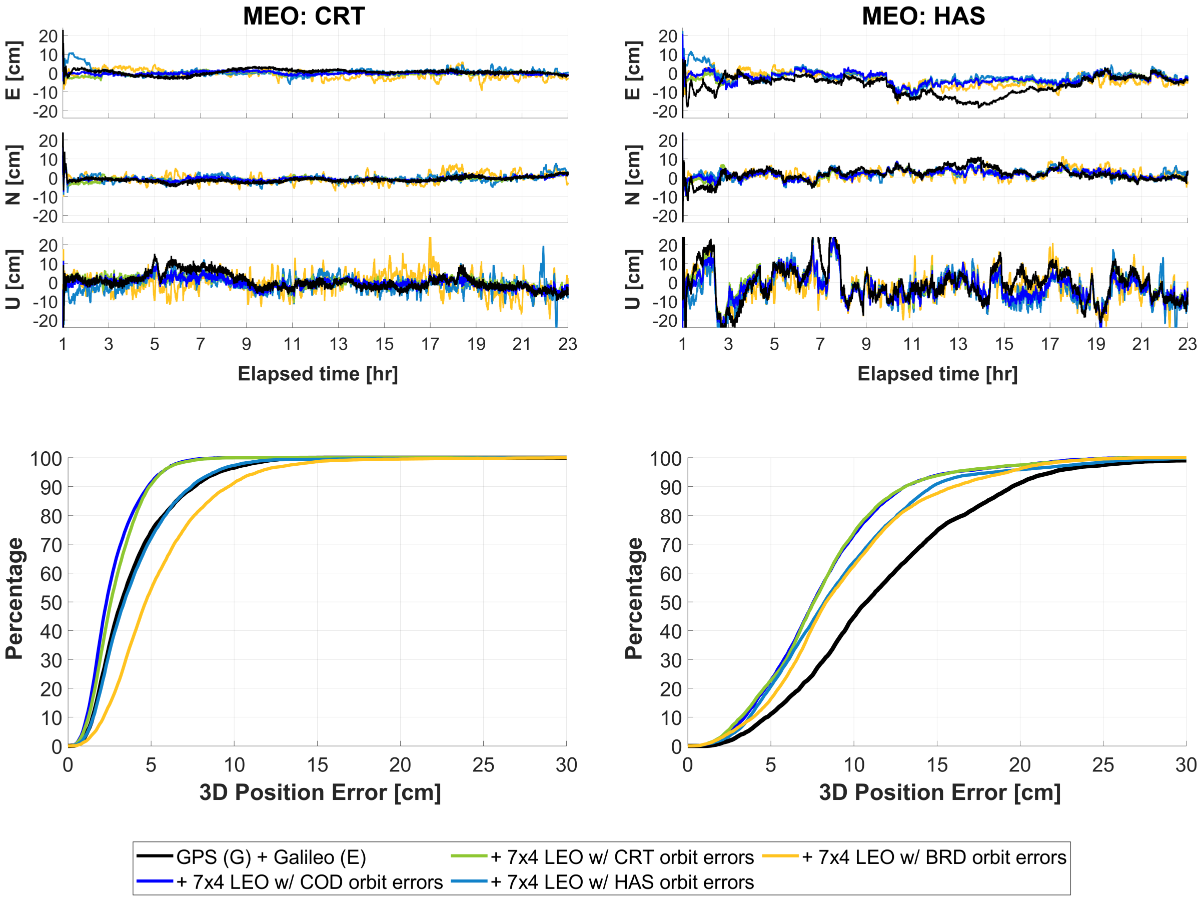

Figure 8.11: Time series (above) and cumulative distribution (below) of positioning errors for a kinematic float-PPP user located at Redu, Belgium on DOY 121 in 2024, shown for the example case of **GPS+Galileo augmented by a simulated LEO constellation of 28 satellites** with **varying LEO satellite orbit error levels and no LEO satellite clock errors**.

8.3.2. MEO GNSS + Simulated LEO Constellation with LEO Satellite Orbit & Clock Errors

This subsection presents the results of the PPP analysis conducted for the cases of augmenting MEO GNSS with a constellation of 28 LEO satellites, where both LEO satellite orbit and clock errors obtained from the on-board real-time POD results were included in the LEO constellation simulation. Only the LEO satellites with CRT-level and HAS-level orbit and clock errors were considered in this part. Similar to the previous subsection, the results for the 2D and 3D convergence time and positioning accuracy metrics as defined in Section 7.4 are presented in Table 8.7 and Table 8.8 and further discussed under the corresponding headings below.

PPP Convergence Time

- **Nominal MEO GNSS (no errors):** Adding LEO CRT-level clock errors in addition to the LEO satellite orbit errors still allowed for an improvement in convergence time as compared to Nominal MEO GNSS alone. When including LEO satellites with HAS-level orbit and clock, there is a noticeable degradation in both 2D and 3D convergence time for all single and dual-GNSS cases. While for the Galileo-only case this increase is limited to around 1 minute, for the GPS-only and GPS+Galileo the convergence times are around double and triple respectively.

- **MEO GNSS with CRT products:** Adding the LEO constellation with CRT-level orbit and clock errors consistently improve the convergence time as compared to MEO GNSS with CRT products alone. Furthermore, the additional LEO satellite CRT-level clock errors increase the convergence time by up to 1 minute as compared to using only CRT-level LEO satellite orbit errors and no clock errors. This indicates that including the relatively large CRT-level LEO satellite clock errors does not significantly degrade the PPP convergence time. Though, the reader should be reminded that this is within the limitations of the assumptions made for the on-board clock error analysis in this thesis, as discussed in Section 5.4.

The LEO satellites with only HAS-level orbit errors improved convergence time in almost all MEO GNSS cases with CRT products. Adding HAS-level LEO satellite clock errors only improved the convergence time for Galileo-only, though this was around double the convergence time when using only HAS-level LEO satellite orbit errors. Meanwhile, the convergence times for GPS-only and GPS-Galileo were significantly degraded, as illustrated for the latter case as an example in Figure 8.12. These results indicate that including the HAS-level LEO satellite clock errors estimated on-board can degrade the convergence time as compared to estimating the LEO satellite clocks from the ground, when considering a ground user of CRT MEO GNSS products.

- **MEO with HAS products:** As previously mentioned, the MEO GNSS-only cases using HAS GNSS products did not converge to 20 cm within the considered 60 minute windows for any of GPS-only, Galileo-only, or GPS+Galileo cases. Adding LEO satellites with both CRT-level orbit and clock errors enabled convergence in all three of the single and dual GNSS cases. These convergence times were not increased by more than 1 minute as compared to the corresponding cases with only LEO satellite orbit errors and perfect LEO satellite clocks.

  When using HAS-level LEO satellite orbit and clock errors, the LEO satellites enable convergence within the hour in almost all cases, only excluding the 3D convergence when augmenting GPS-only. The convergence times when including these HAS-level LEO satellite orbit and clock errors are degraded as compared to the cases including only LEO satellite orbit errors, but the degree to which this occurs is varying among the single and dual GNSS cases, as shown for the example case of GPS+Galileo in Figure 8.12. This varying degradation could be due to the data gaps in the HAS GPS products and the resulting MEO GNSS geometries for the selected user on the selected day.

Table 8.7: Convergence times to 20 cm in minutes (90th percentile) for a kinematic float-PPP user located at Redu, Belgium on DOY 121 in 2024 using **MEO GNSS augmented by a simulated LEO constellation of 28 satellites**, with **both LEO satellite orbit errors and LEO satellite clock errors**. Improvements compared to MEO GNSS-only cases are shown in green, while degradations are shown in red. An 'x' indicates that convergence was not achieved within the considered 60-minute windows.

		MEO: Nominal		MEO: CRT		MEO: HAS	
		2D	**3D**	**2D**	**3D**	**2D**	**3D**
MEO: G	No LEO	4.0	7.3	4.8	10.2	x	x
	LEO: CRT	2.0	4.0	2.2	4.7	6.0	13.5
	LEO: HAS	7.8	19.3	8.0	20.2	11.5	x
MEO: E	No LEO	8.3	27.2	17.0	41.5	x	x
	LEO: CRT	2.5	5.2	3.2	6.3	3.2	8.7
	LEO: HAS	8.5	28.5	8.7	30.0	10.3	33.5
MEO: G+E	No LEO	2.2	4.7	2.7	6.0	x	x
	LEO: CRT	1.2	3.2	1.3	3.7	2.0	11.0
	LEO: HAS	6.5	16.7	6.5	17.5	9.2	21.8

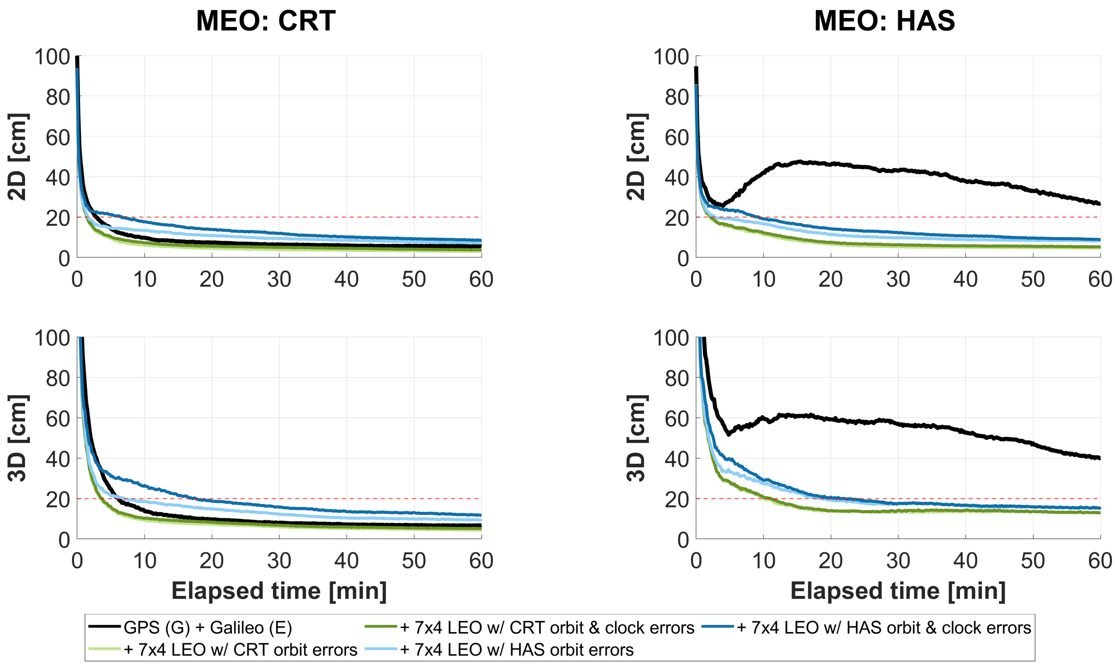

Figure 8.12: 2D and 3D convergence performance of a kinematic float-PPP user located at Redu, Belgium on DOY 121 in 2024, taken as the 90th percentile of 1261 windows of 60 minutes, each shifted by 1 minute from 01:00 to 23:00 on the selected day. The results are shown for the example case of **GPS+Galileo augmented by a simulated LEO constellation of 28 satellites** considering **varying LEO satellite orbit error levels with and without LEO satellite clock errors**.

PPP Accuracy

- **Nominal MEO GNSS (no errors):** Adding LEO satellites with CRT and HAS-level orbit and clock errors degraded the positioning accuracy for each of the Nominal MEO GNSS cases. Compared to the corresponding MEO GNSS-only cases, the positioning accuracy results were around 3 to 4 times worse, but overall the largest RMS positioning error was still less than 10 cm. These results indicate that though the LEO satellite orbit and clock errors can have a negative impact when considering perfect (error-free) MEO GNSS orbits and clocks, the severity of this impact can be limited.

- **MEO GNSS with CRT products:** Adding LEO satellites with CRT-level orbit and clock errors slightly improve the RMS positioning errors, though not by more than 1 cm as compared to MEO GNSS alone. This small improvement can also be noted from the cumulative error distribution shown in Figure 8.13 for the example case of GPS+Galileo, where for example the case of LEO with CRT-level orbit and clock errors has around 82% at 5 cm, while for MEO GNSS-only this is 74%.

  Adding LEO satellites with both HAS-level orbit and clock errors degraded the positioning accuracies. These errors were less than 1 cm larger than the corresponding cases where only LEO HAS-level orbit errors were considered, and overall the worst RMS positioning error is also not more than around 10 cm. Here, the cumulative error distribution of the HAS-level LEO satellite orbit and clock errors is at around 68% for 5 cm.

- **MEO GNSS with HAS products:** When using HAS products for MEO GNSS, adding LEO satellites with both CRT-level and HAS-level orbit and clock errors improve the positioning accuracy. This can be seen for the example case of GPS+Galileo in Figure 8.13, where all of the LEO cases have around 90-94% at 15 cm in the cumulative error distribution, while for MEO GNSS-only this is only 75% at 15 cm. Compared to the corresponding cases where only LEO satellite orbit errors were considered, the LEO satellite clock errors did not degrade the positioning accuracy by more than 1 cm.

Table 8.8: RMS of the 2D and 3D positioning errors in cm computed from 02:00 to 23:00 on DOY 121 in 2024 for a kinematic float-PPP user located at Redu, Belgium using **MEO GNSS augmented by a simulated LEO constellation of 28 satellites**, with **both LEO satellite orbit errors and LEO satellite clock errors** are considered. Improvements compared to MEO GNSS-only cases are shown in green, while degradations are shown in red.

		MEO: Nominal		MEO: CRT		MEO: HAS	
		2D	3D	2D	3D	2D	3D
MEO: G	No LEO	0.9	1.6	2.3	4.4	15.8	23.9
	LEO: CRT	1.8	3.4	2.2	4.1	5.1	12.0
	LEO: HAS	3.3	6.4	3.5	7.0	6.0	13.1
MEO: E	No LEO	1.3	2.2	4.1	6.1	11.1	17.2
	LEO: CRT	2.5	4.5	2.9	5.2	3.7	7.9
	LEO: HAS	4.6	8.2	6.2	10.3	5.7	11.5
MEO: G+E	No LEO	0.6	1.1	2.2	4.7	8.9	13.2
	LEO: CRT	1.4	2.5	1.9	3.8	4.9	9.2
	LEO: HAS	2.1	4.2	2.6	5.2	5.1	10.4

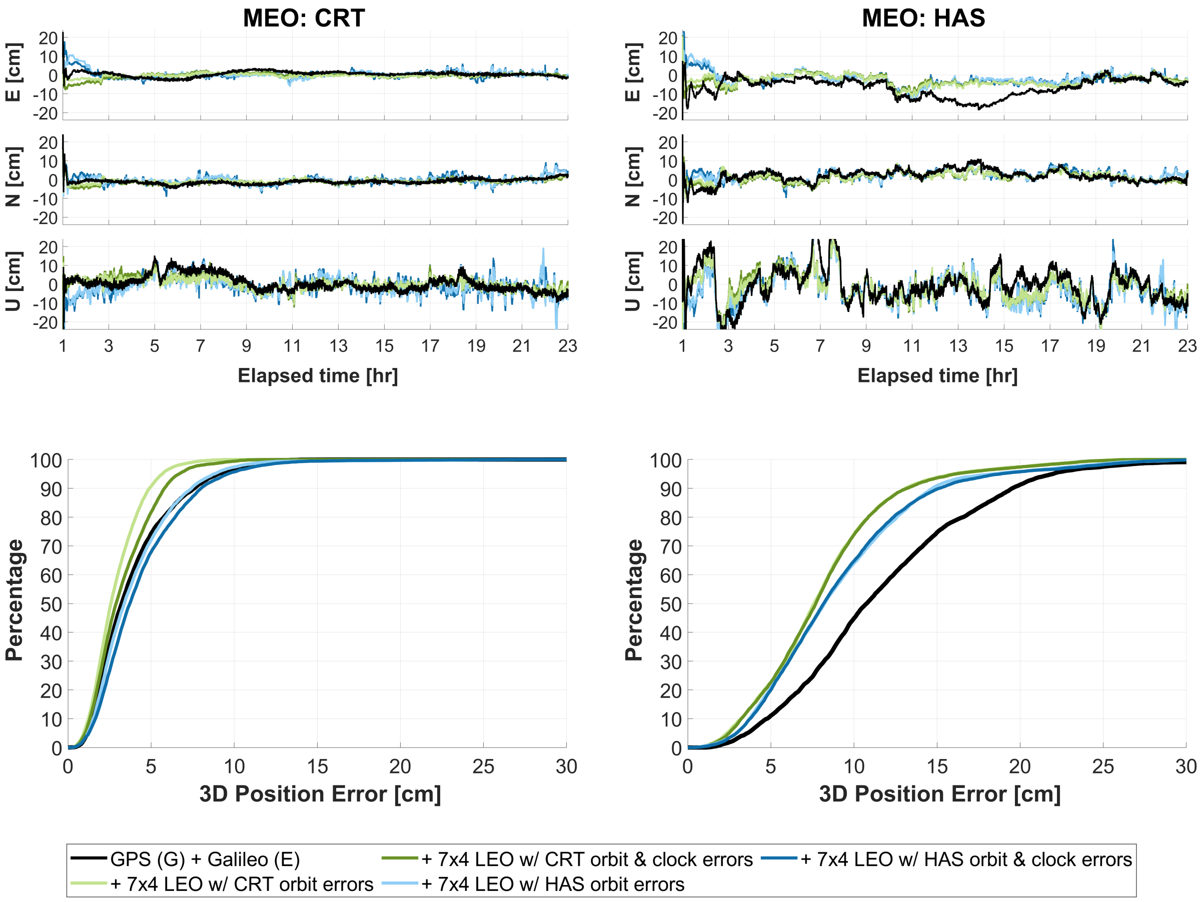

Figure 8.13: Time series (above) and cumulative distribution (below) of positioning errors for a kinematic float-PPP user located at Redu, Belgium on DOY 121 in 2024, shown for the example case of **GPS+Galileo augmented by a simulated LEO constellation of 28 satellites** with **varying LEO satellite orbit error levels and no LEO satellite clock errors**.

9 Conclusion & Recommendations

The objective of this thesis has been to quantify the impact that LEO-PNT satellite orbit and clock errors determined with on-board real-time precise orbit determination would have on user positioning. Several research questions were formulated to address this objective, which are listed below and can be answered as follows.

1. What orbit and clock accuracies can be expected from on-board POD for LEO-PNT satellites?

This question was addressed by performing real-time GNSS-based POD using real-world data. The reduced-dynamic orbit determination method using extended Kalman filter processing was identified as a suitable POD approach. Furthermore, simplified dynamical models were used to emulate the potential limited on-board computational power and to reduce the computation latency. Using the GHOST POD tool developed by DLR, the performance of this POD method for LEO satellites was investigated using dual-constellation GPS and Galileo measurements from DOY 118-124 in 2024 from the Sentinel-6A (S6A) mission. Four types of GNSS products were used to investigate the impact that these products would have on the achievable POD accuracy. These were the broadcast ephemerides (BRD), the Galileo High Accuracy Service corrections (HAS), the CNES Real-Time products (CRT), and the CODE MGEX final products (COD). Here, the BRD and HAS products are representative of what is currently available to LEO satellites in real-time. In turn, the CRT products illustrate what could potentially be achievable if these real-time GNSS corrections could be uplinked to the LEO satellites. Lastly, the COD products were used as a reference for the best achievable performance with the given POD method, though these are not available in real-time to begin with.

The 7-day POD results in this study showed 3D RMS orbit errors as compared to the reference Sentinel-6A orbits of around 2.8 cm, 4.8 cm, 9.9 cm, and 14.5 cm for the POD using COD, CRT, HAS, and BRD products respectively. These results are in line with the expectations from using the degraded dynamical setup as compared to the state-of-the-art real-time on-board POD results reported in literature (Montenbruck et al., 2022), (Hauschild et al., 2022), (Darugna et al., 2022). As no reference Sentinel-6A clock offsets were available, non-degraded batch processing was used to obtain a reference clock solution. The errors of the real-time estimated Sentinel-6A receiver clock offsets had standard deviations of 9.9 cm, 10.7 cm, 15.9 cm, and 21.6 cm for the POD using COD, CRT, HAS, and BRD products respectively. These clock error results were larger than expected, as compared to the corresponding orbit error results. This could in part be due to the fact that no specific setting tuning was performed for the clock error results, as well as the limitations of this analysis effectively being a comparison between two processing methods rather than an independent solution. However, similar approach was adopted by Kunzi and Montenbruck (2022), who also achieved similar clock error levels for real-time POD using the BRD products. The global average Signal-In-Space Ranging Errors (SISRE) is a metric used to quantify the contribution of a navigation satellite's orbit and clock errors on user positioning performance. The SISRE results based on the real-time Sentinel-6A orbit and clock errors were around 10 cm, 12 cm, 17 cm, and 25 cm for the POD using the COD, CRT, HAS, and BRD products respectively.

2. What user positioning performances can be expected when using LEO-PNT in addition to MEO GNSS?

This question was addressed by using the LEO satellite orbit and clock error results obtained in the POD part to assess their impact on the PPP convergence time and positioning accuracy for a user of MEO GNSS augmented by LEO-PNT satellites. For this study, an in-house end-to-end PPP simulator named LEOPARD was used, which can generate synthetic observations based on a defined space segment and user segment, and subsequently use these measurements to perform PPP. The selected scenario was kinematic float-PPP for a ground user located approximately at Redu in Belgium (5° longitude, 50° latitude, 370 m height) for the period of 01:00 to 23:00 on DOY 121 in 2024. For the MEO space segment, the single and dual GNSS cases of GPS and Galileo were considered. The COD, CRT, and HAS GNSS products were used for the MEO space segment orbit and clock errors, where the COD products were taken as the nominal (no error) values. For the LEO space segment, two scenarios were analyzed: a single LEO satellite in exactly the Sentinel-6A orbit, and a LEO constellation of 28 satellites in 7 S6A-like orbital planes evenly spaced in RAAN with 4 satellites per plane. The results from the POD part were used for the LEO satellite orbit and clock error levels, namely those obtained from on-board real-time POD using COD, CRT, HAS, and BRD products respectively. The use of two frequencies was considered for both the MEO and LEO space segments, namely L1 and L2 for GPS, and E1 and E5a for both Galileo and the LEO satellites.

First, the PPP performance when using MEO GNSS only was assessed to serve as a baseline for the results including the LEO satellites. As mentioned, the PPP performance was assessed through the convergence time and the positioning accuracy. The 3D RMS positioning accuracy obtained by the selected kinematic float-PPP user on the selected day from 02:00 to 23:00 with only GPS+Galileo was 4.7 cm and 13.2 cm when using the CRT and HAS GNSS products respectively, which were in line with literature on kinematic float-PPP using these products and real-world measurements (Gao et al., 2023), (Du et al., 2022), (Gao et al., 2025). The kinematic float-PPP convergence performance was statistically assessed by taking the 90th percentile of 1261 windows of 60 minutes, each shifted by 1 minute from 01:00 to 23:00 on the selected day. The 3D convergence time with only GPS+Galileo was 6.0 minutes when using the CRT products, while with the HAS products this convergence was not achieved within 60 minutes. These convergence results with CRT products were in line with the expectations from literature (Gao et al., 2023). In turn, these convergence results with HAS products are pessimistic as compared to literature (Gao et al., 2025), likely due to the data gaps in the HAS products.

Next, the impact of the additional LEO satellites on the user PPP performance was assessed. A single LEO satellite was found to have a marginal impact on the PPP performance, leading to the focus on the results when adding the simulated LEO constellation. These results are reported in three steps, namely for the user positioning performances when augmenting MEO GNSS with LEO satellites that have used BRD, HAS, and CRT products for the on-board real-time POD. For all three, the scenario of only including the LEO satellite orbit errors and no LEO clock errors were considered. This represents the ideal case where the LEO satellite clock errors are (perfectly) estimated on ground. For the latter two steps, the addition of the on-board estimated LEO satellite clock errors were also considered. Overall, the impact of the LEO constellation depended on which MEO GNSS constellations were used, as well as the quality of the MEO GNSS products that were used.

- **LEO-augmented PPP performance currently achievable:** The simulated LEO constellation using on-board real-time POD with BRD products represents what is currently readily achievable. Considering only BRD-level LEO satellite orbit errors and no LEO satellite clock errors resulted in a significant degradation of the PPP convergence time and RMS positioning errors for both the single and dual GNSS constellations with CRT products. For example, in the case of GPS+Galileo with CRT products the 3D convergence time increased from 6.0 to 29.8 minutes and the 3D RMS error from 4.7 to 6.3 cm. However, using GPS+Galileo with HAS products with LEO satellites with only BRD-level orbit errors and no LEO satellite clock errors resulted in improved convergence times and positioning accuracies, achieving 3D convergence in 52 minutes and improving the 3D RMS error from 13.2 cm to 10.5 cm.

- **LEO-augmented PPP performance achievable in the near term:** The simulated LEO constellation using on-board real-time POD with HAS products represents what is achievable in the near term. Considering HAS-level LEO satellite orbit errors and no LEO satellite clock errors did not significantly impact the convergence time when using MEO GNSS with CRT products. However, the 3D positioning accuracy was degraded by 2-3 cm for the single GNSS constellations, while for the dual GNSS case with CRT products there was no impact on the accuracy. In turn, once HAS-level LEO satellite clock errors were added, the GPS+Galileo 3D convergence time degraded to 17.5 minutes, and the 3D RMS error increased by 0.5 cm. For MEO GNSS with HAS products, the LEO constellation with HAS-level orbit errors and no clock errors also provided an improvement in convergence time and positioning accuracy, achieving 3D convergence to 20 cm in 18.3 minutes and a 3D RMS error of 10.3 cm for the GPS+Galileo case. Once HAS-level LEO satellite clock errors were also considered, 3D convergence for the GPS+Galileo case is still achieved in 21.3 minutes, along with a 3D RMS error of 10.4 cm.

- **LEO-augmented PPP performance achievable in the future:** The simulated LEO constellation using on-board real-time POD with CRT products represents what could potentially be achievable in the future. The LEO constellation with CRT-level errors was found to provide improvements in both convergence time and positioning accuracy to each of the single and dual GNSS cases, even when both on-board LEO satellite orbit and clock errors were considered. For example, when using GPS+Galileo with CRT products, the LEO constellation with both CRT-level orbit and clock errors resulted in an improved 3D convergence time from 6.0 minutes to 3.7 minutes and a 3D RMS error improvement from 4.7 cm to 3.8 cm. For GPS+Galileo with HAS products, these went from not converging within 60 minutes to 3D convergence in 11 minutes, and a 3D RMS error improvement from 13.2 cm to 9.2 cm.

In conclusion, for the investigated LEO constellation of 28 satellites augmenting MEO GNSS, using on-board real-time LEO POD with CRT products was found to improve the PPP performance for both the considered CRT and HAS ground user. Using on-board real-time LEO POD with HAS products only improved the PPP performance of the considered HAS ground user, and degraded (when including LEO satellite clock errors) or had no significant impact (when excluding LEO satellite clock errors) on the PPP performance of the considered CRT ground user. Finally, using on-board real-time LEO POD with BRD products resulted in small improvements for the considered HAS ground user and degradations for the considered CRT ground user, both without considering any LEO satellite clock errors. These conclusions are drawn within the limitations of this simulation study, where further improvements to better align the results with real-world conditions are suggested below.

Recommendations for Future Work

The following recommendations can be made for future works that could build up on the results that have been obtained and frameworks that have been used in this thesis, also taking inspiration from the needs and challenges identified in other related literature.

- **LEO product latency, prediction, and format:** The LEO satellite orbits and clocks determined on-board will still have a latency both in being computed and in being transmitted to the user. The effects of this latency on the positioning performance of the user could also be investigated. Furthermore, different strategies could be used to reduce the impact of this, such as short-term orbit predictions, which could also be explored in terms of their accuracy. Finally, the format in which the LEO corrections are provided could also have an impact on the PPP performance, namely whether interpolation needs to be done by the user, which is also a topic that could be looked into.

- **More extensive user segment analysis:** In this study, only one user was considered. To characterize global performance, a range of users across latitudes could be considered, especially since it was seen in literature that users at lower latitudes usually benefit less from satellites with higher inclinations as compared to users at high latitudes. Considering a range of users would provide a more complete understanding of the performances that can be expected from including a LEO constellation. Furthermore, the scenarios of data gaps for the LEO satellites due to outages or obstructed views could also be considered, to further assess the benefit of such a constellation in these conditions.

- **LEO space segment configurations:** Due to the limited data period of the HAS data available for this study, this had an impact on the size of LEO constellation that could be simulated. As the framework for conducting the POD, setting up the LEO space segment, and running the PPP simulations has been defined in this thesis, this could easily be extended if more data were available. Furthermore, data from other reference LEO satellites at different altitudes could also be used within the framework given in this thesis. In this way, the PPP performance of proposed LEO-PNT constellation configurations consisting of more satellites and potentially satellites at different altitudes can be assessed. Lastly, the choice of frequencies transmitted by the LEO satellites could also be tailored to other cases of interest.

- **LEO transmitter biases:** As mentioned in this thesis, the LEO satellite clock that is estimated in the on-board POD is the LEO *receiver* clock offset, while a LEO-PNT ground user would need the LEO *transmitter* clock offset. These two clock offsets will have different hardware delays, especially if the LEO-PNT satellites are transmitting at different frequencies as compared to those from GNSS. Furthermore, the transmitter biases can only be estimated by actually receiving the LEO-PNT signals. The impact of these LEO transmitter biases on PPP performance is also a topic that should be studied.

- **Multipath & cycle slips:** Effects such as multipath and cycle slip were not included in the PPP observation generation in this study, which is also causing a gap with the situation that would be faced in reality. The impact of these effects on the LEO-augmented PPP performance could therefore also be considered in future studies.

- **HAS data quality:** As covered in this thesis, the provided HAS data set had a fair amount of data gaps in both the GNSS orbit and clock products. Although these gaps can very well be consistent with the service provided in reality, the gaps naturally have an impact on the achieved results. This is more so for the PPP, since in the POD the reduced-dynamic approach can account for the gaps. Furthermore, as mentioned, improved results could also be obtained if the higher sampling rates for HAS, namely the 50 seconds for orbits and 10 seconds for clocks could be used instead of the respective 5 minutes and 30 seconds. The impact of HAS data gaps and sampling rates could therefore also be further investigated.

- **Impact of LEO-PNT on PPP-AR:** As mentioned in Chapter 7, the LEOPARD tool used for the PPP simulations in this thesis can also perform PPP-AR. Therefore, investigating the impact of LEO-PNT on PPP-AR could also readily be done with the setup described in this thesis, as well as for future cases considering the recommendations mentioned above.

References

Anderson, P. (2023). “TrustPoint System/Service Overview”. In: *International Committee on GNSS, Workshop on Low Earth Orbit (LEO) PNT Systems*.

Böhm, J., Möller, G., Schindelegger, M., Pain, G., and Weber, R. (2015). “Development of an improved empirical model for slant delays in the troposphere (GPT2w)”. In: *GPS Solutions* 19.3, pp. 433–441. DOI: 10.1007/s10291-014-0403-7.

Calliess, D., Montenbruck, O., Wermuth, M., and Reichinger, H. (2024). “Long-term analysis of Sentinel-6A orbit determination: Insights from three years of flight data”. In: *Advances in Space Research* 74.7, pp. 3011–3027. DOI: https://doi.org/10.1016/j.asr.2024.06.043.

Chen, B., Wang, K., El-Mowafy, A., and Yang, X. (2024). “Real-Time GNSS Satellite SISRE and its Integrity for LEO Satellite Precise Orbit Determination”. In: *Proceedings of the 2024 International Technical Meeting of The Institute of Navigation*. Long Beach, California, pp. 807–820. DOI: 10.33012/2024.19488.

Conrad, A., Axelrad, P., Desai, S., and Haines, B. (2024). “Sentinel-6 Michael Freilich precise orbit determination using PODRIX and TriG receiver measurements”. In: *Journal of Geodesy* 98.5, p. 39. DOI: 10.1007/s00190-024-01842-5.

Cordero, M., Giordano, P., Sarnadas, R., Grec, F.-C., Anghileri, M., and Prieto-Cerdeira, R. (2025). *An Overview of ESA’s LEO-PNT In Orbit Demonstration Mission*. Presented at the 2025 International Technical Meeting of The Institute of Navigation (ION ITM). Session A1: Alternatives, Backups, Complements to GNSS. Long Beach, CA.

Cullen, R., Giulicchi, L., Vuilleumier, P., and Levrini, G. (2021). *Sentinel-6 Precise Orbit Context*. Tech. rep. JC-TN-ESA-SY-0420-S6-POD-Context-1.5. Version Issue 1 Rev 5. ESA UNCLASSIFIED – Releasable to the public. Noordwijk, The Netherlands: European Space Research and Technology Centre (ESA).

Dach, R., Schaer, S., Arnold, D., Brockmann, E., Kalarus, M. S., Lasser, M., Stebler, P., and Jäggi, A. (2024). *CODE product series for the IGS MGEX project*. Tech. rep. Astronomical Institute, University of Bern. DOI: 10.48350/197028.

Darugna, F., Casotto, S., Bardella, M., Sciarratta, M., and Zoccarato, P. (2022). “Sub-Decimeter Onboard Orbit Determination of LEO Satellites Using SSR Corrections: A Galileo-Based Case Study for the Sentinel-6A Satellite”. In: *Remote Sensing* 14.23. Open access under the terms of the Creative Commons Attribution License (CC BY)., p. 6121. DOI: 10.3390/rs14236121.

Donlon, C. J. et al. (2021). “The Copernicus Sentinel-6 mission: Enhanced continuity of satellite sea level measurements from space”. In: *Remote Sensing of Environment* 258, p. 112395. DOI: https://doi.org/10.1016/j.rse.2021.112395.

Du, S., Shu, B., Xie, W., Huang, G., Ge, Y., and Li, P. (2022). “Evaluation of Real-time Precise Point Positioning with Ambiguity Resolution Based on Multi-GNSS OSB Products from CNES”. In: *Remote Sensing* 14.19. DOI: 10.3390/rs14194970.

European Commission, D.-G. D. I. and Space (2023). *Galileo Service Notice #13: Galileo High Accuracy Service (HAS) – Initial Service Declaration*. Tech. rep. 2023002. Version 1.0. EU Satellite Navigation Programmes.

European Union (2022). *Galileo High Accuracy Service Signal-In-Space Interface Control Document (HAS SIS ICD)*. Tech. rep. Issue 1.0. European Union.

Fernández, J. et al. (2024). "The Copernicus POD Service". In: *Advances in Space Research*. DOI: 10.1016/j.asr.2024.02.056.

FrontierSI (2024). *State of the Market Report: Low Earth Orbit Positioning Navigation and Timing – 2024 Edition*. Tech. rep. Version 1.1, January 25, 2025. FrontierSI.

Gao, M., Meng, Z., Zhu, H., Liu, T., Xu, A., Tan, C., and Cao, Z. (2025). "Evaluation of the Galileo high-accuracy service SSR product quality and PPP performance". In: *Advances in Space Research* 75.3, pp. 2669–2682. DOI: https://doi.org/10.1016/j.asr.2024.11.021.

Gao, M., Meng, Z., Zhu, H., Xu, A., Cao, Z., and Tan, C. (2023). "Research on the Real-Time Ambiguity Resolution Algorithm of GPS/Galileo/BDS Based on CNES Real-Time Products". In: *Remote Sensing* 15.21. DOI: 10.3390/rs15215159.

Ge, H., Li, B., Ge, M., Nie, L., and Schuh, H. (2020a). "Improving Low Earth Orbit (LEO) Prediction with Accelerometer Data". In: *Remote Sensing* 12.10. DOI: 10.3390/rs12101599.

Ge, H., Li, B., Ge, M., Zang, N., Nie, L., Shen, Y., and Schuh, H. (2018). "Initial Assessment of Precise Point Positioning with LEO Enhanced Global Navigation Satellite Systems (LeGNSS)". In: *Remote Sensing* 10.7, p. 984. DOI: 10.3390/rs10070984.

Ge, H., Li, B., Nie, L., Ge, M., and Schuh, H. (2020b). "LEO constellation optimization for LEO enhanced global navigation satellite system (LeGNSS)". In: *Advances in Space Research* 66.3, pp. 520–532. DOI: 10.1016/j.asr.2020.04.031.

Hauschild, A. and Montenbruck, O. (2021). "Precise real-time navigation of LEO satellites using GNSS broadcast ephemerides". In: *NAVIGATION* 68.2, pp. 419–432. DOI: 10.1002/navi.416.

Hauschild, A., Montenbruck, O., Steigenberger, P., Martini, I., and Fernandez-Hernandez, I. (2022). "Orbit determination of Sentinel-6A using the Galileo high accuracy service test signal". In: *GPS Solutions* 26.4, p. 120. DOI: 10.1007/s10291-022-01312-5.

Helleputte, T. V. (2004). *GHOST Technical Manual: GPS High Precision Orbit Determination Software Tools*. DLR.

Hong, J., Tu, R., Zhang, P., Zhang, R., Han, J., Fan, L., Wang, S., and Lu, X. (2023). "GNSS rapid precise point positioning enhanced by low Earth orbit satellites". In: *Satellite Navigation* 4.1, p. 11. DOI: 10.1186/s43020-023-00100-x.

Jacchia, L. G. (1971). *Revised Static Models of the Thermosphere and Exosphere with Empirical Temperature Profiles*. Special Report 332. Cambridge, MA: Smithsonian Astrophysical Observatory (SAO).

Kazmierski, K., Zajdel, R., and Sośnica, K. (2020). "Evolution of orbit and clock quality for real-time multi-GNSS solutions". In: *GPS Solutions* 24, p. 111. DOI: 10.1007/s10291-020-01026-6.

Kunzi, F., Braun, B., Markgraf, M., and Montenbruck, O. (2023). "A GNSS-Synchronized Satellite Navigation Payload for LEO PNT". In: 36th International Technical Meeting of the Satellite Division of The Institute of Navigation (ION GNSS+ 2023). Denver, Colorado, pp. 1425–1435. DOI: 10.33012/2023.19322.

Kunzi, F. and Montenbruck, O. (2022). "Precise Onboard Time Synchronization for LEO Satellites". In: *NAVIGATION: Journal of the Institute of Navigation* 69.3. DOI: 10.33012/navi.531. eprint: https://navi.ion.org/content/69/3/navi.531.full.pdf.

Laurichesse, D. (2011). “The CNES Real-time PPP with undifferenced integer ambiguity resolution demonstrator”. In: *Proceedings of the ION GNSS 2011*. Portland, Oregon.

Li, B., Ge, H., Bu, Y., Zheng, Y., and Yuan, L. (2022). “Comprehensive assessment of real-time precise products from IGS analysis centers”. In: *Satellite Navigation* 3.1, p. 12. DOI: 10.1186/s43020-022-00074-2.

Li, B., Ge, H., Ge, M., Nie, L., Shen, Y., and Schuh, H. (2019a). “LEO enhanced Global Navigation Satellite System (LeGNSS) for real-time precise positioning services”. In: *Advances in Space Research* 63.1, pp. 73–93. DOI: 10.1016/j.asr.2018.08.017.

Li, Q., Yao, W., Tu, R., Du, Y., and Liu, M. (2023). “Performance Assessment of Multi-GNSS PPP Ambiguity Resolution with LEO-Augmentation”. In: *Remote Sensing* 15.12, p. 2958. DOI: 10.3390/rs15122958.

Li, W., Yang, Q., Du, X., Li, M., Zhao, Q., Yang, L., Qin, Y., Chang, C., Wang, Y., and Qin, G. (2024). “LEO augmented precise point positioning using real observations from two CENTISPACE™ experimental satellites”. In: *GPS Solutions* 28.1, p. 44. DOI: 10.1007/s10291-023-01589-0.

Li, X., Li, X., Ma, F., Yuan, Y., Zhang, K., Zhou, F., and Zhang, X. (2019b). “Improved PPP Ambiguity Resolution with the Assistance of Multiple LEO Constellations and Signals”. In: *Remote Sensing* 11.4, p. 408. DOI: 10.3390/rs11040408.

Li, X., Ma, F., Li, X., Lv, H., Bian, L., Jiang, Z., and Zhang, X. (2019c). “LEO constellation-augmented multi-GNSS for rapid PPP convergence”. In: *Journal of Geodesy* 93.5, pp. 749–764. DOI: 10.1007/s00190-018-1195-2.

Liu, J., Wang, K., El-Mowafy, A., and Yang, X. (2024). “PCO and hardware delay calibration for LEO satellite antenna downlinking navigation signals”. In: *Measurement Science and Technology* 35.8, p. 086314. DOI: 10.1088/1361-6501/ad48a2.

Lyard, F., Lefevre, F., Letellier, T., and Francis, O. (2006). “Modelling the global ocean tides: Modern insights from FES2004”. In: *Ocean Dynamics* 56.5-6, pp. 394–415. DOI: 10.1007/s10236-006-0086-x.

Mao, F., Lou, Y., Geng, C., Song, Q., Gong, X., and Gu, S. (2024). “Evaluation of timing and time transfer with PPP using Galileo High Accuracy Service”. In: *Measurement* 226, p. 114152.

Massarweh, L. (2024a). “Numerical assessment of LEO-PNT performance: a comparison between ambiguity-float and ambiguity-fixed precise point positioning solutions”. In: *European Navigation Conference (ENC) 2024*. ESA/ESTEC, Noordwijk, The Netherlands.

— (2024b). “Impact of modelling errors on LEO-PNT performance: a brief numerical investigation on ambiguity-fixed positioning”. In: *11th ESA Workshop on Satellite Navigation Technologies (NAVITEC) 2024*. ESA/ESTEC, Noordwijk, The Netherlands.

Mayer-Gürr, T. et al. (2012). “The New Combined Satellite Only Model GOCO03S”. In: *GGHS Meeting*. Paper S2–183. Venice, Italy.

Montenbruck, O. and Gill, E. (2000). *Satellite Orbits: Models, Methods and Applications*. Berlin, Heidelberg: Springer. DOI: 10.1007/978-3-642-58351-3.

Montenbruck, O., Hackel, S., Wermuth, M., et al. (2021). “Sentinel-6A precise orbit determination using a combined GPS/Galileo receiver”. In: *Journal of Geodesy* 95, p. 109. DOI: 10.1007/s00190-021-01563-z.

Montenbruck, O., Kunzi, F., and Hauschild, A. (2022). “Performance assessment of GNSS-based real-time navigation for the Sentinel-6 spacecraft”. In: *GPS Solutions* 26.1, p. 12. DOI: 10.1007/s10291-021-01198-9.

Montenbruck, O., Markgraf, M., Santandrea, S., Naudet, J., Gantois, K., and Vuilleumier, P. (2008). “Autonomous and Precise Navigation of the PROBA-2 Spacecraft”. In: DOI: 10.2514/6.2008-7086.

Montenbruck, O. and Ramos-Bosch, P. (2008). “Precision real-time navigation of LEO satellites using global positioning system measurements”. In: *GPS Solutions* 12.3, pp. 187–198. DOI: 10.1007/s10291-007-0080-x.

Montenbruck, O., Steigenberger, P., and Hauschild, A. (2015). “Broadcast versus precise ephemerides: a multi-GNSS perspective”. In: *GPS Solutions* 19.2, pp. 321–333. DOI: 10.1007/s10291-014-0390-8.

— (2018). “Multi-GNSS signal-in-space range error assessment – Methodology and results”. In: *Advances in Space Research* 61.12, pp. 3020–3038. DOI: https://doi.org/10.1016/j.asr.2018.03.041.

Montenbruck, O., Steigenberger, P., Thoelert, S., Arnold, D., and Bury, G. (2023). “GNSS visibility and performance implications for the GENESIS mission”. In: *Journal of Geodesy* 97.10, p. 96. DOI: 10.1007/s00190-023-01784-4.

Montenbruck, O., van Helleputte, T., Kroes, R., and Gill, E. (2005). “Reduced dynamic orbit determination using GPS code and carrier measurements”. In: *Aerospace Science and Technology* 9.3, pp. 261–271. DOI: https://doi.org/10.1016/j.ast.2005.01.003.

Mu, X. (2023). “CENTISPACE LEO Augmentation Navigation System Status”. In: *ICG LEO-PNT Workshop 2023*. Beijing Future Navigation Technology Co. Ltd.

Murata, M., Akiyama, K., and Kogure, S. (2024). “Impact of Signal-in-Space Error on LEO PNT Augmented PPP Convergence”. In: *Proceedings of the 2024 International Technical Meeting of The Institute of Navigation*. Long Beach, California, pp. 692–701. DOI: 10.33012/2024.19509.

Naciri, N., Yi, D., Bisnath, S., Blas, F. J. de, and Capua, R. (2023). “Assessment of Galileo High Accuracy Service (HAS) test signals and preliminary positioning performance”. In: *GPS Solutions* 27.73. DOI: 10.1007/s10291-023-01410-y.

Peter, H., Springer, T., Zangerl, F., and Reichinger, H. (2022a). “Beyond Gravity PODRIX GNSS Receiver on Sentinel-6 Michael Freilich – Receiver Performance and POD Analysis”. In: *Proceedings of the 35th International Technical Meeting of the Satellite Division of The Institute of Navigation (ION GNSS+ 2022)*. Denver, Colorado, pp. 589–601. DOI: 10.33012/2022.18368.

— (2022b). “Beyond Gravity PODRIX GNSS Receiver on Sentinel-6 Michael Freilich – Receiver Performance and POD Analysis”. In: *Proceedings of the 35th International Technical Meeting of the Satellite Division of The Institute of Navigation (ION GNSS+ 2022)*. Denver, Colorado, pp. 589–601. DOI: 10.33012/2022.18368.

Petit, G. and Luzum, B. (2010). *IERS Conventions (2010)*. Tech. rep. IERS Technical Note No. 36. Frankfurt am Main: Verlag des Bundesamts für Kartographie und Geodäsie: International Earth Rotation and Reference Systems Service (IERS).

Prange, L., Orliac, E., Dach, R., et al. (2017). “CODE’s five-system orbit and clock solution—the challenges of multi-GNSS data analysis”. In: *Journal of Geodesy* 91, pp. 345–360. DOI: 10.1007/s00190-016-0968-8.

Prange, L., Villiger, A., Sidorov, D., Schaer, S., Beutler, G., Dach, R., and Jäggi, A. (2020). “Overview of CODE’s MGEX solution with the focus on Galileo”. In: *Advances in Space Research* 66.12. Scientific and Fundamental Aspects of GNSS - Part 1, pp. 2786–2798. DOI: https://doi.org/10.1016/j.asr.2020.04.038.

Priestley, K. J., Smith, G. L., Thomas, S., Cooper, D., Lee, R. B., Walikainen, D., Hess, P., Szewczyk, Z. P., and Wilson, R. (2011). “Radiometric Performance of the CERES Earth Radiation Budget Climate Record Sensors on the EOS Aqua and Terra Spacecraft through April 2007”. In: *Journal of Atmospheric and Oceanic Technology* 28.1, pp. 3–21. DOI: 10.1175/2010JTECHA1521.1.

Prol, F. S. et al. (2022). “Position, Navigation, and Timing (PNT) Through Low Earth Orbit (LEO) Satellites: A Survey on Current Status, Challenges, and Opportunities”. In: *IEEE Access* 10, pp. 83971–84002. DOI: 10.1109/ACCESS.2022.3194050.

Reid, T. G., Chan, B., Goel, A., Gunning, K., Manning, B., Martin, J., Neish, A., Perkins, A., and Tarantino, P. (2020a). “Satellite Navigation for the Age of Autonomy”. In: *2020 IEEE/ION Position, Location and Navigation Symposium (PLANS)*. 2020 IEEE/ION Position, Location and Navigation Symposium (PLANS). Portland, OR, USA: IEEE, pp. 342–352. DOI: 10.1109/PLANS46316.2020.9109938.

Reid, T. G., Walter, T., Enge, P. K., Lawrence, D., Cobb, H. S., Gutt, G., O’Connor, M., and Whelan, D. (2020b). “Navigation from Low Earth Orbit: Part 1: Concept, Current Capability, and Future Promise”. In: *Position, Navigation, and Timing Technologies in the 21st Century*. Ed. by Y. T. J. Morton, F. Diggelen, J. J. Spilker, B. W. Parkinson, S. Lo, and G. Gao. 1st ed. Wiley, pp. 1359–1379. DOI: 10.1002/9781119458555.ch43a.

Ries, L. et al. (2023). “LEO-PNT for Augmenting Europe’s Space-based PNT Capabilities”. In: *2023 IEEE/ION Position, Location and Navigation Symposium (PLANS)*. 2023 IEEE/ION Position, Location and Navigation Symposium (PLANS). Monterey, CA, USA: IEEE, pp. 329–337. DOI: 10.1109/PLANS53410.2023.10139999.

Romero, I. (2020). *RINEX - The Receiver Independent Exchange Format*. Version 3.05, 1 December 2020.

Su, M., Su, X., Zhao, Q., and Liu, J. (2019). “BeiDou Augmented Navigation from Low Earth Orbit Satellites”. In: *Sensors* 19.1, p. 198. DOI: 10.3390/s19010198.

Teunissen, P. and Montenbruck, O. (2017). “Springer handbook of global navigation satellite systems”. In: DOI: 10.1007/978-3-319-42928-1.

Teunissen, P. J. (2020). “GNSS Precise Point Positioning”. In: *Position, Navigation, and Timing Technologies in the 21st Century*. Ed. by Y. T. J. Morton, F. Diggelen, J. J. Spilker, B. W. Parkinson, S. Lo, and G. Gao. 1st ed. Wiley, pp. 503–528. DOI: 10.1002/9781119458449.ch20.

UNOOSA (2021). *The Interoperable Global Navigation Satellite Systems Space Service Volume (Second Edition)*. United Nations, Vienna, ST/SPACE/75/Rev.1.

— (2023). *Workshop on Low Earth Orbit (LEO) Positioning Navigation and Timing (PNT) Systems*. Workshop proceedings and presentations focused on LEO-based PNT systems. Vienna International Centre, Vienna (Hybrid Format): United Nations Office for Outer Space Affairs.

Vallado, D. A. (2013). *Fundamentals of Astrodynamics and Applications*. 4th. Hawthorne, CA and New York, NY: Microcosm Press and Springer.

Wang, K., Liu, J., Su, H., El-Mowafy, A., and Yang, X. (2023a). “Real-Time LEO Satellite Orbits Based on Batch Least-Squares Orbit Determination with Short-Term Orbit Prediction”. In: *Remote Sensing* 15.1, p. 133. DOI: 10.3390/rs15010133.

Wang, K. and El-Mowafy, A. (2022). “LEO satellite clock analysis and prediction for positioning applications”. In: *Geo-spatial Information Science* 25.1, pp. 14–33. DOI: 10.1080/10095020.2021.1917310.

Wang, K., El-Mowafy, A., Cheng, F., and Yang, X. (2024). “LEO Augmentation in Large-Scale Ionosphere-Float PPP-RTK Positioning”. In: *Journal of Surveying Engineering* 150.2, p. 04024001. DOI: 10.1061/JSUED2.SUENG-1414.

Wang, K., El-Mowafy, A., Su, H., and Yang, X. (2023b). “On the Very Short and Very Long LEO Satellite Orbit Prediction”. In: 2023 International Technical Meeting of The Institute of Navigation. Long Beach, California, pp. 725–735. DOI: 10.33012/2023.18665.

Wermuth, M., Montenbruck, O., and Helleputte, T. van (2010). “GPS HIGH PRECISION ORBIT DETERMIANTION SOFTWARE TOOLS (GHOST)”. In: *Proceedings of 4th International Conference on Astrodynamics Tools and Techniques*.

Wu, M., Wang, K., Wang, J., Xie, W., Liu, J., Chen, B., Ge, Y., El-Mowafy, A., and Yang, X. (2024). “Impact of Latency and Continuity of GNSS Products on Filter-Based Real-Time LEO Satellite Clock Determination”. In: *Remote Sensing* 16.22. DOI: 10.3390/rs16224315.

Wu, S., Yunck, T., and Thornton, C. (1990). “A reduced-dynamic technique for precise orbit determination”. In: *Telecommunications and Data Acquisition Progress Report*.

Xu, S., Yang, Q., Du, X., Xu, X., Zhao, Q., Yang, L., Qin, Y., and Guo, J. (2024). “Multi-GNSS Precise Point Positioning enhanced by the real navigation signals from CENTISPACETM LEO mission”. In: *Advances in Space Research*, S0273117724000358. DOI: 10.1016/j.asr.2024.01.017.

Youn, C. (2023). “Xona Space Systems”. In: *International Committee on GNSS, Workshop on Low Earth Orbit (LEO) PNT Systems*.

Zheng, Y., Ge, H., and Li, B. (2024). “The convergence mechanism of Low Earth Orbit enhanced GNSS (LeGNSS) Precise Point Positioning (PPP)”. In: *Geo-spatial Information Science* 27.6, pp. 2211–2226. DOI: 10.1080/10095020.2023.2270712.

Zhou, P., Xiao, G., and Du, L. (2024). “Initial performance assessment of Galileo High Accuracy Service with software-defined receiver”. In: *GPS Solutions* 28.2. DOI: 10.1007/s10291-023-01540-3.